Politecnico di Torino
Master of science program in Automotive Engineering

Master Thesis

Computational Fluid Dynamics investigation on Ducted Fuel Injection operation with Multi-Injection strategies

Relators
Prof. Federico MILLO
Dr. Andrea PIANO
Cristiano SEGATORI

Candidate
Marco ORLANDO

October 2023

Abstract

Ducted Fuel Injection (DFI) is a concept of growing interest to mitigate soot formation in the diesel combustion process and, simultaneously, break the usual trade-off between soot and Nitrogen Oxides (NOx) emissions. Particularly, the concept is to inject a fuel spray down the axis of a small duct, positioned within the combustion chamber some distance downstream of the injector orifice exit, so that the mixing between air and fuel is increased; as a consequence, a lower equivalence ratio as well as lower engine-out soot emissions are expected.

However, the research studies conducted so far have been mainly performed considering only a single-injection event, while state-of-the art diesel engines typically feature highly optimized Multi-Injection (MI) strategies to address emissions, combustion noise and engine performance issues. Therefore, it still remains nowadays an open point, in scientific literature, the synergistic exploitation of both MI strategy and DFI technology. Particularly, this aspect is of paramount importance to achieve cleaner and more efficient combustion engines. In this framework, the present master thesis work aims to analyse the impact of different MI strategies on the DFI operation in constant-volume conditions.

To achieve this objective, two distinct spray models were utilized for analysis in the 3D Computational Fluid Dynamics (CFD). The first model had been previously developed and rigorously verified using experimental data for single-injection strategies, encompassing both free-spray scenarios (where the fuel spray is not constrained by a duct) and DFI configurations. The second model, which refers to the ECN Spray D conditions, was entirely developed as part of this study. After that, predictive non-reacting have been performed to investigate the effect of MI strategies with DFI. Regarding the injection profiles, various split injections featuring different hydraulic dwell times and proportions of injected mass were examined. Additionally, a tool for generating these profiles was developed as part of this work.

From an overall point of view, the simulation outcomes have substantiated the capacity of duct utilization to increase mixing among air and fuel, even when employing multiple injection (MI) strategies. Indeed, the interactions between various injection events did not significantly alter the overall flow dynamics and, consequently, the advantages in terms of air entrainment and equivalence ratio distribution remained intact. However, some criticism in term of equivalence ratio distribution are found when the fully-predictive model is employed.

In conclusion, the findings derived from the analyses conducted in this study do not present significant challenges for the integration of Ducted Fuel Injection and Multi-Injection strategies. This represents a promising advancement, setting the stage for more in-depth investigations in the future.

Sommario

La Ducted Fuel Injection è una tecnologia innovativa per ridurre la formazione di particolato durante la combustione Diesel e, contemporaneamente, non influire negativamente sugli altri inquinanti, soprattutto gli ossidi di azoto NO_x, contrariamente a numerose strategie di controllo adoperate per questi motori. In particolare, il concetto consiste nell'iniettare il carburante lungo l'asse di un piccolo condotto, *"duct"*, posizionato all'interno della camera di combustione a una certa distanza dall'uscita dell'orifizio dell'iniettore, in modo da aumentare la miscelazione tra aria e carburante; di conseguenza, si possono ottenere un maggiore rapporto aria-carburante e minori emissioni di particolato in uscita dal motore.

Nonostante i risultati sperimentali relativi all'impiego di questa tecnologia siano molto promettenti, non sono ancora noti gli effetti derivanti dall'interazione sinergica tra la Ducted Fuel Injection e strategie di iniezione multipla (MI). Infatti, tutti gli studi di ricerca condotti finora hanno utilizzato esclusivamente su iniezioni singole, mentre nei moderni motori diesel, strategie di iniezione multipla sono ampiamente adottate, data la loro capacità di ottimizzare simultaneamente emissioni, rumore di combustione e prestazioni del motore. Pertanto, il presente lavoro di tesi magistrale mira ad analizzare l'impatto di diverse strategie di iniezione multipla sui benefici introdotti dall'adozione della DFI. Le analisi verranno effettuate in camera a volume costante.

L'approccio seguito in questo studio è di natura numerica, basato sull'impiego di due distinti modelli di *spray* sviluppati per mezzo di software di Fluido-dinamica Computazionale (CFD). Per il primo modello, si fa riferimento a un modello di spray precedentemente sviluppato, opportunamente calibrato e adeguatamente convalidato mediante dati sperimentali sia nelle condizioni di "spray libero" (*free spray*), quindi non vincolato dalla presenza del duct, sia in quelle relative alla configurazione DFI. In virtù di questo processo di validazione pregressa, la sua affidabilità è considerata un elemento consolidato.

Per quanto riguarda il secondo modello, ci si riferirà alle ben note condizioni *Sray D*, e il processo di calibrazione e convalida costituisce un aspetto essenziale di questo lavoro. Tuttavia, va sottolineato che tale modello sarà validato esclusivamente per le condizioni *free spray*, poiché mancano dati sperimentali in condizioni DFI.

Successivamente, sono state effettuate diverse simulazioni in condizioni non reattive per analizzare l'effetto delle strategie di iniezione multipla quando utilizzate con DFI. Per quanto riguarda i profili di iniezione, soltanto iniezioni doppie, *split-injection*, sono state utilizzate, variando opportunamente i valori di *dwell time* e la quantità di massa iniettata in ogni singola iniezione. Inoltre, è stato creato un *tool* per la creazione di tali profili sulla base dei dati sperimentali a singola iniezione, così da poterli utilizzare nelle sopracitate simulazioni.

In generale, i risultati delle simulazioni hanno confermato la migliore miscelazione tra aria e combustibile ottenuta attraverso l'utilizzo del *duct*, anche quando si adottano strategie di iniezione multipla (MI). Infatti, le interazioni tra diversi eventi di iniezione non hanno alterato significativamente la dinamica complessiva del flusso. Nonostante ciò, alcune criticità sono state notate, per quanto riguarda il rapporto aria-combustibile, nelle simulazioni condotte con il modello di spray DFI facente riferimento alle condizioni Spray D.

Contents

List of Figures

List of Tables

Chapter 1

Introduction

In recent years, there has been growing emphasis on addressing air quality and climate change concerns, leading governments to implement increasingly stringent regulations. Within this context, Internal Combustion Engines (ICEs) have been recognized as significant contributors to environmental issues due to their tailpipe emissions. These emissions primarily encompass five key types: carbon dioxide (CO_2), carbon monoxide (CO), nitrogen oxides (NO_x), unburned hydrocarbons (HC) and particulate matter (PM). Consequently, ICEs play a dual role in exacerbating both climate change and air quality issues. As a result, all modern vehicles are equipped with different aftertreatment systems (ATS) for emission management. Particularly, concerning Diesel Engines, they are mostly affected by soot - PM carbonaceous fraction - and NO_x emissions, leading to the needs of complex ATS such as the Selective Catalytic Reduction (SCR) and Diesel Particulate Filter (DPF).

The introduction of these devices is critical, not only due to their efficiency and associated costs (with DPF achieving high efficiency values), but also due to the fuel penalties they impose, stemming from regeneration and increased engine back-pressure. Moreover, the progressively stringent regulations will make difficult the achievement of the targets even when these device are employed. These factors have propelled research efforts toward developing innovative combustion strategies capable of reducing engine-out emissions compared to conventional approaches.

The Diesel combustion is a very complex phenomenon: differently from spark-ignition-engine combustion process, this process cannot be treated as homogeneous but, on the contrary, it is important to refer to local thermodynamic characteristics. *Dec.* [1] gave a description of the combustion process in Diesel engines, highlighting the presence of rich core were the combustion started even if not in stoichiometric conditions; moreover, high temperature zones were individuated and the high availability of oxygen encouraged the formation of nitrogen oxides. The well known Kamimoto-Bae diagram shown in a T-ϕ diagram the formation zones for both NO_x and soot pollutants, highlighting the soot/NO_x trade-off, typical of Diesel Engine. One of the most common and widely employed techniques used in this context is Exhaust Gas Recirculation (EGR), where part of the exhaust gases is reintroduced into the combustion chamber. This process creates a dilution effect, as well as thermal and chemical, that partially inhibits the formation of nitrogen oxides (NO_x). However, according to the just mentioned soot/NO_x trade-off, as demonstrated in [2] "*...the conventional use of EGR, whereby some trapped air is displaced by the EGR, achieves significant reduction in NO_x emissions, but at the expense of a significant increase of particulate emissions*". Coming back to the Kamimoto-Bae diagram, even most of it is characterized by such a trade-off, it is possible to identify a zone where this is no more valid, arising to the possibility of advanced combustion strategies.

In this context it is of particular interest the Leaner-Lifted Flame Combustion, that is defined as "*mixing-controlled combustion that does not produce soot because it occurs at equivalence ratios less than or equal to approximately 2*" [3]; particularly, the LLFC concept was developed before of the cited work, but mainly in constant-volume combustion vessel (CVCV) condition. In the perspective of such a combustion process, it assumes a huge importance the lift-off length (LOL) defined as the distance from the injector where the standing premixed auto-ignition occurs and stabilizes; equally important is the assessment of the equivalence ratio at this critical point in the combustion process. In the research carried out by *Polonowski et al.* [3], the LLFC concept was tested on a single-cylinder engine and three different injector configurations were tested, each one characterized by a specific number of holes - 2, 6 and 10 holes respectively. Moreover, the effects of different parameters, such as TDC temperature, injection pressure and oxygen concentration were investigated. The promising outcomes achieved in constant-volume combustion vessel (CVCV) environment faced challenges when transitioning to engine-like conditions. Specifically, the LLFC was activated and sustained throughout the entire mixing-controlled burn phase, but only when utilizing the 2-hole injector setup. This behavior highlights the intricate interplay between adjacent fuel sprays, resulting in re-entrainment and proximity coupling phenomena. Consequently, there arose a necessity to extend the lift-off length of the fuel spray as well as enhance the mixing between the incoming air and fuel upstream of this critical point.

In this framework, a very promising technology is the ducted fuel injection (DFI) which consists in the injection of the fuel down the axis of a small duct positioned towards the injector hole within the combustion chamber. As for LLFC, first study conducted by *Mueller et al.* [4] were performed in constant-volume combustion vessel conditions. The expected improvements were an higher mixing due to higher velocity gradient between air and fuel, higher combustion efficiency due to enrichment of the most-fuel-lean mixture, increased ignition delay due to cooler charge inside the duct as well as limited re-entrainment phenomena. In [4], different operating temperature were tested - 800, 850, 900, 950 and 1000 K respectively - leading to a broader temperature range for the analysis and testing of the effectiveness of such technology. The results obtained from OH* chemiluminescence and natural luminosity measurements have brought to light the substantial potential for reducing soot emissions with Ducted Fuel Injection (DFI). Notably, except for the scenario at a temperature of 800 K, the natural luminosity signal, which is indicative of soot production, consistently exhibited high visibility in the case of free-spray combustion. However, this signal was significantly diminished when DFI was employed, suggesting a marked reduction in soot emissions in such instances. Moreover, it was of particular interest the case with the highest temperature (T=1000 K): in that operating condition, it was possible to observe as the flame was anchored at or upstream of the duct exit, giving no possibility for air and fuel to mix in that region. As a result, it was hypothesized an higher mixing and air entrainment in the region between the nozzle and duct inlet due to the presence of the duct itself.

The assumption of a greater air entrainment upstream of the duct inlet was confirmed by *Millo et al.* in [5], where a numerical investigation on spray characteristics was performed for both non-reacting and combustion conditions with the adoption of DFI. In this context, indeed, the pressure field analysis showed an under-pressure area in the duct inlet region becoming more evident as the injection proceeded. As a result, a sort of suction effect was created for the air, increasing air entrainment into fuel spray, and air-fuel mixing upon the duct inlet. Other important outcome of the analysis was the formation of local turbulent eddies at the duct outlet, due to the high velocity gradient between the high-speed ducted spray and quiescent air-chamber as expected in [4]; furthermore, looking at the flow inside the duct, the turbulent kinetic energy showed a radial distribution leading to favourable condition for air/fuel mixing. Finally, considering the equivalence ratio distribution, no rich-pockets were present in the case of DFI, with values lower than 2 for the whole injection duration.

In [6], *Gehmlich et al.* conducted a study examining the influence of duct shape, specifically focusing on four different configurations involving a rounded inlet and tapers at the outlet. The results obtained confirmed what discussed already in [4] and, at the same time, led to the adoption of a different shape for the duct. Indeed, it was demonstrated how a rounded inlet was associated to a higher lift-off length, so to a great soot reduction; furthermore, the taper on the outlet had not a great effect on duct performance, but appeared to reduce the risk of combustion anchoring, as happened in the case of T=1000 K in [4]. Ultimately, the study revealed that the total pressure rise was not contingent upon the duct shape; however, it consistently exhibited higher values in the case of DFI combustion. This theoretically related to a more efficient combustion process associated with DFI.

Further investigation on the duct geometry properties were performed by *K. Svensson and G. Martin* in [7], looking at the influence stand-off distance - distance between the injector hole and the duct inlet - and duct length had on duct performances. From this point of view, an increment in the stand-off distance led to higher soot production; this was valid also for the length of the duct. It is essential to note that these results are not universally applicable but rather dependent on specific operating conditions. For example, in [7], it was demonstrated that at a pressure of 120 bar and a stand-off distance of 6 mm, the natural luminosity signal for the DFI cases is significantly higher compared to the free-spray cases. This difference is attributed to a lift-off length that is shorter than the stand-off distance under these conditions. Moreover, it should be also considered the interaction among these parameters, that is not-linear.

Although the results obtained in the constant-volume combustion vessel experiments have shown promise, it's important to note that these experiments were conducted under conditions quite different from those encountered in real-engine applications. In this sense, the analysis performed by *Nilsen et al.* in [8] represents the first DFI application attempt in engine condition. The engine was a 1.7L single-cylinder engine with 2-holes injector[1] and two oxygen concentrations were tested - 16% and 21% respectively - in order to investigate also the coupling possibility of this technology with exhaust gas re-circulation technique (EGR). The results fully confirmed the outcomes of [4],[6] and [7], showing a strong attenuation of engine-out soot emissions for both oxygen concentration setups. Moreover, looking at the apparent heat release rate curve, it was possible to appreciate a higher premixed-burn spike in the case of DFI combustion, suggesting a more persistent premixed phase, as demonstrated also by the fact that the curves approached zero first for DFI case with respect to free-spray one. Furthermore, measurements of other pollutant-species engine-out emissions did not seem to be strongly influenced by the presence of the duct, without any particular increment, except for CO ones, that increased but remaining still well manageable by basic ATS device.

Finally, even it has been demonstrated in previous work [4] that DFI was linked to an higher total pressure rise, leading to a more efficient combustion, experimental results obtained in [8] showed a lower fuel-conversion-efficiency for the DFI case: this was not in contrast with the previous findings; indeed, the lower total efficiency could be related to a lower pressure in the DFI cases up from 30 crank-angle-degrees (CAD) aTDC, and the reason why of this lower pressure may be linked to higher heat transfer given the presence of the duct and its support surfaces.

The research conducted in [8] was subsequently extended in [9]; again, a 1.7L single-cylinder engine was employed but here equipped with a 4-holes injector. The second phase

---

[1] For further information about experimental setup refer directly to the cited article.

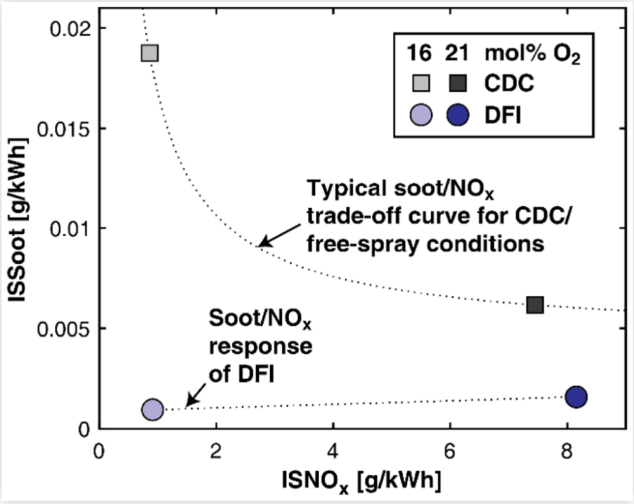

Figure 1.1: "DFI breaks the soot/NO_x trade-off by simultaneously attenuating soot and NO_x formation. Plot shows measured ISSoot and NO_x data for CDC and for DFI", from [8, figure 11]

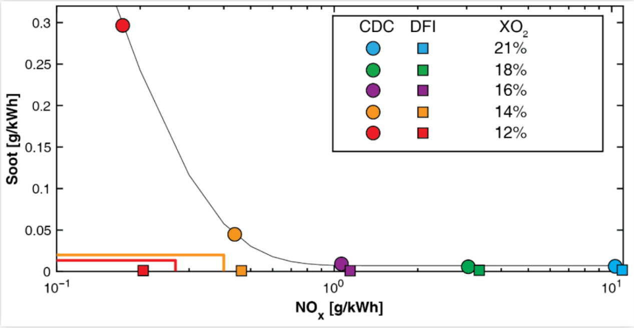

Figure 1.2: "Soot vs. NO_x plot for DFI and CDC in the XO_2 sweep", from [9, figure 16]

of this research expanded the scope by considering a broader range of parameter variations. These included oxygen concentrations, injection pressure, injection duration (*for load modulation*), and start of combustion timing sweeps.

The results of this extended investigation further affirmed the potential of Ducted Fuel Injection technology, demonstrating its efficacy in significantly reducing soot emissions. However, it should be noted that when exploring various engine load conditions, limitations were identified, particularly in high-load scenarios.

Of particular interest is the oxygen concentration modulation performed both in [8] and [9]. In this context, indeed, it was demonstrated the ability of DFI in breaking the usual trade-off between soot and nitrogen oxide engine-out emissions. The obtained results are reported in fig. 1.1 and 1.2. How it is possible to notice, DFI scenario allowed high dilution levels in both cases, not feasible with CDC due to the resultant soot emissions.

The remarkable achievements observed in DFI engine applications prompted considerations regarding the feasibility of retrofitting this technology onto existing engines, especially in the context of heavy-duty applications. At this purpose, *Svensson et al.* [10] conducted a research on a 2.5L single-cylinder engine, operated with two different working modes, each

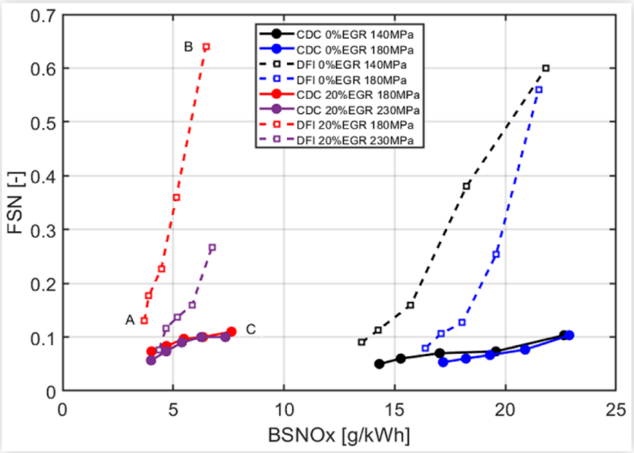

Figure 1.3: "FSN vs BSNO$_x$ at A100 operating condition. Injection timing sweeps at two rail pressures and two EGR levels", from [10, figure 11]

one at different operating conditions[2]; also in this case CDC and DFI operation were compared. In contrast to previous findings, the engine-out soot emissions were notably elevated with DFI, while NO$_x$ emissions were reduced as shown in fig. 1.3. Additionally, a clear dependence on rail pressure and injection timing was identified for DFI operations, which contrasted with the behavior observed in conventional diesel combustion.

Despite the opposite and not favourable results obtained, some consideration should be done highlighting the totally different operating conditions over which DFI was tested in this work, compared to [8] and [9]; indeed, the load experienced was more than doubled[3] and, in this sense, it confirmed the high sensitivity of DFI technology to high-load application. Furthermore, it was of paramount importance to consider the retrofitting as an attempt to adapt this technology in a engine-design architecture not optimized for its operation. Finally, in [10] a more complex injector configuration was used, characterized by six holes: re-entrainment and proximity coupling phenomena could lead to a reduction of the lift-off length canceling out the improvement due to DFI implementation.

In the retrofitting context, a numerical investigation was performed by *Piano et al.* [11]. Differently from [10] a light-duty application was the object of the work, even both low and high loads conditions were tested. Regarding the performed analysis, firstly a cold flow analysis was performed: this was of paramount importance to understand how the flow field was modified due to the duct presence within the combustion chamber. The major outcome was a modified flow field, characterized by lower swirl intensity in the DFI case, finally leading to lower mixing between air and fuel.

The combustion simulation performed in [11] had also important outcomes; indeed, it showed an increment of the soot engine-out emissions if compared with the free-spray case, coherently with the findings of [10]. However, DFI operations were still characterized by longer ignition delay and more intense premixed burn. Despite the higher amount of soot emitted, different behaviour would have been expected in reference of the soot formation phase - first stage of the combustion process - were DFI operations were associated with lower soot production; on the contrary, in the soot oxidation phase totally different results were obtained, with a greater oxidation process for free-spray mode. For this reason, the two

---

[2] Refer to [10, table 2 and table 3] for more information.

[3] IMEP maximum of 8 bar in [9], while over 20 bar in [10].

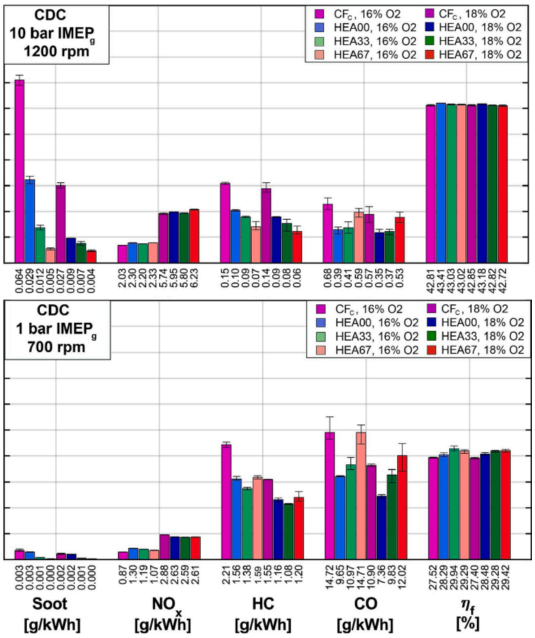

Figure 1.4: "Fuel effect on performance and emissions for the four fuels at CDC conditions", from [12, figure 6].

phases were analysed separately in order to obtain a better understanding; for the first stage, i.e. soot formation phase (6 deg aTDCf), the cumulated entrainment curve highlighted an higher amount of air entering in the spray for DFI. This was in line with the findings of [5] were higher entrainment was experienced at the duct inlet in DFI cases. Furthermore, looking at the centerline equivalence ratio in [11], DFI still attenuated it, even the obtained values were higher than 2. Moving to the second stage, from 6 deg to 50 deg aTDCf, the flow is characterized by lower temperatures, especially in the region close to the duct, preventing the soot oxidation process to be as efficient as in the free-spray case.

Moving to the high-load working point, the numerical investigation reaffirmed the challenges associated with DFI in comparison to this specific operating condition: slower combustion without any increment in the ignition delay led to a combustion degradation, as testified also by the in-cylinder pressure trace were a gap of 20 bar was present among DFI and free-spray. The reason why of this degradation was associated with the ignition of most of the mixture in the in-duct region highlighting, again, that "*the very high reactivity conditions characteristics of the full load K-point are thus prohibitive for a proper DFI operation*" [11].

Despite the findings from [10] and [11], the significant potential for soot reduction has been explored in conjunction with the use of *low-net carbon fuels*, as investigated by *Nyrenstedt et al.* in [12]; the work objective was to have an understating on their coupling possibilities to meet future regulation targets.

The study encompassed four distinct fuels, which comprised a No.2 S15 diesel as a reference, and three oxygenated fuels; these varied in terms of their blend compositions, i.e. products from hydrothermal liquefaction (HTL), ethanol-to-distillate conversion (ETD) and alkoxyalkanoate (AOA) synthesis contents[4]. Different dilution levels have been included in

---

[4] For further information on blends composition and properties refer to [12, table 1 and table2].

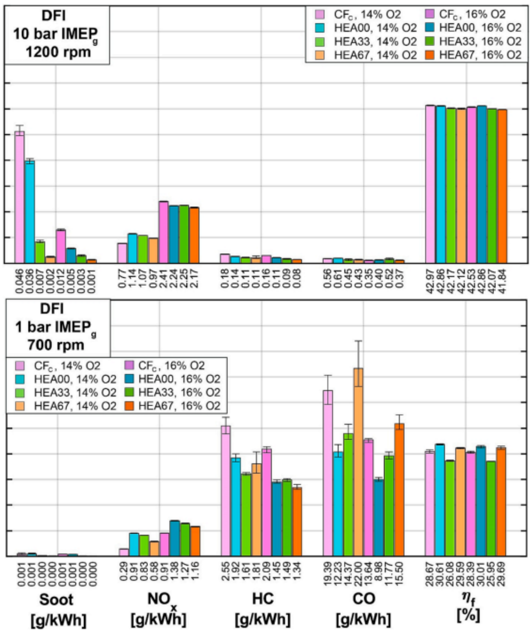

Figure 1.5: ”Emissions and performance of DFI with HEAxx fuel blends at 10 bar and 1 bar IMEP$_g$”, from [12, figure 7].

the analysis too. The work has been performed in four different steps: first, the benefits from DFI introduction were tested, then a fuel sweep was performed for both CDC and DFI; finally, ducted fuel injection, oxygenated fuels and different dilution levels were tested together.

Moving directly to the results, they are reported in fig. 1.4 and 1.5. The potential of DFI in soot mitigation was again proved, even though the attenuation obtained with low-net carbon fuels is more relevant. Moreover, the dilution effect was still effective for nitrogen oxides reduction. Final outcome of the work was a total reduced efficiency needed for the NO_x ATS: indeed, looking at 2027 regulation targets, needed efficiency of 41.5% for Particulate Matter (PM) Aftertreatment Systems (ATS) was attained at 16 mol% O_2 dilution level for conventional diesel fuel and it was reduced at 0% when passing to HEA00 blend. Hence, the coupling of low-net carbon fuels and DFI technology has been shown to be a very promising solution, even considering the fact that *”high dilution may become crucial for keeping the needed ATS efficiency within feasible levels. SCR systems can deliver high efficiencies, but this requires a system expansion where additional SCR hardware adds to the complexity, space, and cost-of ownership for a vehicle [...]. DFI unlocks additional solution options, compared to CDC, for meeting future emissions regulations”* [12].

In summary, the DFI potential for soot mitigation has been investigated during the years, first in constant-volume combustion chamber environment, than in engine-like applications. Furthermore, the retrofitting solution on existing engine has been also discussed, even with poor results. However, still a gap in literature is present, regarding the synergistic exploitation of both multi-injection strategy and DFI technology; this is going to be an aspect of huge importance for the effective applicability of this new concept, being state-of-the art diesel engines featured with much more complex injection profile with respect to the single-injection-event exploited in most of the presented work.

In light of the preceding discussion, the primary objective of this study is to conduct an initial analysis in non-reacting conditions to examine the effects and phenomena associated with a second injection event when employing ducted fuel injection (DFI) technology. To accomplish this, various tasks have been undertaken in the following sections. Two spray models developed within a Computational Fluid Dynamics (CFD) framework have been employed for this purpose.

The first model, i.e. *Polito-UniPG spray model*, has previously been developed and validated against experimental data for both free-spray and DFI cases. Hence, no additional efforts in terms of calibration or validation are required for this work. Conversely, the second model, referred to as the *ECN Spray D model*, has been entirely developed and validated as part of this study. However, since experimental DFI data are unavailable for the specific conditions, this model will be considered as fully-predictive.

As a result, the following sections will begin with an overview of the experimental conditions upon which the models were developed. Subsequently, the development of the ECN Spray D model will be elaborated. Concurrently, two tools designed for creating multi-injection profiles based on the experimental rate shapes used during the experiments will be introduced, with a specific focus on their operational principles. These tools will play a crucial role in the subsequent non-reacting analysis, where the obtained injection profiles will be utilized. Finally, the results of the non-reacting analysis will be presented, with a particular emphasis on air entrainment phenomena, turbulent mixing, and equivalence ratio distribution. Through this approach, the potential for coupling DFI and multi-injection strategies will be examined contemporaneously with the potential of the numerical tools developed during this study.

Chapter 2

Experimental Case Studies

In the initial chapter, the primary goal of this study was introduced, which is to examine the performance of DFI (Ducted Fuel Injection) sprays when utilizing multi-injection profiles. In the context of this research, two specific experimental setups have been selected as reference points: the PoliTO-UniPG setup, as previously discussed in [5], and the ECN Spray D setup. The choice of these setups is based on distinct reasons:

- **PoliTO-UniPG Setup**: The PoliTO-UniPG experimental setup is preferred due to its extensive data availability for both DFI and free-spray characterizations, as well as to be in line with the previous findings of [5]. Consequently, the CFD model previously developed based on this setup is considered reliable and validated for both of these conditions.

- **ECN Spray D Setup**: The selection of the ECN Spray D setup is motivated by the aim to closely match the injector configuration used in the PoliTO-UniPG spray model. However, it's important to note that this setup lacks data for DFI configuration, which is a notable distinction from the PoliTO-UniPG setup.

This chapter provides a detailed examination of the experimental setups for both conditions outlined in sections 2.1 and 2.2. Particular attention will be given to the identification of critical thermodynamic properties that serve as reference values for the associated simulation setups.

2.1 PoliTO-UniPG spray chamber

In the context of the PoliTO-UniPG data, all the tests were conducted within a constant-volume vessel. This choice was made to ensure quasi-steady thermodynamic conditions and to simplify the installation of the duct. The primary objective of this experimental campaign was to investigate the underlying phenomena involved in mixture formation for DFI applications, thus not requiring the need for an engine-specific setup.

The constant-volume vessel utilized in this application was equipped to operate at pressures up to 30 bar and temperatures up to 773 K. This capability was achieved through the inclusion of a ceramic shield and a continuous flow of hot air/nitrogen. To investigate the interaction between the fuel spray and the duct, a stainless steel duct holder was employed, providing the flexibility to explore various configurations. For this particular study, a duct with a diameter of 2 mm and a length of 14 mm was selected, and it was positioned 2 mm downstream from the nozzle exit (referred to as D2L14G2).

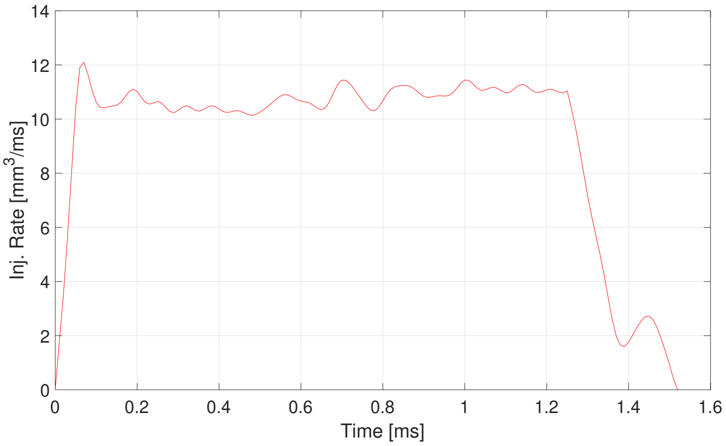

Figure 2.1: Injection Rate at $P_{inj} = 1200$ bar, and $ET = 1000$ µs.

The chosen injection setup for this experimental campaign featured a Bosch CRI1 common rail injector equipped with a single-hole nozzle, which had a diameter of 180 µm. To perform the hydraulic characterization of this injection setup, a proprietary injection analyzer based on the Zeuch Method was employed. In this analysis, the injection rate was determined by conducting injections into a chamber filled with the same fuel used for the injection. When the injection starts, a certain pressure level P_{base} is present in the chamber (10, 20 or 30 bar), and an amount of volume of fuel is forced into the chamber during the injection period. This leads to an increase in chamber pressure, as described by (2.1), where V represents the chamber volume, and k denotes the Bulk Modulus of the fluid. Since the injection rate is defined as the change in volume over time, (2.2) is employed to evaluate the injection rate, illustrating its dependence on the ratio of chamber volume to bulk modulus, as well as the pressure increase observed in the chamber during the injection event [13]. Various tests were conducted and injection rate measurements performed with different energizing times, injection pressures, and back-pressure values; for the present work, the injection rate of interest is the one recorded with an energizing time (ET) of 1000 µs, depicted in fig. 2.1. Furthermore, it is of particular interest to point out how the Start Of Injection (SOI) timing has been detected on the base of the injection-rate measurements; indeed, as discussed and demonstrated in [14], a back-flow is present at the start of the niddle movement causing part of the volume to flow back in the injector. This can be fully appreciated by looking at the time-history of the injected volume, as it will be proposed in sec. 3.3. As a result, the actual SOI for the current injection rate, will be no more fixed with the first non-negative value of injection-rate but at the first non-negative value of injected volume, computed as the integral of the injection-rate curve.

$$\Delta P = \frac{k}{V}\Delta V \tag{2.1}$$

$$\dot{Q} = \frac{dV}{dt} = \frac{V}{k}\frac{dP}{dt} \tag{2.2}$$

The evolution of the spray, both in terms of liquid and vapor penetration, was measured using a z-shaped Schlieren configuration, as illustrated in fig 2.2. These measurements were conducted under low-temperature, non-evaporating conditions. In contrast, under high-temperature, evaporating conditions, back-light measurement techniques were employed. Moreover, concerning the diagnostic setup, a classical Phase Doppler Anemometry (PDA) layout has been employed for drop size and velocity measurements.

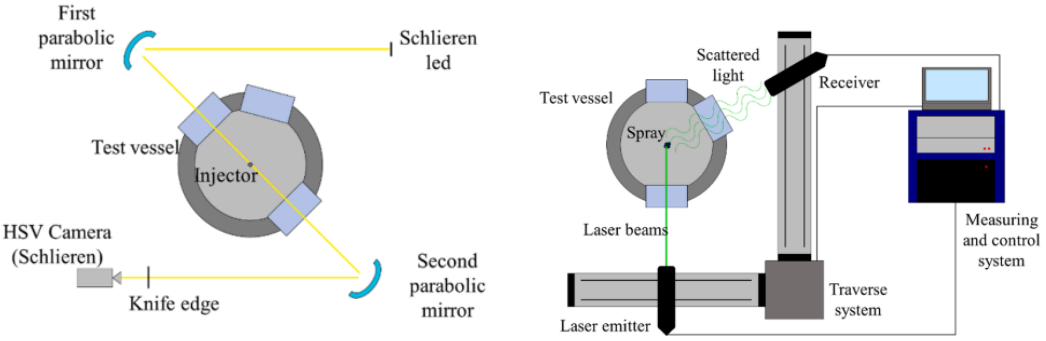

Figure 2.2: *Left*: Z-shaped Schlieren optical setup for spray evolution measurement from [5, figure 1]. *Right*: Phase Doppler Anemometry (PDA) layout frm [5, figure 1].

The comprehensive test plan employed for characterizing the spray evolution through high-speed imaging analysis involved variations in vessel pressure (10 and 20 bar) and injection pressure (400, 800, and 1200 bar), along with variations in vessel temperature (373, 573, and 773 K). However, for the specific case of interest in this work, we will focus on the results obtained under the conditions of $T_{vessel} = 773\ K$, $P_{vessel} = 20\ bar$, and $P_{inj} = 1200\ bar$.

From a qualitative analysis of fig. 2.3 it is possible to appreciate some differences among the free-spray configuration and ducted one, that will be also important for the validation of the numerical model obtained for ECN spray D, were no data are available belonging to DFI setup. Particularly, the spray tip penetration is much faster for DFI cases, "*suggesting the missing momentum flux exchange with the surrounding air in the duct to prevail on the spray-duct wall dissipative interactions*" [5]. Furthermore, in such evaporative configuration, the spray results thinner in DFI case, due to an high evaporation rate.

In summary, tab. 2.1 presents the reference test conditions for this work.

Fuel Type	ISO 4113
Fuel density	824.1 kg/m^3 @T=306K
Fuel Temperature	373 K
Injection Pressure	1200 bar
Vessel Pressure	20 bar
Vessel Temperature	773 K

Table 2.1: PoliTO-UniPG test conditions.

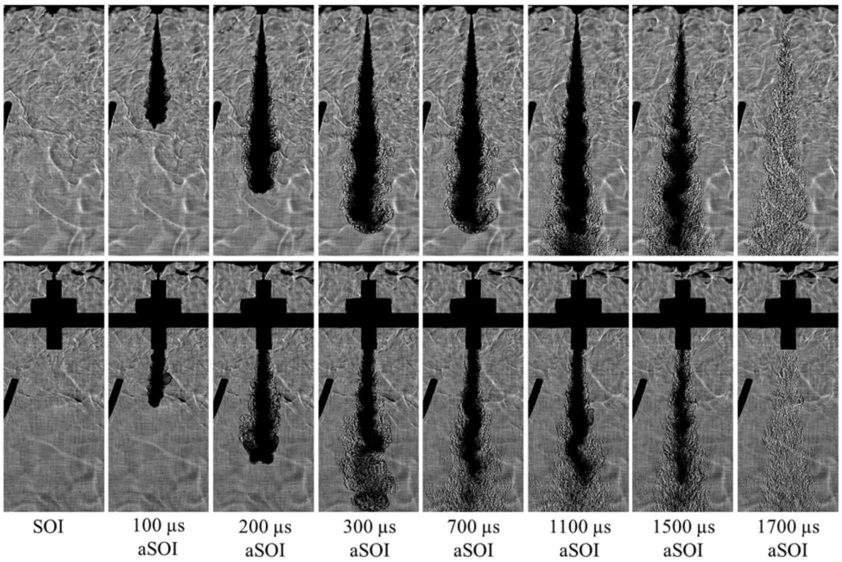

Figure 2.3: Spray evolution for both free spray (top) and duct configuration (bottom). Operating conditions:P_{inj} = 1200 bar, T = 773 K, P_{vessel} = 20 bar, ET = 1000 µs. From [5, figure 5].

2.2 ECN spray D

The Engine Combustion Network (ECN) [15] is a global collaboration involving both experimental and computational researchers in the field of engine combustion. Its primary objective is to establish an online library of experimental data, which serves as a valuable resource for validating combustion models and conducting research in this field.

In the context of the goals of this work, the ECN library was carefully reviewed to identify a spray case that closely matched the injector setup of the PoliTo-UniPG spray model, with particular attention to the nozzle diameter, which was specified as 180 µm in the previous section. As a result of this objective, the Spray D configuration was selected as a future reference case.

Concerning the experimental conditions, the environment in which the experiment is performed is a constant-volume premixed combustion vessel from Sandia equipment, which has a cubic shape with characteristic dimensions of 108 mm. To ensure uniform thermodynamic conditions at injection timing, a fan is employed and can operate at two working points: 8000 rpm and 1000 rpm, in line with the specific equipment being used[1].

The fuel injector is positioned in one side port using a metal insert that forms the right wall of the combustion chamber. Finally, other insers are present to host the sprak plugs, as well as all the sensors needed for measurements purposes. Figure 2.4 illustrates the structure of the combustion chamber, with the images sourced from [15].

The procedure for establishing thermodynamic conditions and the ambient composition follows the well-defined standards of the Engine Combustion Network (ECN). The chamber is designed as a premixed system to simulate conditions similar to those encountered in diesel combustion. In this setup, an ignitable mixture is introduced into the chamber before the experiment begins. Spark plugs, integrated into the chamber's equipment, ignite this mixture. The pre-burn phase is crucial as it helps establish the initial pressure and thermodynamic conditions, as well as the ambient composition in which the fuel will be

---

[1] Refer to the Sandia CV page on the ECN website for further information.

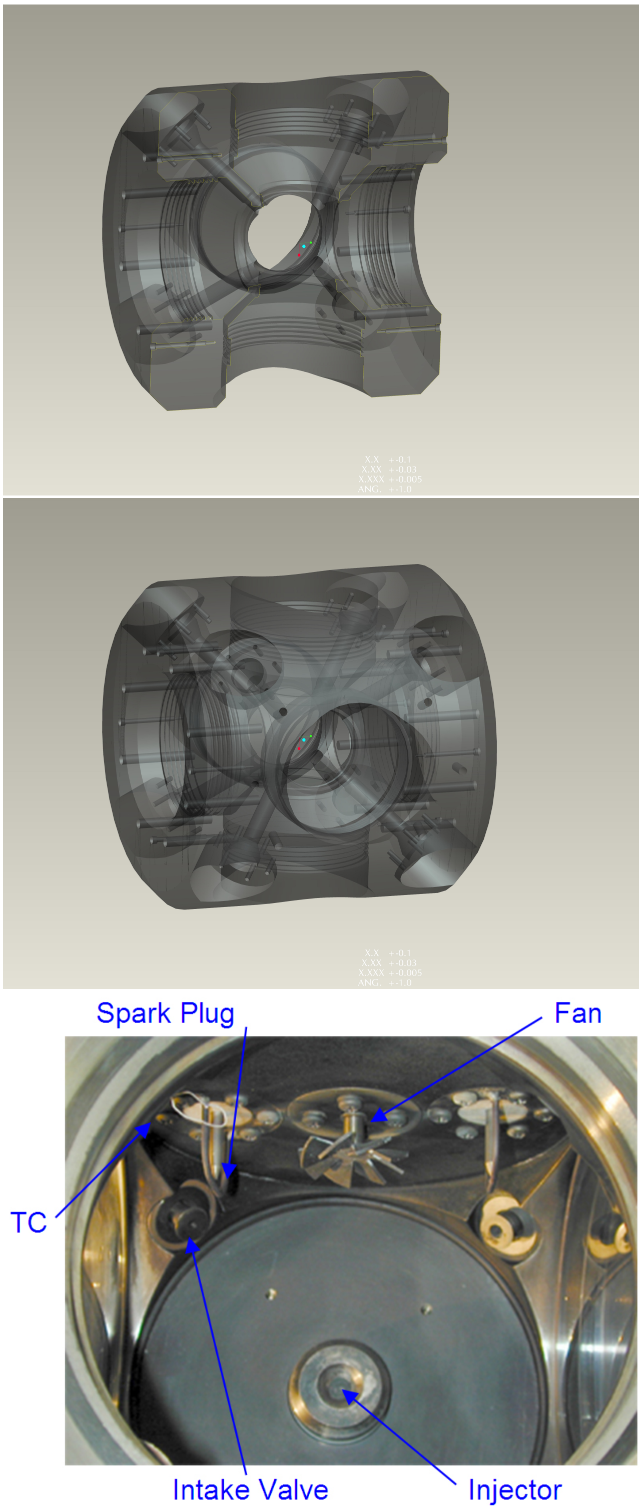

Figure 2.4: Constant-volume Premixed Combustion Vessel. From the top: half-view of the chamber; full view of the chamber; highlight on the chamber equipment. Images sourced from [15].

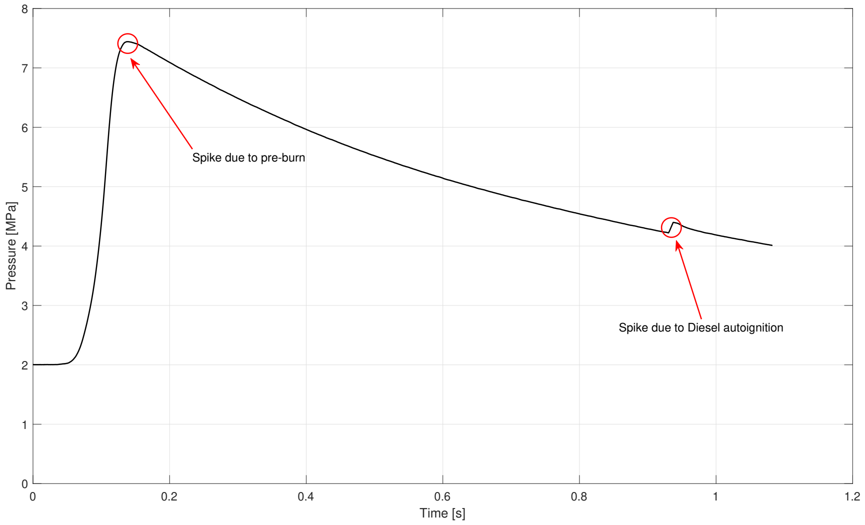

Figure 2.5: Pressure trace prior and at injection timing.

injected at the start of the experiment. Fig. 2.5 shows the pressure trace resulting from the pre-burn of this ignitable mixture; following the pre-burn, there is a cool-down phase lasting approximately 1 second, during which the pressure gradually decreases. As a result, pressure at the injection point serves as a key thermodynamic characteristic, upon which the entire thermodynamic field of the experiment will depend. Additionally, it's important to note that the pressure within the chamber is influenced by the spike resulting from the spark ignition. This spike, in turn, depends on the reactants present in the vessel before the pre-burn phase. As a result, both the ambient composition and the entire thermodynamic field at the injection point are functions of the ambient composition prior to the spark ignition. In the case study, the reactant blend prior to spark ignition is presented in tab. 2.2.

Concerning the fuel used in the experiment, it was a n-dodecane ($C_{12}H_{26}$) ”*in order to enable a complete specification of the chemical and physical properties of the fuel*” [16]. It is injected into the vessel at a pressure of $P_{\text{inj}} = 154$ bar and a temperature of $T_{\text{fuel,inj}} = 363$ K. The chamber's pressure was $P_{\text{vessel}} = 58.9$ bar with a temperature of $T_{\text{vessel}} = 900$ K, resulting in an ambient density of $\rho_{\text{vessel}} = 22.8\ \text{kg/m}^3$. The species composition within the chamber at SOI consisted of N_2 at 89.71%, CO_2 at 6.52%, and H_2O at 3.77%. A summary of these thermodynamic characteristics is provided in table 2.2.

The injector used in the experiment is a single-hole injector (D209134) in an axial configuration. It has a nominal outlet diameter of 180 µm and features a conical shape designed to prevent or limit the onset of cavitation phenomena, as demonstrated in [16] and [17]. The characterization of this injector, including the computation of the rate of injection (ROI), was carried out in [16]. This study highlighted the significant influence of back pressure, injection pressure, and the type of fuel on the rate of injection and momentum flux rate. Of particular interest is the conclusion regarding the dependence of the rate of injection on back pressure and injection pressure when using the same nozzle. Consequently, the final rate of injection can be computed as the product of two terms, according to equation (2.3)

$$ROI = \dot{m} \cdot ROI_{nd} \tag{2.3}$$

where $\dot{m}$ [g/s] is the mass flux which takes into account the effect of back pressure, and

Fuel and Vessel thermodynamic properties	
Fuel Type	n-dodecane ($C_{12}H_{26}$)
Fuel Temperature	363 K
Injection Pressure	1500 bar
Vessel Pressure	58.9 bar
Vessel Temperature	900 K
Vessel Density	22.8 kg/m^3
Ambient Composition prior to spark ignition	
rC_2H_2	3.20 %
rH_2	0.50 %
rO_2	8.25 %
rN_2	88.05 %
Ambient Composition at start of diesel-injection	
O_2	0%
N_2	89.71%
CO_2	6.52%
H_2O	3.77%

Table 2.2: Spray D thermodynamics and ambient composition properties.

ROI_{nd} is the non-dimensional rate of injection obtained for a given injection pressure. In the case study, given a back-pressure of 60 bar and an injection pressure of 1500 bar, the mass flux coefficient is 11.9463 g/s. In fig. 2.6 both the two curves are reported.

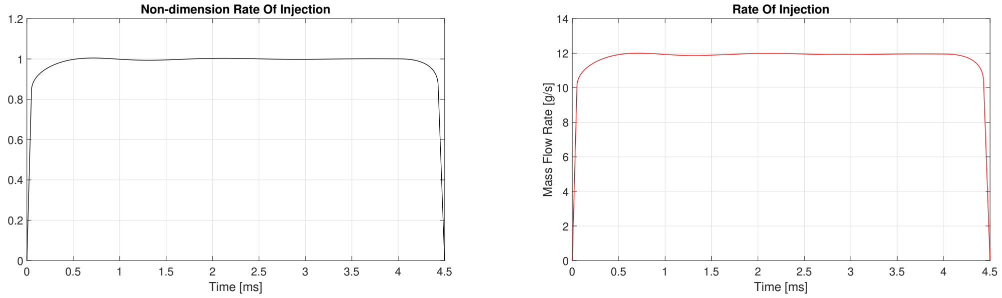

Figure 2.6: Non-dimensional and actual rate of injection (ROI) for D209134 injector. Mass flux coefficient equal to 11.9463 g/s.

In the experimental setup, the diagnostic equipment plays a crucial role, and the ECN provides precise specifications in this regard. For this work, special attention is given to the diagnostic tools used for measuring liquid and vapor penetration.

In the context of vapor penetration measurement, schlieren imaging technique was employed. This technique involves passing a laser light through the vessel and directing it, via a mirror, onto a high-speed camera sensor. Schlieren imaging is sensitive to gradients in refractive index, which arise due to density differences along the line of sight. Consequently, this technique is well-suited for detecting the vapor boundary in the spray. In fig. 2.7 a schematic of such a diagnostic setup is reported.

The measurement of liquid penetration was accomplished using the diffused back - illumination (DBI) imaging technique. This technique relies on light extinction caused by the presence of droplets when light passes through the vessel. It is worth noting that while the ECN also suggests using the Mie-scattering technique for this measurement, DBI

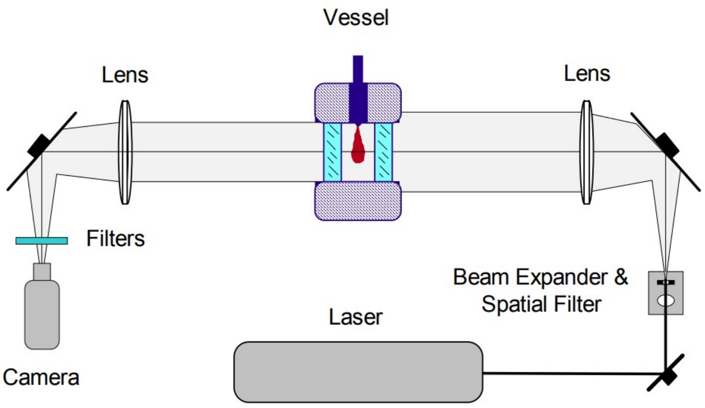

Figure 2.7: Schlieren imaging detection system setup for vapor penetration measurements, Figure from [18, figure 3]

is strongly recommended over Mie scattering.

Figure 2.8 illustrates the time evolution of the spray. As it is possible to notice, the vapor phase can be distinguished from the liquid phase starting from 200 µs aSOI. Indeed, while the liquid length stabilizes at approximately 25 to 30 mm, beyond this region the presence of the vapor phase becomes more pronounced, especially up from 200 µs aSOI, where the vapor length and the liquid length start to diverge. This observation aligns with the data presented in Figure 2.9, where both the actual liquid and vapor penetrations are plotted alongside their respective standard deviations, which consider the measurement uncertainties.

As discussed in the introduction of this chapter, the Spray D test did not employ the duct, and therefore, there are no results available for this specific configuration using this injector and test conditions. Consequently, the experimental results obtained for the PoliTO-UniPG spray are valuable not only for the validation of the correspondent spray model but also for the future validation of the fully predictive Spray D model when coupled with the duct, as discussed in sec. 4.2.7.

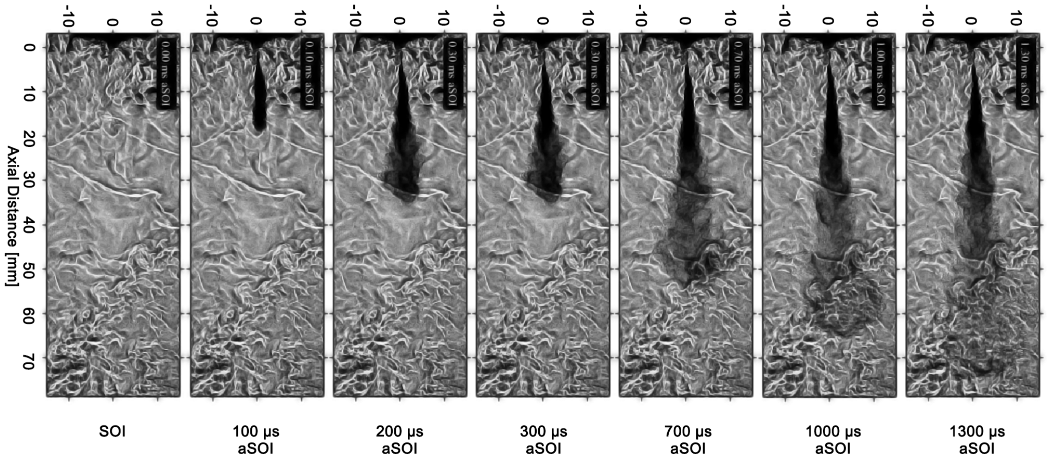

Figure 2.8: Spray evolution for spray D. Operating conditions: $P_{inj} = 1500\ bar$, $T_{vessel} = 900\ K$, $P_{vessel} = 60\ bar$.

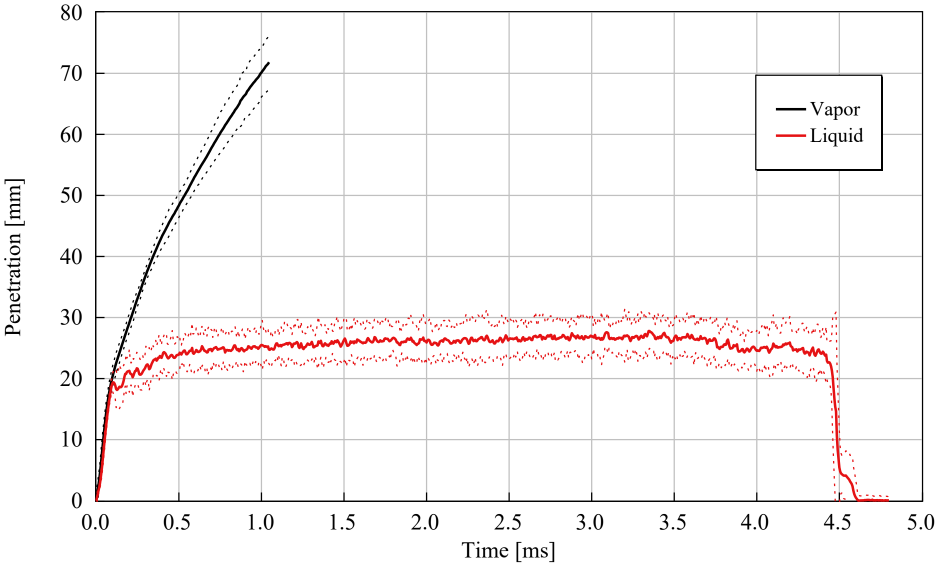

Figure 2.9: Liquid and vapor penetration curves. The continuous line represent the mean value, the dotted line its standard deviation.

Chapter 3

Simulation methodology

The aim of this chapter is to introduce the methodology employed for conducting simulations. The analysis will be conducted in a CFD environment by means of CONVERGE CFD software, using two spray models, both of which have been validated against experimental data. Furthermore, the case setup will be elucidated, including the introduction of the sub-models utilized in both cases. Lastly, two tools developed for generating multi-injection profiles from single-injection profiles will be presented.

3.1 Case Setup Overview

In the development of a reliable CFD simulation model, various aspects require careful consideration. Geometry, boundary conditions, initial conditions, and turbulence setup all play a crucial role in the CFD environment. Below, a summary of the case setups for both the UniPG-PoliTO spray and ECN Spray D is provided, with a particular focus on commonalities and differences between the two setups.

The first step is represented by the CVV reproduction: in this work the same chamber geometry, a cylinder with base diameter of 9 cm and height off 13.8 cm, is used for both models. Concerning the DFI cases, the duct geometry used is the D2L14G2 - 2 mm diameter, 14 mm length and 2 mm stand-off distance - in the standard configuration, i.e. without rounded inlet or taper on the outlet.

In the presentation of the geometry, it is important to underline how the free-spray cases

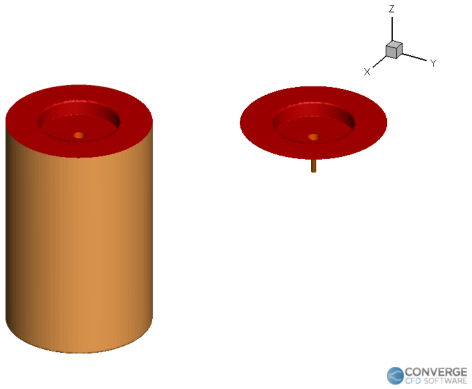

Figure 3.1: 3D view of CVV, duct and injector.

are characterized by the same CVV of the DFI configuration, presented in fig. 3.1, a part for the presence of the duct itself. For what concern the initialization of the setup, in both cases the computational domain is divided in a single region, delimited by the the CVV walls. However, moving to the boundary conditions, in the DFI case it must be taken into account also the presence of the duct, obviously not present in the case of the free-spray. As a result, temperature gradient must be set for the duct wall; in this work, the gradient is equal to zero, thus the initial value of the duct wall temperature is the same of the vessel temperature.

The chosen turbulence model for this simulation is the *Reynolds-Averaged Navier-Stokes* (RANS) transport equation, specifically utilizing the *Re-Normalization Group* (RNG) method. This selection is in agreement with previous studies as [19] and [20], which have demonstrated the superiority of the RNG k-ε model and strongly recommended its use in Diesel simulations. For sake of clarity, it is important to underline that RANS is commonly employed for industrial flow simulations due to its computational efficiency. However, RANS relies on turbulence models, which can introduce uncertainties. On the other hand, *Large Eddy Simulation* (LES) model directly resolves large-scale turbulence structures, providing accurate unsteady flow information. Nonetheless, it demands substantial computational resources, especially for fine grids, making it more suitable for research and specialized applications. As a result, RANS has been chosen for this work especially due to the lower computational power requested.

In the context of the RANS model, the instantaneous drop velocity u_i is split in two terms, a mean component $\bar{u}_i$ and a fluctuating one u'_i respectively. The u'_i is managed by the turbulent dispersion model, in this work the *O'Rourke model* [21]: it is assumed that each component of u'_i follows a Gaussian distribution, described by [21, eq. (1)].

The interaction between drops and walls is modeled using the rebound/slide model, which was initially described by *Naber and Reitz* in [22] and later improved by *Gonzalez et al.* in [23]. This model is named after the two impingement regimes used to simulate the interaction between drops and the wall. The Weber number, defined in (3.1), is used as a variable to determine which of the two mechanisms predominates:

$$We_i = \frac{\rho_1 V_n^2 d_0}{\sigma} \tag{3.1}$$

with ρ density of the fuel, V_n velocity component normal to the surface, d_0 droplet diameter and σ is the surface tension. The rebound regime is stabilized if (3.1) is lower than 80 and, consequently, the drop will rebound elastically with a normal velocity described by [23, eq. (4)], here reported in (3.2):

$$V_{n,0} = V_{n,i}\sqrt{\frac{We_0}{We_i}} \tag{3.2}$$

The definition of We_0 is given on the basis of the work performed by *Wachters et al.* in [24], here reported in (3.3) from [25]:

$$We_0 = 0.678 We_i \exp(-0.04415 We_i) \tag{3.3}$$

On the contrary, if (3.1) is higher than 80, then the slide regime is prevalent and the model proposed by [22] is used to compute the drop velocity.

The interaction between droplets and the wall, as described by the rebound/slide model presented earlier, also results in the formation of a thin liquid film. In CONVERGE, it is possible to account for the evaporation of this film using two models: the *Uniform Temperature model* and the *Discretized Temperature model*. For the purposes of this work, the second model is not activated, and only the first model is employed. The principle behind the *uniform temperature* model for film evaporation is *"an energy balance between four energy terms: convection to the gas, vaporization of the film mass, conduction from the wall and boiling of the film"* [25].

The evaporation of the parcels is governed by the *Frossling correlation* [26]: it is in the role to compute the time rate of change of droplet size.

An important characteristic of the model is the injection size distribution for the droplets. Among the options provided by CONVERGE, *Blob Injection model*, *Chi-squared Distribution model*, *Rosin-Rammler model*, and *Uniform model*, the Blob Injection model, described in [27], was employed in this work. In this model, drops are injected with a diameter equal to the nozzle's effective diameter, which considers the nozzle area while accounting for the discharge coefficient. An important characteristic of this model is the prediction of a liquid core in the region near the nozzle exit, due to the fact that "*the injected blobs breakup due to interaction with the surrounding gas as they penetrate yielding a region of relatively large drops near the nozzle*" [27]. In this sense, the blob injection method does not rely on the assumption of already atomized fuel at nozzle exit, differently from other distribution theories.

In the previous description of the models, the focus was on individual drops. However, considering the vast number of drops that need to be introduced into the computational domain, representing each drop individually is not a practical solution. Therefore, the liquid phase is instead represented using "*parcels*," defined as *"groups of identical drops."*. In this context, the number of parcels injected per nozzle has been shown to be highly significant. *Senecal et al.* in [28] demonstrated how the number of injected parcels per nozzle must be coherent with the mesh resolution employed. In this sense, a more refined mesh should be matched with a higher number of injected parcels to ensure that a cell is not characterized by the presence of a single large parcel; otherwise, the liquid penetration could be artificially increased due to the lower drag resistance faced by larger parcels. Furthermore, the number of injected parcels should also be adjusted in accordance with the total injected mass. A practical relation for computing the total number of injected parcels is: (3.4)

$$N_{parcels} = \frac{m_{tot,inj}}{m_{parcel}} \quad \text{with} \quad m_{parcels} = 1.5 \cdot 10^{-10}\ kg \tag{3.4}$$

where m_{parcel} is the suggested mass for each parcel when the minimum grid size is in between 0.2 and 0.35 mm.

In the context of the process parcels undergo when inside the CCV, one of the crucial aspects is droplet breakup. Breakup modeling is a critical element in spray modeling activites; several options are available in *Converge CFD*, including variations of the *Kelvin-Helmholtz* and *Rayleigh-Taylor* (KH-RT) model, as well as alternative models like *Linearized Instability Sheet Atomization* (LISA) or *Taylor Analogy Breakup* (TAB). For this study, the KH-RT model was chosen because it has been widely used and validated in the literature. It is generally accepted as one of the most reliable models for representing the breakup process in sprays. This model is based on the Kelvin-Helmholtz and Rayleigh-Taylor instabilities that occur between the liquid and gas at the jet interface. These instabilities lead to the formation of wavy structures at the interface, which eventually result in the breakup of droplets into smaller particles. However, given the considerable effect this model has on liquid and vapor penetration, thus on spray modeling, a sensitivity analysis was deemed necessary, as detailed in sec. 4.2.5. For what concern a more detailed explanation of the KH-RT model refers to sec. 3.1.1, 3.1.2 and 3.1.3.

The drag force plays a crucial role in determining the behavior of parcels in various phenomena. Therefore, the accuracy of the drag coefficient C_D computation is of paramount importance. CONVERGE offers several options for modeling drag, ranging from no model to the *sphere* model and ultimately the *dynamic drop drag* model. The choice of the most suitable drag model depends on the specific simulation requirements and the level of accuracy needed for the analysis. The absence of a model for computing the drag coefficient resulted in low accuracy in the obtained results. On the other hand, a *sphere* model considers the parcels as perfectly spherical. Finally, the *dynamic drag* model, that is also the one employed in this work, accounts "*for variations in the drop shape through a drop distortion parameter y*" [25]. In the context of the drop distortion, the TAB model [29] is used, i.e. the one presented in the breakup discussion, for the computation of the drop distortion coefficient y while the relations from [30, eq. (9) and (10)] is used for the actual drag coefficient, here reported in (3.5) and (3.6) respectively. Concerning the computation of y, as explained by *O'Rourke et al.*, the basic idea is to consider an analogy among an oscillating and distorting droplet and a spring-mass system.

$$C_{D_{sphere}} = \begin{cases} 0.424 & Re > 1000 \\ \dfrac{24}{Re}\left(1 + \frac{1}{6}Re^{2/3}\right) & Re \leq 1000 \end{cases} \tag{3.5}$$

$$C_{D_{dyn}} = C_{D_{sphere}}(1 + 2.632y) \tag{3.6}$$

In conclusion, the validation of numerical results against experimental data is of paramount importance. In this sense, both the liquid and vapor penetration curves assume a relevant role. The computation of these two quantities is governed by the "*liquid fuel mass fraction for calculating spray penetration*", "*bin size for calculating vapor penetration*" and "*fuel vapor mass fraction for calculating vapor penetration*" variables of CONVERGE that are set to 0.95, 0.001 and 0.001 respectively. In this way, the liquid penetration is defined as the distance, starting from the nozzle, in which the 95% of the liquid mass is contained.

3.1.1 Kelvin-Helmholtz breakup model

As mentioned in the preceding section, the breakup models hold significant importance for our model, especially concerning spray model calibration and in the context of the sensitivity analysis discussed in section 4.2.5. Therefore, a more comprehensive elucidation of the breakup models incorporated into our model is provided here.

The Kelvin-Helmholtz breakup model is rooted in the study of the Kelvin-Helmholtz instability observed in a liquid jet. This instability was thoroughly investigated by *Reitz and Bracco*, as documented in their work published in [31]. The central concern of their analysis revolved around understanding the stability of a liquid jet with a cylindrical shape characterized by a radius denoted as r_0 and a velocity represented as U during its injection into a stagnant, incompressible, and inviscid gas medium possessing different density properties.

Consequently, the primary aim of the study detailed in [31] was to establish a dispersion relation that relates the real part of the growth rate, denoted as ω_{KH}, with the wavenumber Λ, where Λ is calculated as $2\pi/\lambda_{KH}$. This relation was sought under the condition of an infinitesimal axisymmetric surface displacement, as expressed in (3.7), being applied to the underlying steady-state motion of the system.

$$\eta = \eta_0 e^{ikz+\omega t} \tag{3.7}$$

The numerical solution of this problem was provided by *Reitz* in [27], where both a relation for the maximum growth rate Ω_{KH} and its maximum wavelength Λ_{KH} were given in [27, eq. (4) and (5)], as shown in equations (3.8) and (3.9). This analysis led to the identification of the maximum growth rate and wavelength that occur within the liquid jet just before it undergoes breakup.

$$\frac{\Lambda_{KH}}{r_p} = 9.02\frac{(1+0.45Oh^{0.5})(1+0.4T)^{0.7}}{(1+0.87We_g^{1.67})^{0.6}} \tag{3.8}$$

$$\Omega_{KH}\left[\frac{\rho_l r_p^3}{\sigma}\right]^{0.5} = \frac{(0.34+0.38We_g^{1.5})}{(1+Oh)(1+1.4T^{0.6})} \tag{3.9}$$

Oh is the Ohnesorge number, T is the Taylor Number, We_g is the Weber Number for the gas phase, r_p is the parcel radius and σ is the surface tension. These two critical characteristics are subsequently connected to the time constant introduced into the breakup model. This time constant plays a pivotal role in fine-tuning the Kelvin-Helmholtz breakup process.

In the context of the model, the initial parcel diameter is set as the nozzle hole diameter, according to the *Blob Injection model*. Furthermore, the model is based on the assumption that the new drop, i.e. *child parcel*, radius after breakup, r_c, is proportional to the maximum wavelength obtained in equation (3.8), as described in (3.10).

$$r_c = B_0\Lambda_{KH} \tag{3.10}$$

The proportionality constant B_0 allows for the adjustment of drop radius after breakup, with larger or smaller radii achievable depending on its value. Concerning the breakup timing, it is described in (3.11), where it assumes paramount importance for the model the variable B_1, that will be a calibration parameter for the spray D model, as described in sec. 4.2.5. Particularly, the value of this time constant is dependent on the injector used, and for modeling purpose it can vary from 5 to 100. Furthermore, as anticipated before, τ_{KH} depends on the maximum wavelength and wave number found before. The breakup model, consequently, follows a dynamic law for change of droplet radius, described in (3.12), according which the drops break-up once the breakup timing is elapsed.

$$\tau_{_{KH}} = \frac{3.726B_1r_p}{\Lambda_{_{KH}}\Omega_{_{KH}}} \tag{3.11}$$

$$\frac{dr_p}{dt} = -\frac{(r_p-r_c)}{\tau_{_{KH}}} \tag{3.12}$$

An essential aspect of the model is determining the mass threshold required for a parcel to be classified as a *child parcel*. After breakup occurs, a child parcel is not immediately generated; instead, it is introduced into the computational domain only when the mass of the parent parcel reaches a specific percentage known as the *KH new parcel cutoff*. To identify this condition for creating a new child parcel, the fragmented mass, denoted as m_b and calculated using (3.13), is computed at each breakup step. Additionally, this equation incorporates the *shed factor* s, which represents the percentage of drops undergoing primary breakup. A sensitivity to this factor will be performed in sec. 4.2.3.

$$m_b = \sum_n sN^n\frac{4}{3}\pi\rho_l\left[\left(r_p^n\right)^3 - \left(r_p^{n+1}\right)^3\right] \tag{3.13}$$

3.1.2 Rayleigh-Taylor breakup model

The second mechanism contributing to the breakup phenomenon is the Rayleigh-Taylor instability. This mechanism becomes particularly significant in Diesel applications, where fuel is injected into the chamber at high pressure, subjecting the droplets to substantial deceleration.

The Rayleigh-Taylor instability is a type of interface instability that occurs when two fluids of different densities are involved. Acceleration and density gradients are key factors governing this mechanism. When subjected to pressure and density gradients, the denser fluid displaces the lighter one, leading to the formation of instabilities at the interface between the two fluids. In our application, these instabilities occur at the interface between the air and the fuel droplets.

In contrast to the Kelvin-Helmholtz instability, the breakup time in Rayleigh-Taylor instability depends solely on the maximum growth rate Ω_{RT} associated with this wave instability. The expressions for the maximum growth rate Ω_{RT} and the corresponding wavelength are given in (3.14) and (3.15). These equations depend on gas and liquid densities as well as droplet acceleration. It's worth noting that in CONVERGE, viscosity effects are considered, leading to a modification of these equations and a slightly different formulation, as expressed in [25, eq. (11.77)].

$$\Omega_{RT} = \sqrt{\frac{2}{3\sqrt{3}\sigma}\frac{\left[a(\rho_l - \rho_g)\right]^{3/2}}{\rho_l + \rho_g}} \tag{3.14}$$

$$\Lambda_{RT} = 2\pi\sqrt{\frac{3\sigma}{a(\rho_l - \rho_g}} \tag{3.15}$$

The instabilities in Rayleigh-Taylor waves begin to grow when the droplet radius exceeds Λ_{RT}, hence a mechanism similar to the previously described Kelvin-Helmholtz instability is established. Consequently, Rayleigh-Taylor breakup occurs once the Rayleigh-Taylor breakup time elapses. The resulting child parcels have radii as expressed in (3.16). Furthermore, the expression for the Rayleigh-Taylor time constant is provided in (3.17). The variables C_0 and C_1 correspond to the Kelvin-Helmholtz constants B_0 and B_1.

$$r_c = C_0 \Lambda_{RT} \tag{3.16}$$

$$\tau_{RT} = \frac{C_1}{\Omega_{RT}} \tag{3.17}$$

3.1.3 Hybrid KH-RT breakup model

In the preceding sections, we have presented the Kelvin-Helmholtz and Rayleigh-Taylor breakup mechanisms along with their corresponding CFD models. In this section, we introduce the actual breakup model employed in this work, denoted as an interaction between the two mechanisms (KH-RT model).

Breakup plays a pivotal role in spray formation, comprising two distinct phenomena known as primary and secondary breakup. Primary breakup, associated with atomization, is primarily attributed to aerodynamic forces, particularly due to the high-pressure conditions experienced by droplets upon exiting the nozzle. In contrast, secondary breakup primarily arises from interactions among different fluids.

In this context, the breakup model utilized in both spray models in this work predicts primary breakup using the KH model. Conversely, secondary breakup is modeled with a competitive mechanism between the KH and RT models. To ensure that the RT model is responsible only for secondary breakup, with the primary breakup being handled by KH model exclusively, it is necessary to enable the KH model to create child parcels. This configuration ensures a clear division of roles between the two breakup mechanisms, with the KH model governing the initial atomization (primary breakup) and both KH and RT model addressing further breakup processes (secondary breakup). Concerning the secondary breakup process, the predominant mechanism is determined by the one whose characteristic time elapsed before.

For clarity, CONVERGE provides two different hybrid models, distinguished by the definition of the *breakup length*. In the KH-RT model with a breakup length, the RT model becomes active at a specific distance from the nozzle exit, known as the breakup length. However, based on calibration activities during the development of the PoliTO-UniPG spray model, the ECN Spray model has been configured with the KH-RT model without a breakup length. This configuration enhances the model's reliability in various operating conditions from a breakup perspective.

3.2 ECN spray D

The ECN Spray D simulation setup has been initialized on the base of the correspondent available experimental data.

For the liquid phase, specifically the parcel simulation species, the chosen fuel in this model is the *dodecane* $C_{12}H_{26}$. Since experimental data regarding specific density values were unavailable, no modifications were made to the data provided by CONVERGE. As mentioned in the introduction of this chapter, only a single region within the entire computational domain is defined, bounded by the chamber walls. Therefore, the initialization of pressure and temperature followed the available experimental data. Temperature and density values were available, allowing the chamber pressure to be calculated according to the perfect gas law. Regarding the initial turbulent conditions, no specific data were available, so they were initialized based on the recommendations provided by CONVERGE CFD for the ECN Spray A case. Table 2.1 summarizes the initialization values used for characterizing the CVV.

Temperature	900 K
Pressure	5890266 Pa
Turbulent Kinetic Energy	1 $\mathrm{m}^2/\mathrm{s}^2$
Turbulent Dissipation	100 $\mathrm{m}^2/\mathrm{s}^3$

Table 3.1: Region (*vessel*) initialization values.

Regarding the initial values for the breakup models, the values suggested by CONVERGE for Diesel simulations were adopted. Table 3.2 presents these suggested values. In terms of injector properties, the discharge coefficient was calculated by considering the theoretical mass flow rate through the nozzle based on the nozzle radius, and the pressure gradient between the rail pressure P_{inj} and the vessel pressure P_{vessel}, as well as the actual experimental mass flow rate $\dot{m}$, as shown in equation (3.18). This calculation resulted in a discharge coefficient of $C_d = 0.98$. Additionally, the near cone angle was computed using the Heywood model [32, eq. (10.16)], as given in equation (3.19). In this equation, c_1 is a constant that depends on the nozzle geometry and can vary between 0.26 and 0.4, while c_2 is equal to 0.0043 for vaporizing sprays or 0 for non-vaporizing sprays.

$$C_d = S\frac{\sqrt{2\rho_f(P_{inj} - P_{vessel})}}{\dot{m}} \tag{3.18}$$

$$tan(\vartheta/2) = c_1\left[\left(\frac{\rho_a}{\rho_f}\right)^{0.19} - c_2\left(\frac{\rho_f}{\rho_a}\right)^{0.5}\right] \tag{3.19}$$

Kelvin-Helmholtz Model (KH)	
Fraction of injected mass/parcel	3%
Shed Mass Constant	1
Model Size Constant	0.6
Model Velocity Constant	0.188
Model breakup Time Constant	7
Rayleigh-Taylor Model (RT)	
Model breakup Time Constant	1
Model Size Constant	0.6

Table 3.2: Breakup models initial values.

3.3 Injection Rate tool for multi-injection analyses

The aim of this section is to present a tool developed to create multi-injection profile starting from experimental data of single-injection profile.

Within the realm of multi-injection strategies, there was a demand for diverse injection profiles to perform simulations. To meet this need, two separate MATLAB tools were created specifically for this purpose. The first - a simplified version - allows the creation of split-profile only; on the other hand, the second tool features a more intricate and robust architecture. It empowers the user to specify various parameters, including the number of injection events, the total fuel quantity to be injected in the entire injection profile, the allocation percentage for each injection event, and the dwell time. Additionally, the user can select whether to employ an electric or hydraulic dwell time. The complex tool can be utilized when several injection profiles are available for the same injection pressure and a range of energizing times. In contrast, the simplified version can be employed when only an injection rate curve is available. In this case, the user cannot choose the total injected mass but must use the value corresponding to the experimental curve. However, it is possible to to split this mass into two injection events with a proper dwell time.

The tools working principle is based on different tasks:

1. Acquisition of injection-rate experimental data and re-sampling;
2. Detection of the Start of Injection timing (SOI);
3. Isolation of the single-injection rate shape;

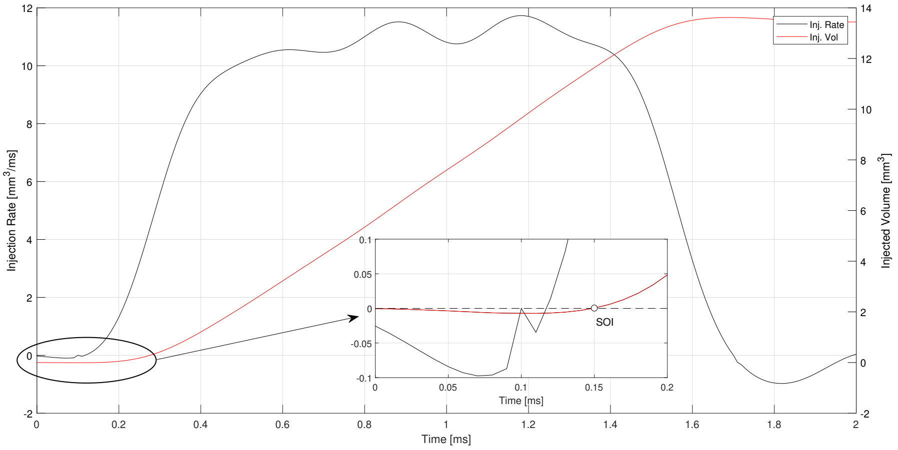

Figure 3.2: SOI detection with Injection Rate and Injected Volume curves.

4. Creation of the multi-injection profile based on user inputs;

The initial task involves retrieving data from a database, encompassing injection rate, injection current, and sampling frequency information. Subsequently, the acquired data is subjected to a resampling process to enhance accuracy for subsequent operations, resulting in a higher data point density. The final sampling interval has been configured to be 0.0001 ms for this purpose.

The second task, i.e. start of injection timing detection, is carried out considering the precise time instant in which the fuel starts to enter in the combustion chamber; indeed, the injection event is characterized by a first backflow when the needle starts its movement for injector opening. This is related to a reduction of the pressure in the chamber due to the increment of its volume. This backflow results in a negative initial injected volume.

In this context, the tool proceeds with the computation of the injected volume, i.e. cumulative integral of the injection rate, looking for the first point where it becomes higher than zero after beginning of the backflow. In fig. 3.2 the SOI detection point method is illustrated with reference to the case at injection pressure $P_{rail} = 1200\ bar$ and energizing time $ET = 900\ \mu s$.

Once the start of injection timing has been detected, it is possible to isolate, from experimental data, the single-injection rate shape. The obtained profiles are going to be the references for the creation of the multi-injection ones. In fig. 3.3 are illustrated the curves obtained.

While the steps described so far are identical in both versions, the subsequent part of the procedure diverges between the two case, at least to some extent; for what concern the simplified tool refers to section 3.3.1 for mote detail. In the following, the operational principles of the complex version will be elucidated.

As mentioned above, the user is asked to prompt the number of injection events, the amount of fuel to be injected in the whole profile, as well as the dwell time. Focusing on the first two inputs, three different cases can be faced, with reference to fig. 3.3:

1. The amount of fuel to be injected in an injection event is less than that injected with the rate-shape profile featuring the shortest energizing time (ET = 175 in fig. 3.3);

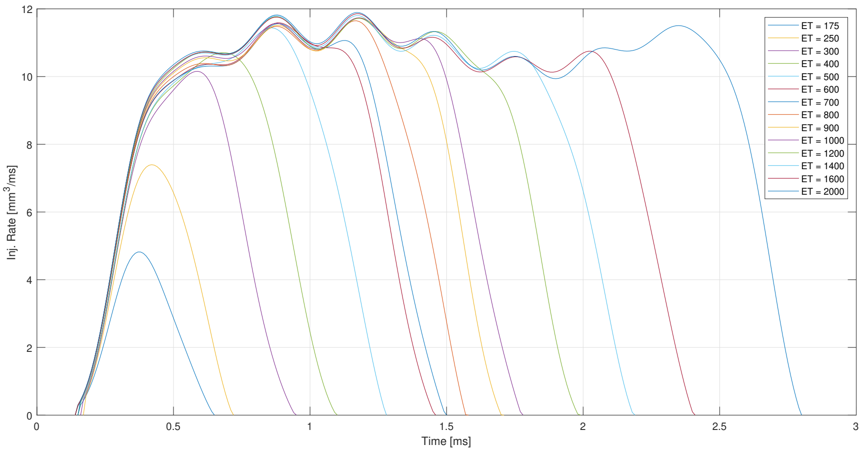

Figure 3.3: Rate Shape Curves obtained for different energizing time (ET).

2. The quantity of fuel to be injected in an injection event falls within the range of that injected in the experimental data curves (ET = 175 - ET = 2000 in fig. 3.3);
3. The quantity of fuel injected in an injection event surpasses that of the curve with the longest energizing time (ET = 2000 in fig. 3.3);

The procedure by which the curve will be obtained is, in every case iterative: given the amount of fuel to be injected it is computed, using a simple linear relation with the experimental data, reported in (3.20), the correspondent injection duration, defined in this case as the time between the SOI and the instant at which the injection rate approaches again to zero. The DOI obtained in this way represents a first attempt then corrected by an iteration procedure.

$$DOI_{new} : Inj_{vol,new} = DOI_{exp} : Inj_{vol,exp} \tag{3.20}$$

Subsequently, once the End of Injection (EOI) timing for that specific injection event is determined, the curve representing the closing of the injector, i.e. *drop in the injection rate curve*, which corresponds to a higher amount of fuel compared to the user's selection, is adjusted. First, it is shifted to the left, aligning it with the EOI point detected, and then connected with the upper portion of the rate shape curve. This adjustment is made to ensure that no sharp peaks are present in the final injection rate profile. It's crucial to note that scaling the existing curves alone would not suffice because the maximum amplitude of the injection rate is restricted by the injection pressure.

Finally, the integral of the modified curve is computed to ensure that the resulting injected volume matches the user's specified fuel quantity. To minimize errors stemming from potential non-linearity between the Duration of Injection (DOI) and injected volume, as instead supposed in (3.20), the DOI related to the new injection event is corrected. This is achieved by adding or subtracting a certain number of samples n to the computed DOI. Hence, the experimental data was initially resampled to ensure a more accurate determination of the actual DOI. In a sparsely sampled dataset, adding or removing a sample point could result in injecting more or less fuel than the user's input. This correction process ensures that the injection duration is adjusted to match the corrected DOI, which in turn affects the injected volume. With each iteration of correction, the closing curve of the injection rate is adjusted accordingly. Figure 3.4 illustrates the two curves obtained through this process.

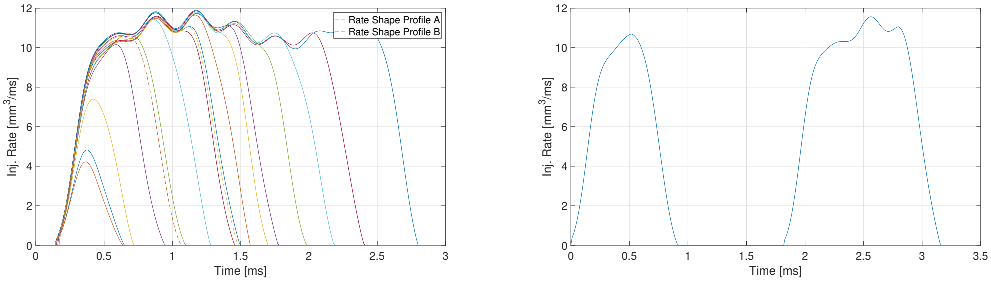

Figure 3.4: Experimental rate shape curves (continuous line) and computed rate shape curves (dotted line). The computed ones refer to a total injected fuel volume equal to 17 mm^3 and a split ratio among the injection events of A = 36%, B = 64%.

The described approach is applicable to the second case, while for the first case, it is possible to directly refer to the simplified version of the tool in sec. 3.3.1. Indeed, the approach remains the same, involving the creation of multiple virtual curves within the range of injected mass, ranging from zero up to the value corresponding to the lowest energizing time.

In the third case, where the fuel quantity to be injected is greater than that injected during the curve with the highest ET, an extrapolation of the curve is performed instead of an interpolation. While the computation of the Duration of Injection (DOI) remains consistent with the previous method, in this case, there is not a reference curve with a higher injected fuel quantity. Therefore, the last curve is partially duplicated a number of times to facilitate the matching, based on its integral, of the fuel volume specified by the user. In figure 3.5 the A curve was found applying such extrapolation method.

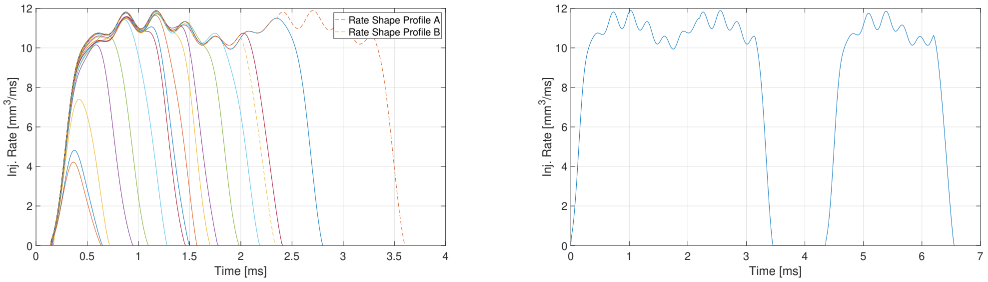

Figure 3.5: Experimental rate shape curves (continuous line) and computed rate shape curves (dotted line). The computed ones refer to a total injected fuel volume equal to 55 mm^3 and a split ratio among the injection events of A = 63%, B = 37%.

As mentioned earlier, the advanced tool provides the capability to control the dwell time, offering the choice between hydraulic and electric dwell time. In the former case, the dwell time specified represents the actual time interval between the two injection events. In the latter case, however, the user-defined time interval is taken as the duration between the start of the drop in the current signal for the first injection event and the commencement of the rise in injection current for the second injection event. Consequently, the hydraulic dwell time is calculated on the base of experimental injection current data, taking into account of the electric dwell time, opening and closing delay for the injector, as described in (3.21), where $DT_{hydraulic}$ is the hydraulic dwell time, $DT_{electric}$ is the electric dwell time, OD_{inj} and CD_{inj} are the opening and closing delay related to the injector.

$$DT_{hydraulic} = DT_{electric} + OD_{inj} - CD_{inj} \tag{3.21}$$

3.3.1 Simplified tool

As mentioned in the preceding section, the simplified tool encompasses only a portion of the code found in the more complex version, allowing for a subset of the operations available in the latter. Specifically, the simplified tool is capable of creating only split-injection profiles. Additionally, it lacks the capability to interpolate data to obtain new curves, handling one curve at a time compared to the complex version. For the purpose of this work, the simplified tool was used to create the split-injection profiles used in simulations.

While the initial tasks of detecting the start of injection (SOI), extracting rate shape data from raw data, and resampling are performed similarly to the complex version, a different approach is employed here to create the injection profile. The drop curve of the rate shape is extracted, and multiple curves are generated by linking this curve to the nominal rate shape at each sampling time starting from the end of the rise curve, as depicted in fig. 3.6. The corresponding mass for each curve is computed and stored in an array. Subsequently, the computed masses are compared to the mass of each injection event set by the user, selecting the curve that minimizes the error.

The rate shape curves separately obtained for the two injection events are then concatenated, considering the dwell time specified by the user, which in this case can only be hydraulic. An example for each spray data - PoliTo-UniPG and ECN Spray D - of the profiles obtained with this tool is reported in fig. 3.7.

To clarify, the tool works effectively with both the PoliTO-UniPG spray and the ECN Spray D data. However, in the former case, the input for the tool is the total injected volume of fuel, while in the latter case, the inputs are configured based on the total injected mass, aligning with the available experimental data.

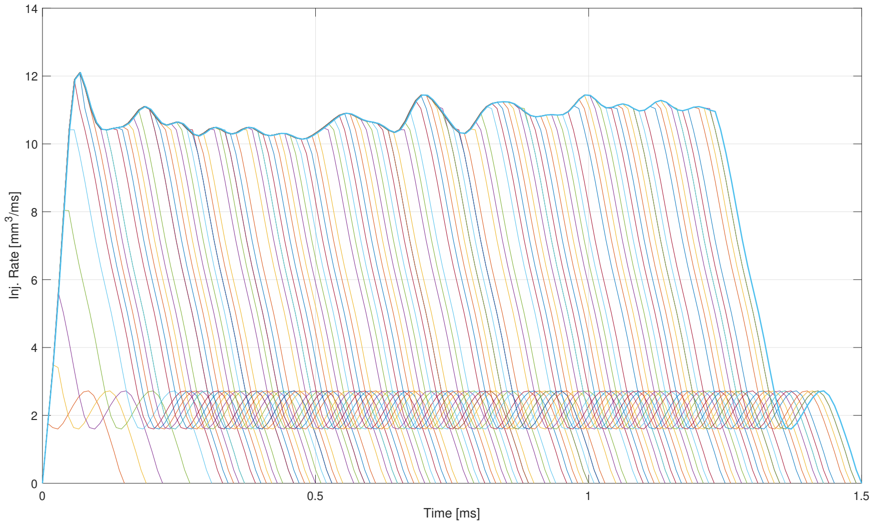

Figure 3.6: Curves obtained from PoliTO-UniPG Spray data by concatenating the nominal curve and the drop one at each sampling instant with a sampling time equal to 1 ms.

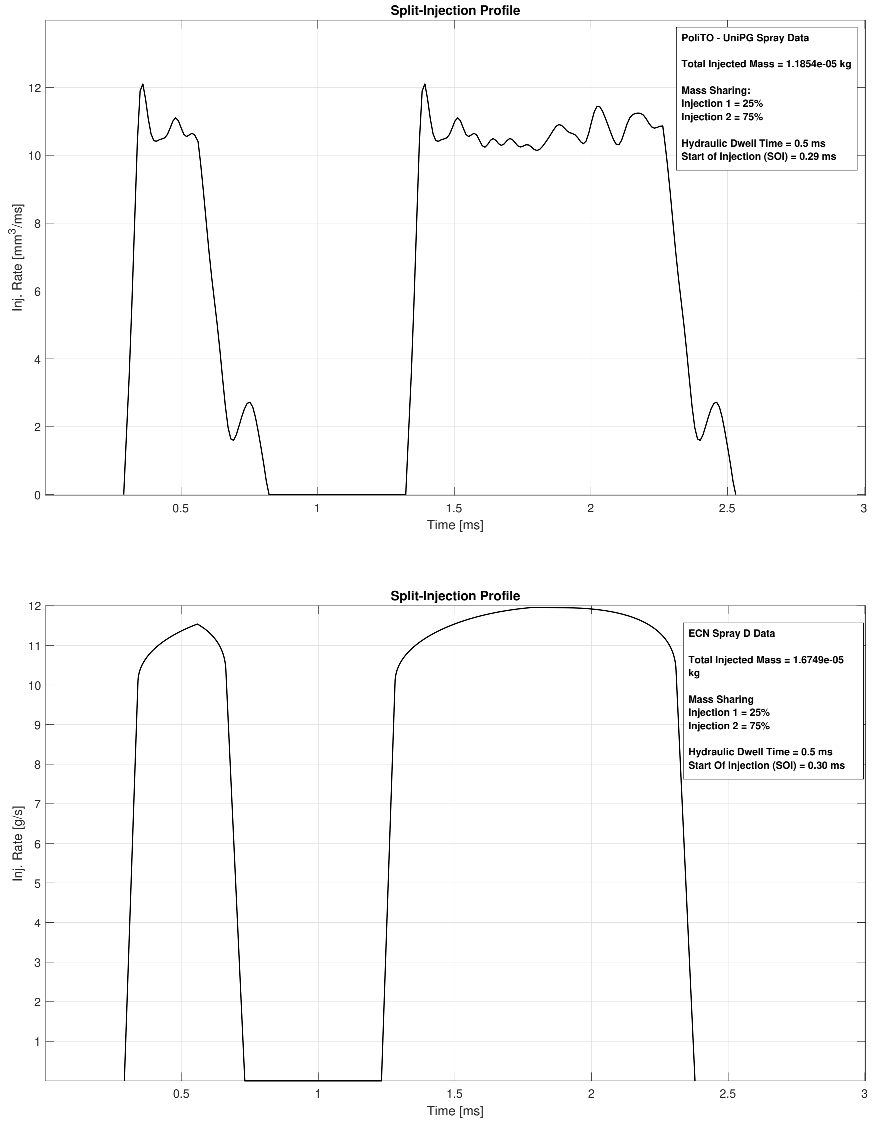

Figure 3.7: Split-profile obtained using the split tool. The top profile is derived from PoliTO-UniPG spray data, while the bottom profile is from ECN Spray D data. The mass is distributed with 25% in the first injection and 75% in the second injection.

Chapter 4

Spray models calibration and validation

4.1 PoliTO-UniPG spray chamber

The 3D CFD simulation methodology and the calibration process for the PoliTO-UniPG spray model have been extensively detailed in [33] and [5]. This section provides a concise overview of the validation techniques applied to the spray model and offers a glimpse of the numerical results achieved. For a more comprehensive understanding of the calibration and validation process, please refer to the referenced articles.

The initial step involved a grid sensitivity analysis, which included testing various base grid sizes to determine the maximum base grid dimension that ensures result convergence. The minimum grid size obtained in the computational domain is scaled accordingly thanks to AMR and Fixed Embedding techniques[1]. Subsequently, the calibration process focused on the analysis of the breakup models and the calibration of their key parameters. Additionally, to account for the high-pressure gradient, the assumption of super-cavitation was applied. As a result, the discharge coefficient was refined, leading to a reduction in its value compared to the one calculated based on the mathematical relationship outlined in the previous chapter. In this way, a further shrinkage effect on the nozle area is obtained. Lastly, the collision model was deactivated for this particular model.

It is worth noting that the set of experimental data encompasses various test conditions, including data for both free-spray and DFI equipment in terms of liquid and vapor penetration obtained at different rail pressure, $P_{inj} = 800\ bar$ and $P_{inj} = 1200\ bar$, vessel pressure, $P_{vessel} = 10\ bar$ and $P_{vessel} = 20\ bar$, and different vessel temperature, $T_{vessel} = 573\ K$ and $T_{vessel} = 773\ K$. In this context, the spray model was initially calibrated using a reference free-spray case with the following conditions: $P_{inj} = 1200\ bar$, $T_{vessel} = 573\ K$, and $P_{vessel} = 20\ bar$. For the thesis work, the thermodynamic conditions are identical, except for the vessel temperature, which is $T_{vessel} = 773\ K$.

Figure 4.1 presents the final numerical and experimental liquid penetration curves for both free-spray and DFI configurations, both for the calibration case and the case of interest in this thesis work[2]. The grey boxes were added because experimental data could not be obtained in that region; indeed, the duct is not optically-accessible, and the imaging window length is limited to 50.0 mm. In general, it is possible to notice a good agreement among numerical and experimental data for both temperature conditions. A slight discrepancy is

---

[1] More detailed information about how scaling is implemented with these two techniques can be found in sec. 4.2.1.

[2] Refer to [5, Appendix A] for the numerical validation under different test conditions.

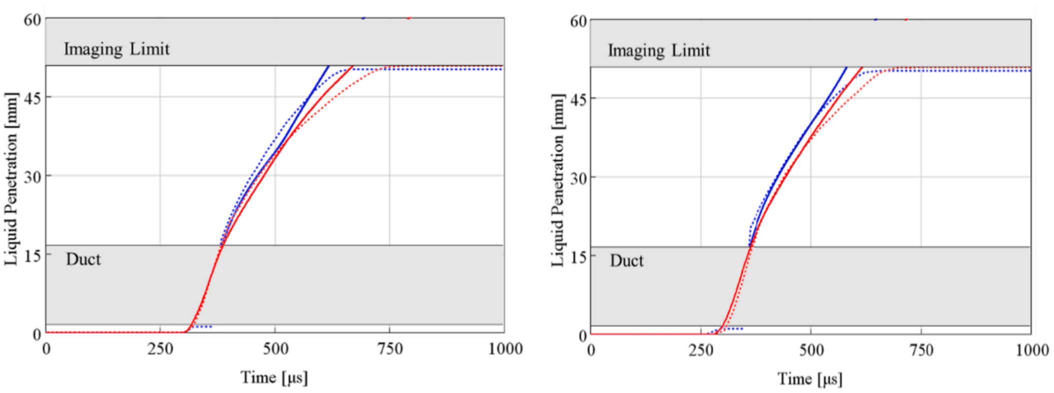

Figure 4.1: Numerical (*solid line*) and experimental (*dotted line*) liquid penetration curves for both free-spray (*red*) and DFI (*blue*) conditions at $P_{inj} = 1200\ bar$, $T_{vessel} = 573\ K$ (*left*) and $P_{inj} = 1200\ bar$, $T_{vessel} = 773\ K$ (*right*). From [5, figure 23A and figure 24A].

found close to the imaging limit for the case with $T_{vessel} = 773\ K$. However, "*the error was considered as acceptable for automotive engine applications taking into account the typical piston bore size*" [5]. For both tested temperature, a faster and higher liquid penetration length is obtained for the DFI cases compared to the free-spray ones.

4.2 ECN Spray D

The development of the ECN Spray D spray model involved several key steps. Similar to the PoliTO-UniPG spray model, it began with a grid sensitivity analysis. Following that, an exploration of various model parameters was conducted. The calibration process focused primarily on different injection parameters, such as cone angle and KH time constant, using a Design of Experiments (DOE) approach. Table 4.1 presents the initial values for the calibration parameters under consideration. The values related to the breakup models were based on CONVERGE recommendations for Diesel spray, as already presented in sec. 3.2; on the other hand, the discharge coefficient and cone angle were computed using experimental data. However, a sensitivity analysis was performed as these values were derived from simplified mathematical model and were not directly measured in experiments, potentially leading to variations from the computed values.

C_d	0.98
ϑ	15.5°
B_1	7
Shed Mass Constant	1
Turbulent Kinetic Energy	1 m^2/s^2
Turbulent Dissipation	100 m^2/s^3

Table 4.1: Calibration parameters initial values.

The validation of the model is carried out based on experimental data, primarily for the free spray scenario. However, this validation approach is not applicable to DFI due to the absence of relevant experimental data. In the case of free spray, the validation process involves comparing numerical results, such as liquid and vapor penetration curves, with their corresponding experimental counterparts; Furthermore, a qualitative assessment of the

	Scale factor	Length [mm]	Top base radius [mm]	Bottom base radius [mm]
Bigger Truncated Cone	2	35	2	9
Smaller Truncated Cone	3	7	1	2

Table 4.2: Fixed Embedding Geometries Dimensions for ECN Spray D model in free-spray condition.

spray's shape is conducted by comparing numerical spray representations with experimental images. For the DFI case, since experimental data is lacking, validation relies on prior knowledge and the numerical results obtained from the PoliTO-UniPG DFI spray model.

4.2.1 Grid Sensitivity

The domain in CONVERGE is discretized by different grid sizes. Firstly, the whole computational domain is discretized by a base grid; then *Fixed Embedding* and *Adaptive Mesh Refinement* (AMR) techniques could be used to refine the domain discretization.

The base grid, i.e. the *coarse* one, is built up with cubes of dimension $dx = 2\ mm$: this is a crucial dimension for the whole discretization approach. Indeed, both the cube dimensions obtained with fixed embedding and adaptive mesh refinement techniques are related to the base grid by means of a scale factor, according to (4.1):

$$d_{x,final} = \frac{d_{x,base}}{2^{f_{scale}}} \tag{4.1}$$

where $d_{x,final}$ is the cube dimension obtained with fixed embedding or AMR. The importance of employing a precise grid dimension is closely tied to the dependence of sub-models used for breakup, drag, evaporation phenomena, turbulence, etc., on the grid dimension itself. However, although reducing the grid dimension could potentially alleviate this dependency, it would also lead to increased computational power and time requirements. In this context, a trade-off between these conflicting requirements becomes crucial.

Going into further detail about the two techniques used for fixed embedding, two truncated cones have been employed. The first cone is characterized by a scale factor of 2, resulting in a minimum grid size of $dx = 0.5\ mm$ in this region. Additionally, it extends 35 mm into the chamber and has a top base radius of 2 mm and a bottom base radius of 9 mm. On the other hand, the second cone is smaller but achieves a higher grid resolution with a scale factor of 3, resulting in $dx = 0.25\ mm$. It has a length of 7 mm, a top base radius of 1 mm, and a bottom base radius of 2 mm. As a result, the second truncated cone is automatically nested within the larger one. The reason for using these two cones lies in the fact that the nozzle region is characterized by the most complex flow-behaviour as well as the complexity of the coupling among the liquid and gas phase, whereas lower resolution is sufficient as one moves farther away from that region. The dimensions of the two geometries are reported in table 4.2.

Conversely, adaptive mesh refinement technique enables higher resolution depending on specific events, significantly reducing the computational power required for simulation compared to the one required if the same grid scale would be used for the whole simulation time. In this context, a scale factor of 3 has been applied, allowing for a uniform grid spacing of $dx = 0.25\ mm$ across the entire region. Activation criteria for adaptive refinement are based on velocity and temperature gradients.

As previously noted, all the sub-models employed in the simulation are contingent on grid resolution. Consequently, the objective here is to determine the maximum grid dimension at

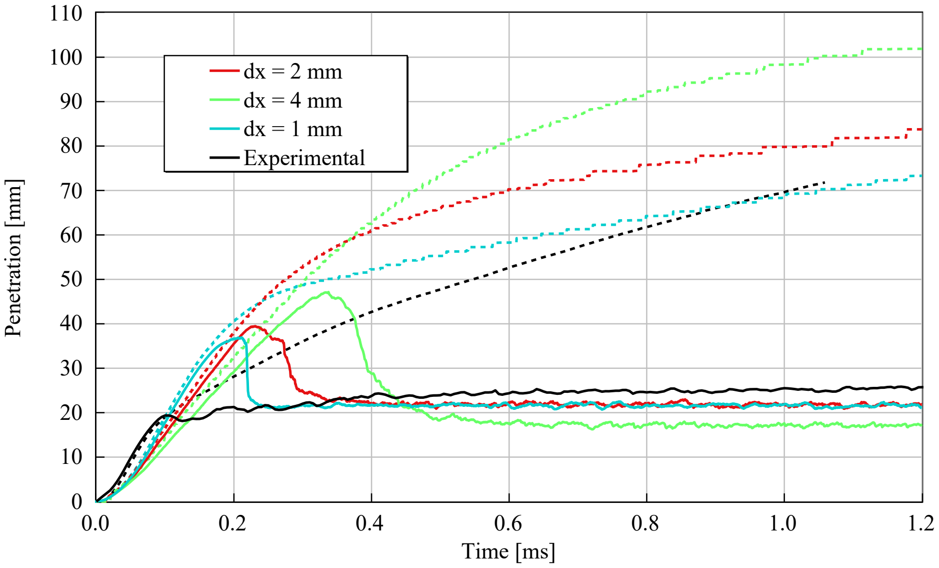

Figure 4.2: Grid sensitivity: liquid (*continuous line*) and vapor (*dashed line*) penetration curves for different base grid size.

which the solution converges, thus becoming independent on grid resolution. To achieve this, three distinct base grid dimensions were tested: $dx = 1\ mm$, $dx = 2\ mm$, and $dx = 4\ mm$ respectively. The results, particularly in terms of liquid and vapor penetration, are presented in fig. 4.2.

Excluding the transient phase and focusing solely on the steady-state liquid length, it can be affirmed that it becomes independent of the grid dimension starting from $dx = 2\ mm$. Specifically, the liquid length obtained with $dx = 1\ mm$ is the same as that obtained with $dx = 2\ mm$. However, this independence does not extend to the transient phase, where the smallest grid size helps reduce the first peak. Nevertheless, as will be discussed in subsequent sections, the first peak is influenced by factors beyond grid resolution and will be addressed differently. This is primarily due to the significantly higher computational power required to handle a base grid of 1 mm, which would result in a minimum grid size of 0.125 mm when using fixed embedding and AMR techniques. In this regard, a plot depicting the computational power required to handle the smallest grid dimension is presented in fig. 4.3. It's evident that in the case of $dx = 1\ mm$, the computational power needed for numerical solving of the entire domain is one order of magnitude higher compared to the other two cases. On the right side of fig. 4.3, the total number of cells is presented for various grid sizes over time. This plot illustrates the contribution of Adaptive Mesh Refinement (AMR), as evidenced by the increase in the total number of cells. Without AMR, the total cell count would remain constant over time. Furthermore, in accordance with the smaller grid size, the number of cells in the computational domain with $dx_{base} = 1\ mm$ is one to two orders of magnitude greater than in the case of the smaller grid size. The grid structure in the CVV is reported in fig. 4.4. Since the bigger cone is superimposed on the smaller one, in fig. 4.4, only the larger truncated cone is visible.

4.2.2 Time-step Sensitivity

In the previous section the grid resolution effects were discussed. However, it was anticipated that no actions have been taken on grid resolution based on the transient phase of the liquid

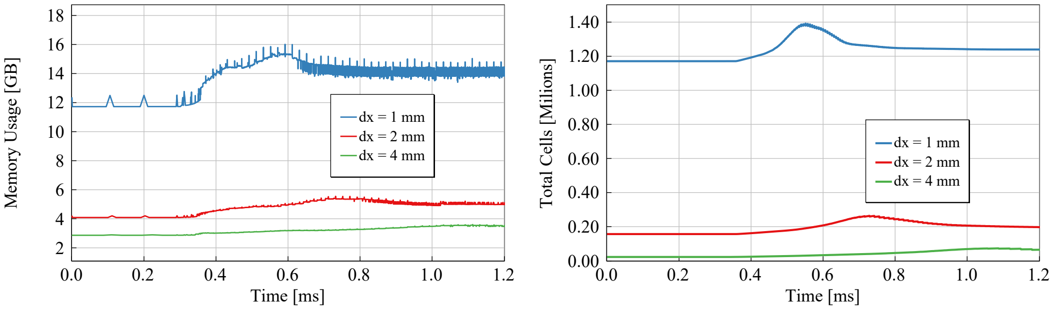

Figure 4.3: *Left*: Computation power for different grid sizes. *Right*: Total number of cells for different grid size.

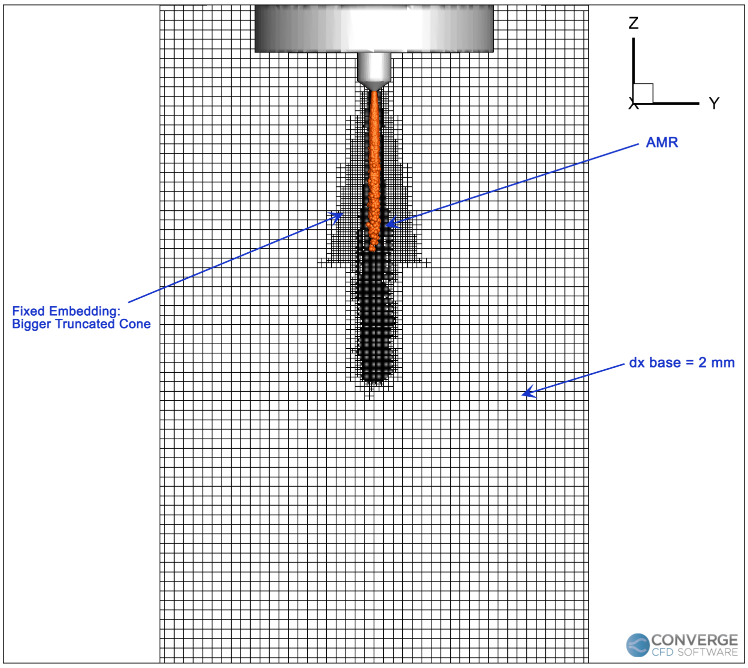

Figure 4.4: Grid structure in the computational domain for ECN Spray D in free spray condition.

penetration. Indeed, it is of higher interest to analyse the time-step used to numerical compute the solution.

In the context of numerically computing the solution, CONVERGE provides two distinct options, allowing the user to choose between a *fixed time-step* and a *variable time-step*. In this study, the latter option is utilized. When employing a variable time-step, CONVERGE conducts various checks to determine the size of the next time-step, ultimately selecting the maximum time-step that satisfies all of these criteria. Detailed information regarding these constraints can be found in [25, Table 3.1]. Consequently, while the current time-step is typically governed by the Convection Courant-Friedrichs-Lewy (CFL) condition, the focus here is on adjusting the maximum time-step, denoted as dt_{max}, used during the simulation.

In fig. 4.2, the dt_{max} was set to $2e-06\ s$ up from $t = 0.27\ ms$ till the end of the simulation; however, such a time-step could be not sufficiently small to describe properly

Default			A			B	
Time [ms]	Time-step [s]		Time [ms]	Time-step [s]		Time [ms]	Time-step [s]
0	0.01		0	0.01		0	0.01
0.27	2e-06		0.29	5e-08		0.29	5e-08
			0.43	1e-07		0.55	1e-07
			0.71	2e-06		0.71	2e-06

Table 4.3: Default, A and B time-step profiles.

that phase. In this framework, a sensitivity on the time-step has been performed.

Firstly, the time-step was increased for the part of the simulation primarily involved in the transient rise of the liquid penetration, in accordance with fig. 4.2, as outlined in tab. 4.3, time-step profile A. As previously, the results pertaining to liquid and vapor penetration are depicted in fig. 4.5. As anticipated, the peak is influenced by the time-step used; a reduction in the time-step led to a dampening of the peak, although it is still evident even with the new time-step profile. However, convergence of results at steady-state conditions is achieved even with the highest time-step.

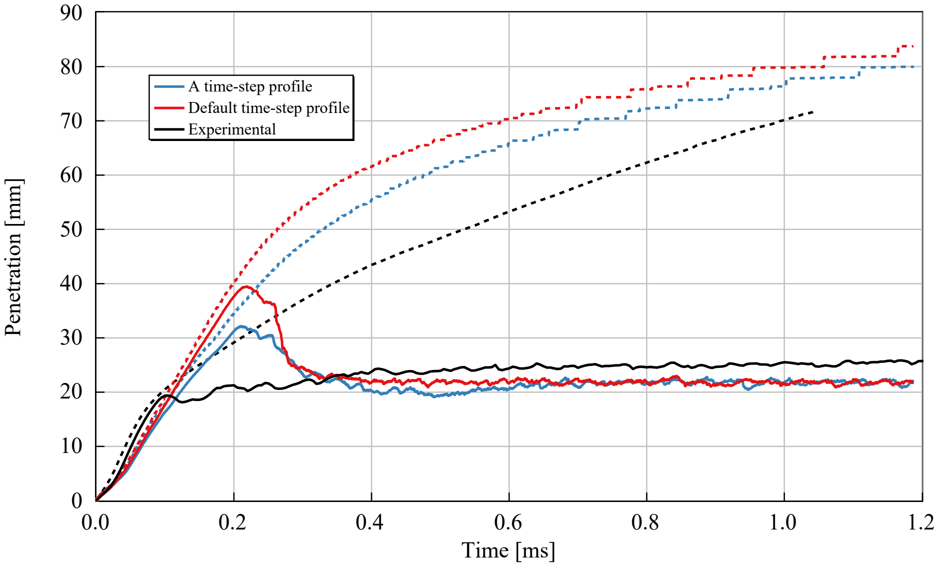

Figure 4.5: Time-step sensitivity: liquid (*continuous line*) and vapor (*dashed line*) penetration curves. "Default time-step profile" refers to $dt_{max} = 2e-06\ s$ while "A time-step profile" refers to the one with $dt_{max} = 5e-08\ s$ as presented in tab. 4.3.

In order to obtain a further reduction of the peak, it was further increased the part of the simulation solved with a time-step $dt_{max} = 5e-08\ s$, thus solving with the time-step profile B in tab. 4.3. The correspondent liquid and vapor penetration curves are displayed in fig. 4.6. The expansion of the simulation duration with the smallest time step, i.e., $dt_{max} = 5e-08\ s$, did not completely eliminate the peak. Instead, it only attenuated the tail end of the peak. Consequently, this alone does not justify the increased computational power required to solve a longer portion with this time-step.

The results obtained thus far emphasize that the first peak in the liquid penetration curve is influenced not only by the time-step used for numerical solving but also by various other

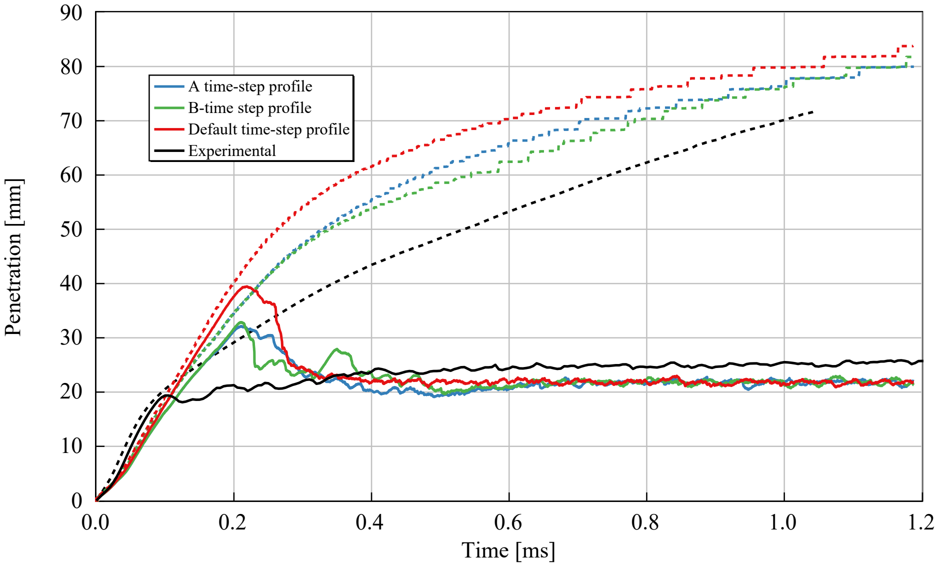

Figure 4.6: Time-step sensitivity: liquid (*continuous line*) and vapor (*dashed line*) penetration curves. Refer to tab. 4.3 for each time-step profile definition.

parameters and effects. Therefore, it is crucial to investigate the interplay between the grid size and the selected time-step. In this framework, fig. 4.7 compares the liquid penetration curve obtained with time-step profile A and the default grid dimension, i.e. $dx_{base} = 2\ mm$, with the one obtained using the same profile but a smaller and more finely resolved grid, i.e. $dx_{base} = 1\ mm$.

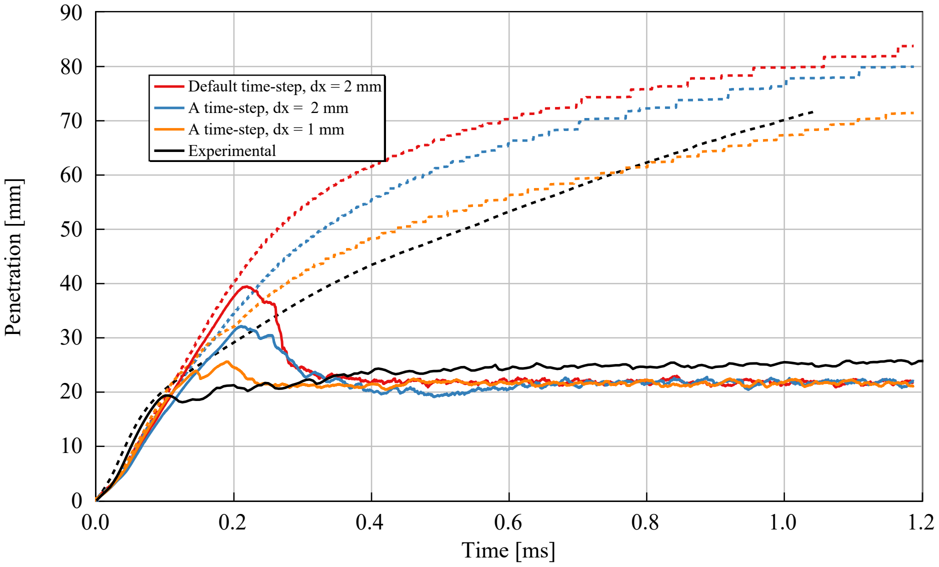

Figure 4.7: Liquid *(continuous line)* and vapor *(dashed line)* penetration curves with different time-step as well as base grid dimension.

The liquid curve generated with the smallest grid dimension, combined with the A time-step profile, resulted in the complete elimination of the peak. Although this approach is not practical due to the high computational power requirements and the consequent extended simulation duration, it provides evidence that the peak is not a physical phenomenon but rather a consequence of model-related issues. This is evident as the peak disappears when the grid is refined and the time-step is reduced.

Regarding vapor penetration, it can be observed in fig. 4.7 that the curve obtained with the smallest grid size exhibits a closer alignment with the experimental data. However, this alignment is not as evident in the other curves, potentially due to a more pronounced peak, resulting in higher jet tip penetration during this phase.

Summarizing the results of this sensitivity analysis, it has been shown that the maximum time-step used to compute the numerical solution significantly affects the damping of the transient liquid penetration peak. Moreover, it has been observed that this peak is not physical but rather related to model issues. Consequently, starting from this step, the A time-step profile from tab. 4.3 has been employed. In the subsequent sections, the analysis will shift its focus towards other parameters and their impact on both the steady-state liquid length and the transient peak. Additionally, efforts will be made to improve the alignment of the vapor data with the experimental results.

4.2.3 Sensitivity to shed mass constant

The shed factor variable was introduced in sec. 3.1.1 to represent the *percentage of mass that undergoes primary breakup*. It has a significant impact on the entire breakup process, as it affects the tracking of the fragmented mass as described in eq. (3.13). In this sensitivity analysis, the shed mass constant was varied, considering three different values: 0.1, 0.4, and the initial value of 1. Furthermore, despite the findings of the previous section about time-step, here the sensitivity has been performed with the default time-step profile of tab. 4.3, in order to reduce the computational power requested for this sensitivity, as well as to investigate the shed factor effect only. The results of this sensitivity are shown in fig. 4.8.

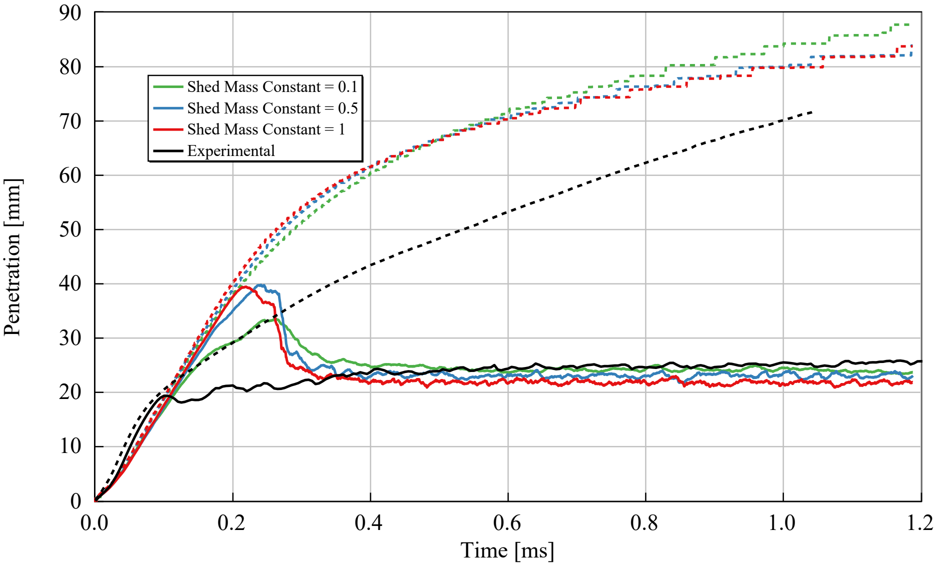

Figure 4.8: Liquid *(continuous line)* and vapor*(dashed line)* penetration curves for different values of the shed mass constant.

The initial observation reveals that the curve characterized by the highest shed factor has the shortest steady-state liquid length. This finding can be attributed to the fact that the

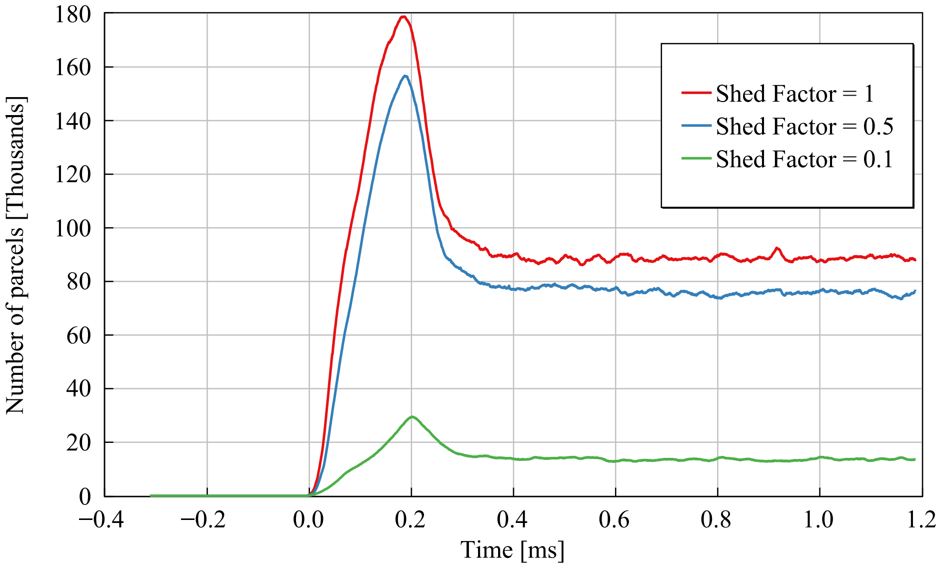

Figure 4.9: Number of parcels for different shed mass constant values.

highest shed factor results in a breakup process for all parcels in the computational domain. As a result, the number of parcels in the computational domain is significantly higher in the case where the shed factor is 1, as testified from fig. 4.9. Consequently, with fewer parcels undergoing primary breakup, the drop radius distribution differs notably as it is possible to see from fig. 4.10 at $t = 0.73\ ms$. Specifically, when the shed factor is set to 1, the drop radius reaches its minimum value in the near nozzle region. Conversely, when the shed factor is reduced to 0.1, the near nozzle region contains larger droplets. The variation in drop radius is of significant importance in the breakup process, as smaller-diameter droplets tend to evaporate more quickly compared to larger ones.

Regarding the transient phase, using a shed factor equal to 0.1 leads to a reduction in the peak, similar to what was observed with the A time-step profile previously analyzed. However, the vapor penetration results remain practically unaffected by changes in this parameter. As a conclusion of this sensitivity analysis, a shed factor of 0.1 is chosen even it will later be restored to its initial value of 1; indeed, it is important to note that using a shed factor of 0.1 significantly modifies the entire breakup process, as evidenced by the previously discussed plots. This decision is made to investigate the interaction of this factor with other effects, as described in the next section.

4.2.4 Sensitivity to turbulent initial conditions

In this sensitivity analysis, the goal is to gather information about the influence of turbulent initial conditions, specifically related to turbulent kinetic energy (TKE) and initial turbulent dissipation (ϵ). In the initial setup, these values are set to $TKE = 1\ m^2/s^2$ and $\epsilon = 100\ m^2/s^3$. However, these values were determined based on considerations related to

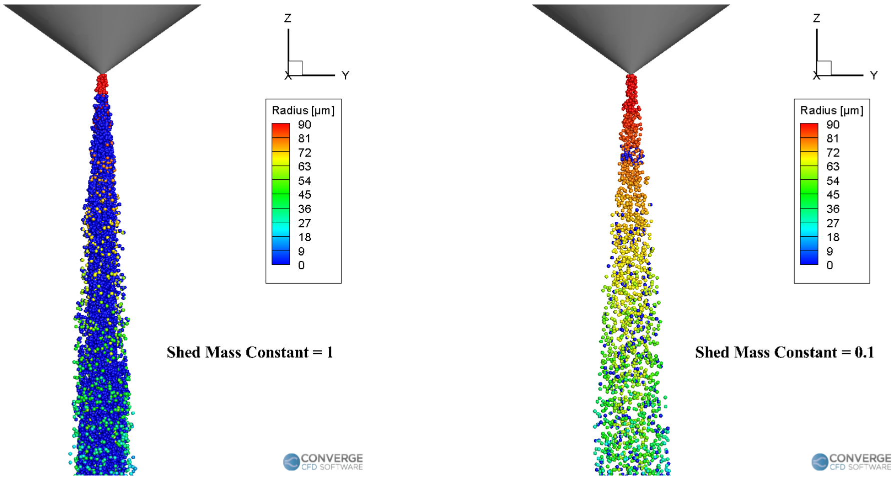

Figure 4.10: Drop radius distribution in the near nozzle region at $t = 0.73$ ms for two different shed factors.

the quasi-steady condition present in the chamber at the injection timing, similarly to the conditions experienced in Spray A case, as suggested by CONVERGE; since there are no experimental data available for validation, there is a possibility of error in their initialization. Consequently, a sweep has been performed, simultaneously changing both the turbulent kinetic energy and the turbulent dissipation initial values. In this case the sensitivity has been performed with the shed mass constant equal to 0.1, as outlined in the previous section. Results of this sensitivity in terms of liquid and vapor penetration are displayed in fig. 4.11.

An important outcome of this sensitivity analysis is the high sensitivity to turbulent initial conditions. In the case of the most turbulent condition, i.e., $TKE = 10$ m^2/s^2 and $\epsilon = 200$ m^2/s^3, the total damping of the peak has been achieved. However, it's important to note that this result is not to be interpreted as a strict condition. Rather, the information to be extrapolated here is the influence of turbulent initial conditions on the initial damping. Regarding the specific values of initialization, a further analysis will be conducted later. In this step, the turbulent initial conditions are kept at their initial values, i.e., $TKE = 1$ m^2/s^2 and $\epsilon = 100$ m^2/s^3. Additionally, as previously mentioned, the shed factor is reset to the standard suggested value of 1.

4.2.5 Sensitivity to KH time constant and near cone angle

In this section, the objective is to identify the optimal combination of the Kelvin-Helmholtz model time constant B_1 and the near cone angle ϑ for our model to achieve the best agreement with the experimental data. These two variables are known to have the most significant influence on liquid penetration, thus this step represents a very important point in the whole calibration process for the spray model.

This sensitivity process will be carried out through several steps:

1. Creation of a Design of Experiment Matrix (DOE);
2. Analysis of the initial results from the parameter sweep and narrowing down the range of parameters;
3. Final selection of the optimal parameter combination;

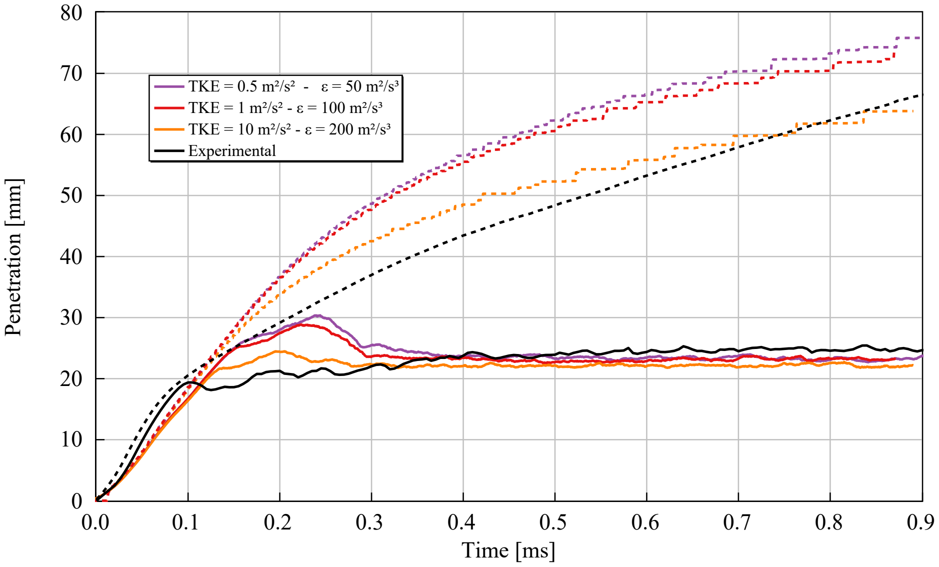

Figure 4.11: Sensitivity to Turbulent Kinetic Energy (TKE) and Turbulent Dissipation (ϵ) initial values.

In the first step, we have selected three values for the near cone angle, which fall within the range recommended by the Heywood model. Indeed, as discussed in 3.2, among the different models available for the computation of the near cone angle, we refer to the one presented in [32], here reported again in (4.2):

$$tan(\vartheta/2) = c_1 \left[\left(\frac{\rho_a}{\rho_f} \right)^{0.19} - c_2 \left(\frac{\rho_f}{\rho_a} \right)^{0.5} \right] \tag{4.2}$$

where c_1 is a constant which depends on the nozzle geometry and can vary from 0.26 and 0.4, while c_2 is equal to 0.0043 for vaporizing spray or to 0 in the case of non-vaporizing spray. In this phase we set the c_1 variable to 0.*26*, *0.4* and to an intermediate value of *0.33*; the correspondent near cone angle values are *12.8°*, *21°*, and *14°*.

For the Kelvin-Helmholtz model time constant, there is a broader range to explore, with CONVERGE suggesting values between 5 and 100. As an initial attempt, we have chosen three values within the range of 5 to 40. These values are 7, 20, and 40.

Since this sensitivity analysis involves two distinct parameters, it is essential to consider not just single values but also investigate their coupling. To achieve this, a 2D Design of Experiments (DOE) matrix has been created, allowing for the exploration of all possible combinations of these two parameters. In this step only two parameters have been chosen in order to reduce the number of simulation to be performed; indeed, being the effect of each parameter not perfectly known and, at the same time, also the effect of the interaction among this parameters, the number of simulations will increase exponentially with the number of variables included in the DOE matrix. In fig. 4.12 the 2D DOE matrix is reported.

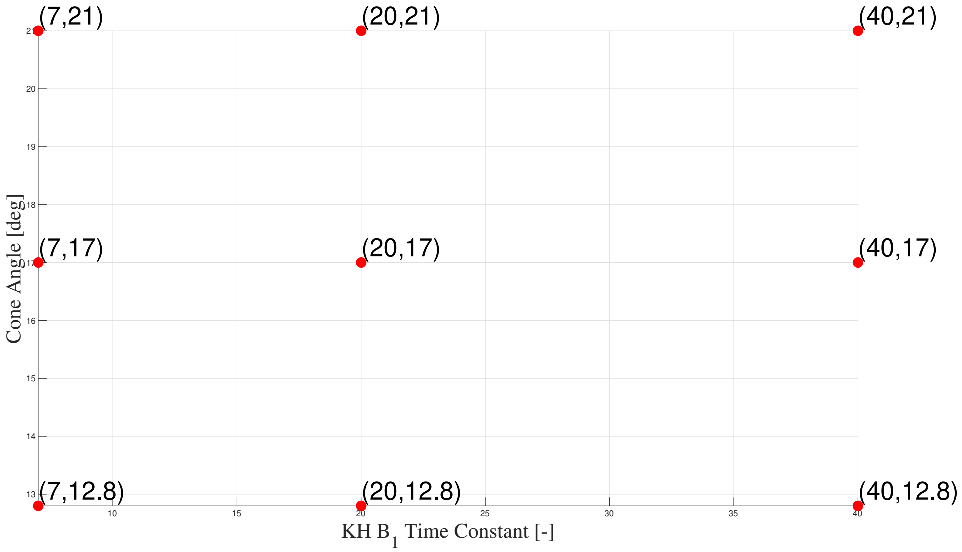

Figure 4.12: 2D DOE matrices.

Fig. 4.13 displays the results of liquid and vapor penetration based on the 2D simulation matrix presented in fig. 4.12. These results are examined while varying the near cone angle, keeping the Kelvin-Helmholtz (KH) time constant constant.

Looking at the behavior of the steady-state liquid length, we observe an interesting pattern. For cases where $B_1 = 20$ and $B_1 = 40$, an increase in the cone angle leads to a longer liquid length. In contrast, a decrease in the liquid length is noted when $B_1 = 7$. This behavior can be explained by considering how these two parameters influence the breakup process. When the KH time constant is set to 7, breakup occurs prematurely, reducing the impact of higher drop velocity resulting from the smaller outlet diameter created by the cone angle. On the other hand, when higher breakup time constants (20 and 40) are used, there is ample time for droplets to take advantage of their higher speed, achieved due to the smaller near cone angle, allowing them to penetrate deeper into the chamber.

Fig. 4.14 depicts the reverse scenario, where a near cone angle sweep is conducted while keeping the Kelvin-Helmholtz (KH) time constant fixed. An interesting observation is that, for a near cone angle of 17°, the vapor penetration appears to remain largely unaffected by variations in the time constant values.

These initial findings highlight the impracticality of using high B_1 values, as indicated by the inconsistent results obtained for $B_1 = 40$ compared to experimental data. Furthermore, for all tested values of the near cone angle ϑ, the experimental steady-state liquid length consistently falls within the range defined by the curves obtained for $B_1 = 7$ and $B_1 = 20$. Another significant outcome of this analysis is the improved alignment between experimental and numerical results, particularly with regard to the liquid penetration peak during the transient phase. This alignment was achieved solely by adjusting the values of the near cone angle ϑ and the KH time constant. Consequently, the calibration effort will primarily concentrate on fine-tuning these parameters.

In this framework, following the three aforementioned steps, it is possible to narrow the operating range for the KH time constant while maintaining the range for the near cone angle unchanged. The revised Design of Experiment (DOE) matrix is presented on the left in fig. 4.15, which now includes a sweep of near cone angle values for $B_1 = 14$.

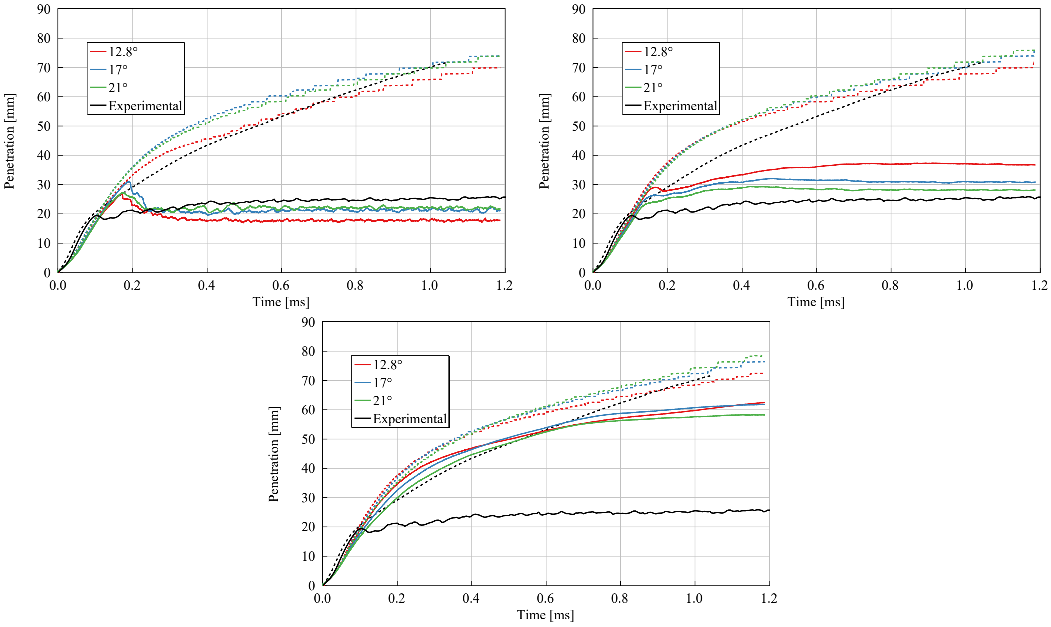

Figure 4.13: Liquid (*continuous line*) and Vapor (*dashed line*) penetration curves for 2D Design of Experiment (DOE) simulations. On the top-left, a near cone angle sweep with $B_1 = 7$. On the top-right, a near cone angle sweep with $B_1 = 20$. On the bottom, a near cone angle sweep with $B_1 = 40$.

The angle sweep results for this configuration are illustrated on the right in fig. 4.15. In this setup, a notable observation is the quasi-independence of the steady-state liquid length concerning the near cone angle. Simultaneously, the rising trend of the liquid penetration curves appears to be better approximated for lower near cone angle values, which, conversely, yield the highest peak during the transient phase.

The results obtained thus far, coming from parameter sweeps shown on the left in fig. 4.15, need to be analyzed to identify the common trend in liquid penetration for both near cone angle ϑ and KH time constant B_1. In this analysis, we solely focus on liquid penetration as it is closely related to vapor penetration. To create a contour map, we reference the mean liquid penetration for each parameter combination within a time window spanning from $t = 0.4$ ms to $t = 1.2$ ms. This time frame is chosen because the liquid length is well-defined for each simulation during this period. On the contrary, it is worth noting that the transient phase, as observed in fig. 4.13, 4.14, and 4.15, does not exhibit a clear trend and is not accurately captured by the models. Consequently, in this phase, we do not rely on this part of the simulation for our analysis.

The contour map, as shown in fig. 4.16, reveals several important insights. Firstly, there is an independent behavior of steady-state liquid length concerning the near cone angle within a broad range of KH time constants. Specifically, between $B_1 = 12$ and $B_1 = 15$, the liquid length remains unaffected by changes in the near cone angle. Additionally, between $B_1 = 15$ and $B_1 = 17$, any variations in liquid length with alterations in the near cone angle are minimal. In contrast, in regions with lower KH time constant values ($B_1 < 12$) and higher KH time constant values ($B_1 > 17$), variations in liquid length are more pronounced.

In the context of the experimental liquid penetration data, the mean value to consider within the range defined by the color map is $L_{exp,ss} = 23.5$ mm. However, it is important to note that the color map was constructed based on just nine test points, which may

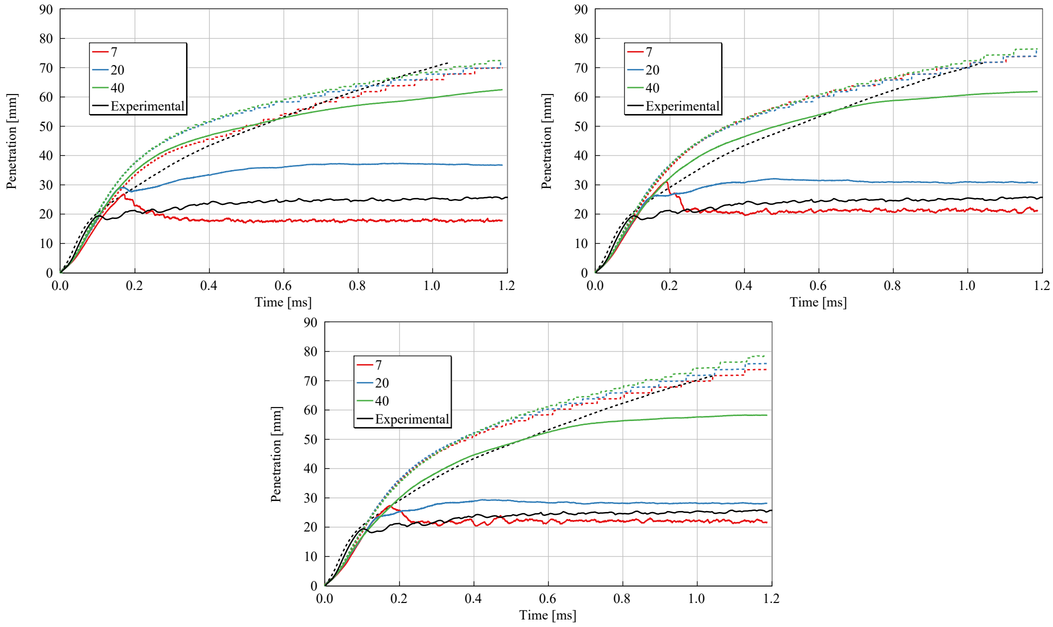

Figure 4.14: Liquid (*continuous line*) and Vapor (*dashed line*) penetration curves for 2D Design of Experiment (DOE) simulations. On the top-left, a B_1 values sweep with $\vartheta = 12.8°$. On the top-right, a B_1 values sweep sweep with $\vartheta = 17°$. On the bottom, a B_1 values sweep sweep with $\vartheta = 21°$.

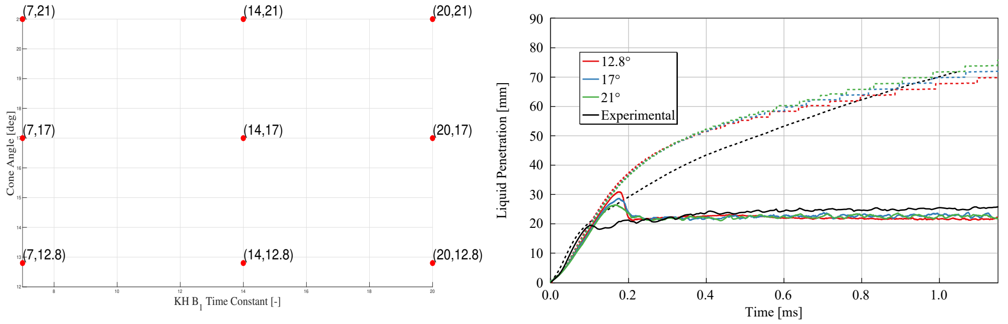

Figure 4.15: On the left the new 2D DOE matrix including an angle sweep for $B_1 = 14$. On the right liquid (*continuous line*) and vapor (*dashed line*) penetration curves obtained with different near cone angle values for $B_1 = 14$.

be insufficient for a comprehensive understanding of the entire interaction between these two parameters. Therefore, within this region, we not only consider the light-green region but also include the dark-green region, expanding the acceptable range from a mean liquid penetration length of 23.09 mm to 25.56 mm.

Examining the parameters delineated within the contour map and considering the acceptable parameter range we have determined, it becomes apparent that there are effectively no constraints on the near cone angle. In contrast, stringent limitations apply to the time constant B_1, which must reside within the narrow band of 15 to 17. Our initial investigations were centered around two extreme scenarios: one featuring $B_1 = 15$ coupled with a near cone angle of $\vartheta = 17°$, and the other involving $B_1 = 17$ in conjunction with a near cone

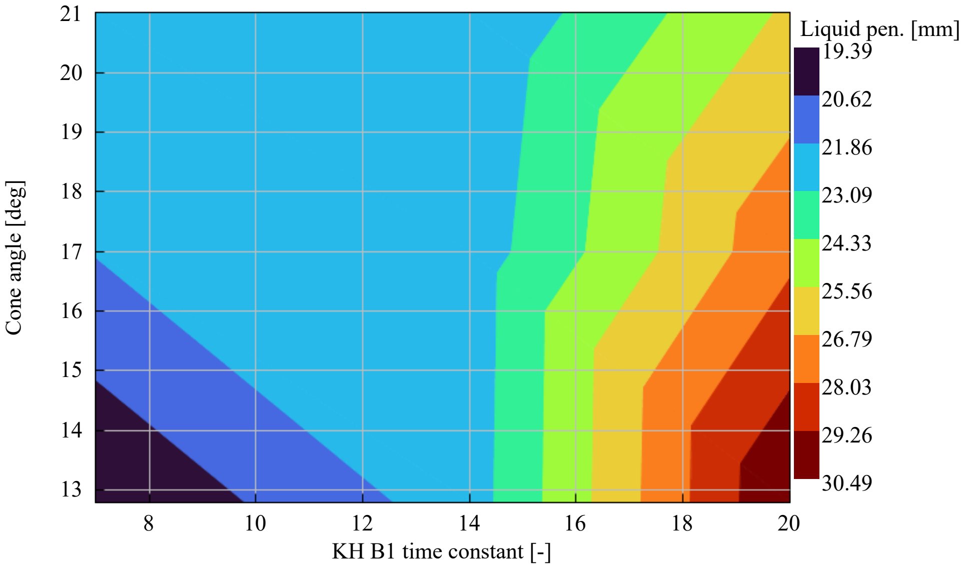

Figure 4.16: Steady-state liquid length contour map.

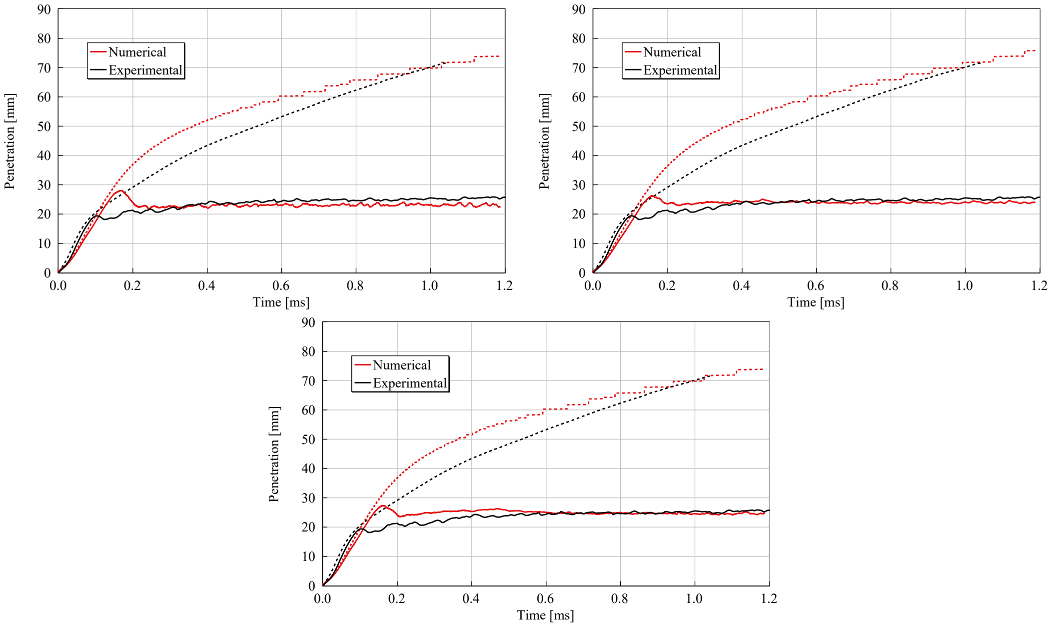

Figure 4.17: Liquid (*continuous line*) and Vapor (*dashed line*) penetration curves for three different test conditions. On top-left: $B_1 = 15$, $\vartheta = 17°$. On top-right: $B_1 = 17$, $\vartheta = 20°$. On the bottom: $B_1 = 17$, $\vartheta = 17°$.

angle of $\vartheta = 20°$. The results are displayed on the top of fig. 4.17. Looking at the region of interest, i.e. $0.4 < t < 1.2\ ms$, the simulation with $B_1 = 17$ seems to approximate better the steady-state liquid behaviour. Furthermore, in consideration of the preceding discoveries and the slight impact of the cone angle on liquid length for $B_1 > 15$, an additional simulation was conducted with $\vartheta = 17°$, as illustrated at the bottom of the same figure. In this scenario, the numerical steady-state liquid length aligns precisely with the experimental data, thus concluding this phase of model development.

4.2.6 Refining activity on the model

The objective of this section is to make the liquid and vapor penetration more consistent with the experimental data. The numerical model developed so far, as shown at the bottom in fig. 4.17, already demonstrates good alignment with experimental results. However, further refinements are required to enhance the match of vapor penetration and improve the model's reliability during the transient phase of liquid penetration. These refinements will be based on the insights gained from previous investigations, particularly regarding turbulent initial conditions.

The previous findings concerning turbulent initial conditions have revealed the effect of reducing the transient peak when the highest values of turbulent initial conditions are employed. In light of this, a new sweep for the initialization of turbulent kinetic energy has been conducted. In this case, three different values have been tested: $TKE = 1\ m^2/s^2$, $TKE = 3\ m^2/s^2$, and $TKE = 10\ m^2/s^2$. The choice to manipulate turbulent initial conditions is based on the observation that a different initialization of the model led to a reduction in the peak without significantly altering the steady-state behavior in liquid penetration. It is important to note that the proposed values may deviate from the actual initial conditions during experiments, not reflecting the quiescent environmental conditions. Nonetheless, for this work, the assumption of virtually increasing the turbulent kinetic energy to enhance the model's reliability during the transient phase of liquid penetration is accepted. This decision is also influenced by the time-evolution of the turbulent kinetic energy, which is only slightly affected by this modification, as shown in fig. 4.18 where the mean TKE value in the spray region as a function of time is plotted. An important observation from this plot is that an increase in the initial turbulent kinetic energy leads to a faster variation of the same in the initial phase of the injection, as testified by the different slope during the transient rising phase in the same figure. In this sense, it is assumed that higher initial turbulent kinetic energy results in a quicker creation of turbulence in the first stage, thus enhancing liquid evaporation, without significantly affecting the steady-state value where convergence at the same mean value can be appreciated. Moreover, it is worth noting that the initial TKE values tested, i.e., $TKE = 3\ m^2/s^2$ and $TKE = 10\ m^2/s^2$, are significantly lower than the maximum local value reached in the spray during injection. The results of the sensitivity to TKE initial values are plotted in fig. 4.19.

Furthermore, in this step, the difference in terms of liquid and vapor penetration when using a smaller grid has been analyzed. Figure 4.20 presents the results of this comparison. An important observation emerges from this analysis: while in the first step of the calibration process, the grid sensitivity study, the curve associated with the smallest dx_{base} exhibited better behavior in describing the transient phenomenon and capturing vapor penetration, here the differences are practically negligible. The only noticeable difference is in the rise of the liquid penetration, which is still somewhat sensitive to the grid size employed. However, the distinctions in the maximum transient peak and vapor penetration curves are no longer present. In light of these results, despite the good achievement in prediction of the liquid and vapor penetration, the effect of different initial conditions needs more analysis, for future development of the model.

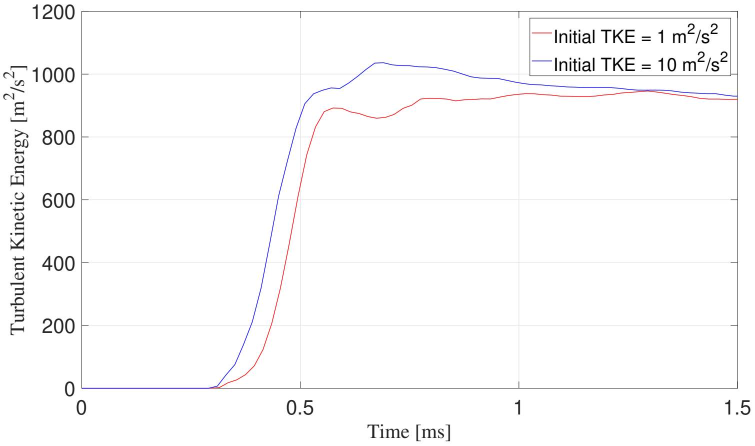

Figure 4.18: Time-evolution of the mean turbulent kinetic energy (TKE) in the spray region.

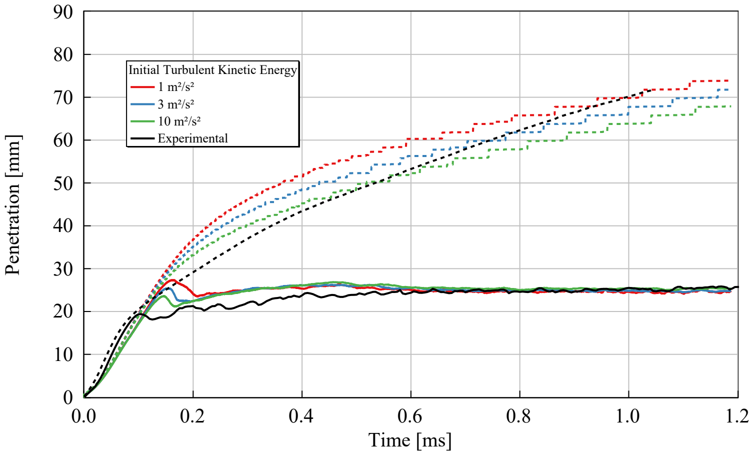

Figure 4.19: Sensitivity to turbulent initial conditions.

In summary, the calibration process involved various sensitivity analyses. It began with an investigation into the dependence of the solution on grid dimensions, ensuring grid size convergence with a base grid size of 2 mm. Then, an exploration of the maximum time-step (dt_{max}) for use up to achieving steady-state liquid penetration was conducted, employing a variable time-step ranging from $5e{-}08$ s to $1e{-}07$ s for this phase. Following this, sensitivity analyses were performed to understand the influence of the shed factor and turbulent initial conditions on liquid penetration. Subsequently, a calibration activity using a Design of Experiments (DOE) approach focused on the near cone angle (ϑ) and the Kelvin-Helmholtz time constant (B_1) was performed. The final choices were $\vartheta = 17°$ and $B_1 = 17$. In the final refinement step, turbulent initial conditions were adjusted to a turbulent kinetic energy of $TKE = 10\ m^2/s^2$ and turbulent dissipation of $\epsilon = 100\ m^2/s^3$.

In fig. 4.21, it is possible to see the numerical liquid and vapor penetration profiles from the calibrated model, as well as the experimental mean curves and the standard deviation associated curves. The model appears to be quite reliable in predicting liquid penetration, especially in the steady-state curve. However, the prediction for vapor penetration, while not perfect, is acceptable as it remains close to the experimental curve and falls within the

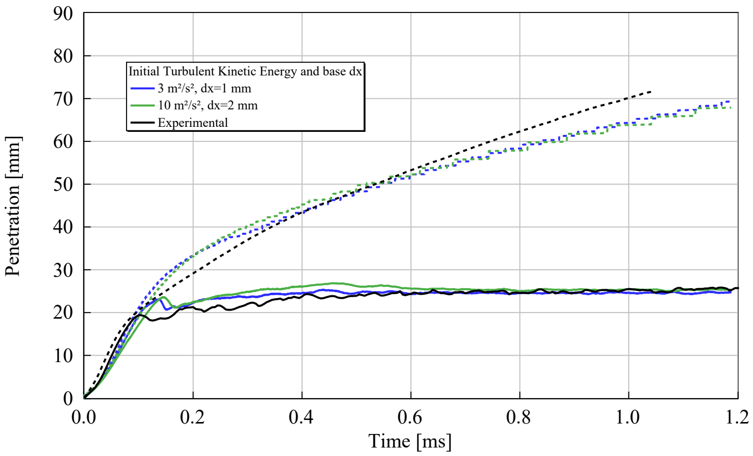

Figure 4.20: Sensitivity to turbulent initial conditions and base *dx*.

range defined by the vapor penetration, except for a time interval between $t = 0.14\ ms$ and $t = 0.38\ ms$. In light of these findings, future development of the model should prioritize improving the prediction of vapor penetration, aiming for a closer match with experimental data. This enhancement will contribute to a more comprehensive and accurate representation of the spray dynamics.

In fig. 4.22, a qualitative comparison is presented between experimental and numerical images. This comparison serves as a means to validate the spray shape for both the liquid and vapor phases. At 100 µs after the start of injection (aSOI), the liquid phase in the numerical simulation closely resembles that in the experimental images. However, as the injection proceeds, this alignment becomes less apparent. At 400 µs and 500 µs aSOI, the liquid phase in the experimental images appears to have a wider near-cone angle, resulting in a larger shape for the entire liquid length. Conversely, the vapor penetration in the experimental images seems slightly smaller than what is observed in the numerical images. It is important to note that this is a qualitative comparison, and a detailed quantitative assessment is not feasible. Furthermore, it is worth noting that distinguishing between the vapor and liquid phases in these images can be challenging and errors can be present due to a not-optimized procedure. Consequently, small variations in the spray shape can result from different settings used to identify these phases.

Finally, despite these minor qualitative differences, the spray model can be considered calibrated and validated also in function of the results obtained in literature were similar behavior especially in transient conditions have been obtained also employing more complex and accurate turbulence models, as in [34].

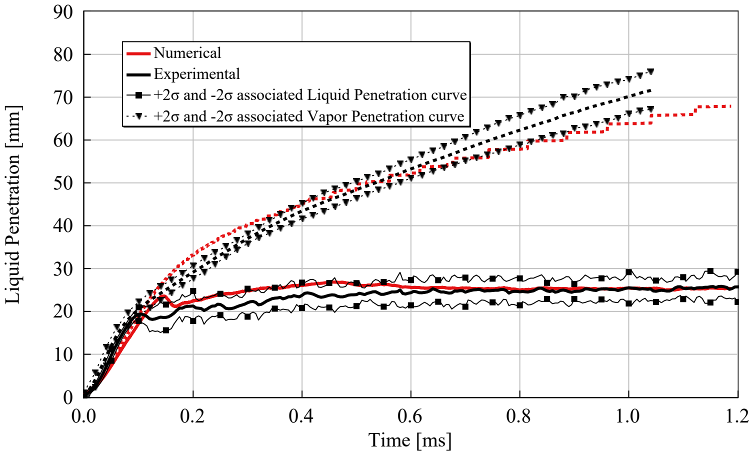

Figure 4.21: Experimental liquid and vapor curves along with their respective standard deviation curves, as well as the numerical results obtained from the calibrated model.

4.2.7 Fully-predictive DFI results

In this section, the DFI (Ducted Fuel Injection) is integrated into the developed ECN Spray D model. This results in a fully-predictive model, as there are no available experimental data for the DFI case under these test conditions. Consequently, the validation of the DFI ECN Spray D model relies on prior findings and knowledge, particularly from the PoliTO-UniPG experimental and numerical data.

First, the model was adapted to accommodate DFI. To achieve this, the CVV now includes a duct, represented as a small cylinder with dimensions of *2 mm* in diameter and *14 mm* in length, positioned *2 mm* below the nozzle outlet (D2L2G14). The inclusion of the duct introduced new initialization parameters, such as the temperature on the duct walls. In this case, no temperature gradient was considered, and the duct walls were set to the same temperature as the vessel.

In terms of grid size, both fixed embedding and AMR (Adaptive Mesh Refinement) techniques were maintained. The implementation of AMR remained similar to before, with the exception that it now needed to consider the presence of the *inlaid mesh*. As for fixed embedding, two new embedded regions were introduced. The first was defined within the duct region, while the second was a reverse truncated cone. The objective here was to encompass, within a smaller grid size area, all the flow in the region adjacent to the duct inlet. In table 4.4 the embedded region geometries are reported; in fig. 4.24, the grid structure is displayed. For clarity, it is important to note that in both the free-spray computational domain and here, the smaller cone with the smaller grid size is not visible, as it is incorporated within the bigger cone.

Finally, to achieve a rate shape comparable in terms of DOI with the PoliTO-UniPG spray data, a modified ROI was used compared to the experimental data. It is essential to note that this modification does not affect the results obtained thus far, as this new rate shape was created using the same simplified tool employed for the creation of the split profiles explained in sec. 3.3, thus ensuring the reliability of the profile obtained. The

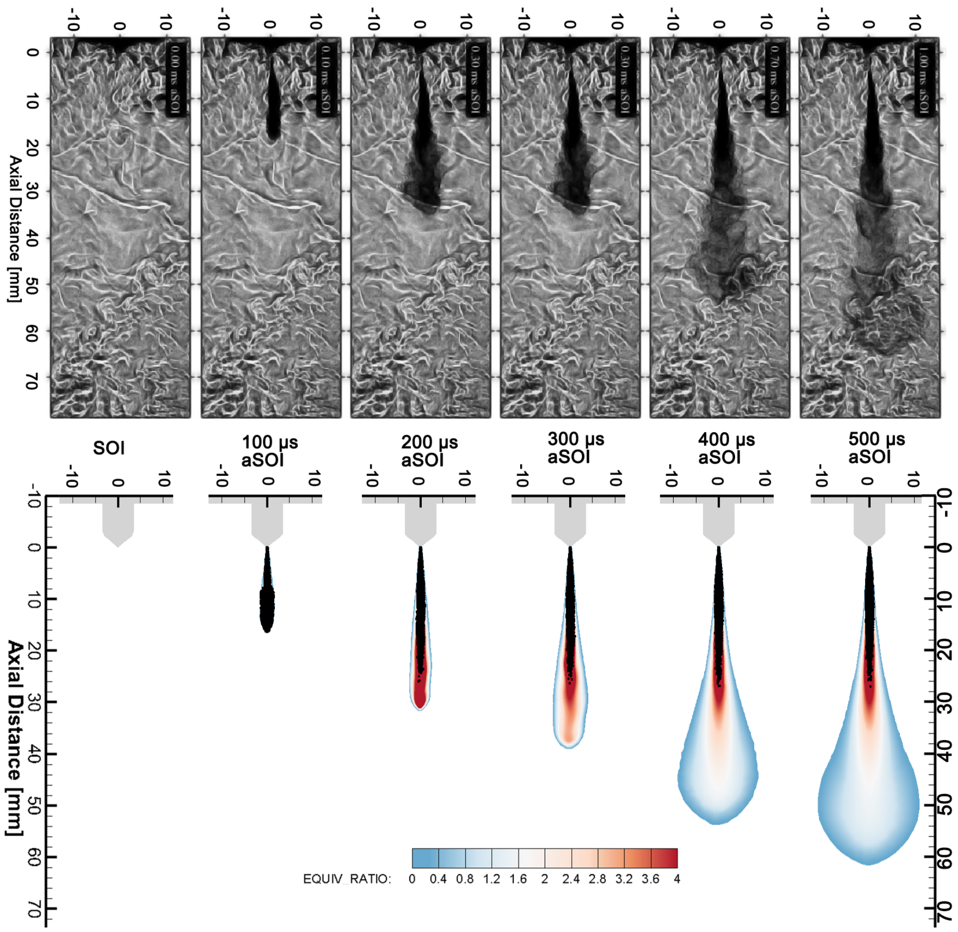

Figure 4.22: Experimental vs. Numerical Spray Evolution. The vapor phase is contoured by equivalence ratio values. The liquid phase is represented in black.

new profile is shorter, resulting in less mass being injected. The new rate shape profile is displayed in Figure 4.23.

	Scale factor	Length [mm]	Top base radius [mm]	Bottom base radius [mm]
Bigger Truncated Cone	2	35	2	9
Smaller Truncated Cone	3	7	1	2
Duct Region	3	14	1	1
Reverse Truncated Cone	2	11.5	8	15

Table 4.4: Fixed Embedding Geometries Dimensions for ECN Spray D model in DFI condition.

Once the adaptation of the model for the DFI case was performed, a simulation is run. First the computed liquid and vapor penetration is compared to the free-spray curves, as in fig. 4.25. From this, it is possible to denote an higher liquid-length for the DFI case. This finding is in line with the one obtained in [5]. Consequently also the vapor penetration is higher up from 0.2 ms aSOI, sign of an higher jet penetration.

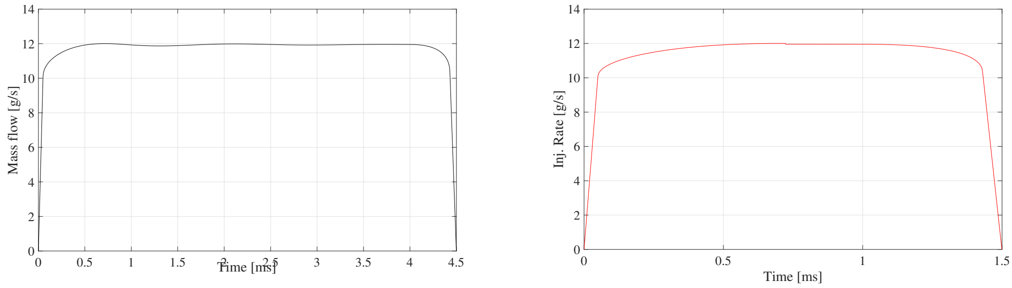

Figure 4.23: Experimental rate of injection (*left*) and shorted Rate of Injection (*right*) used for ECN Spray D simulations.

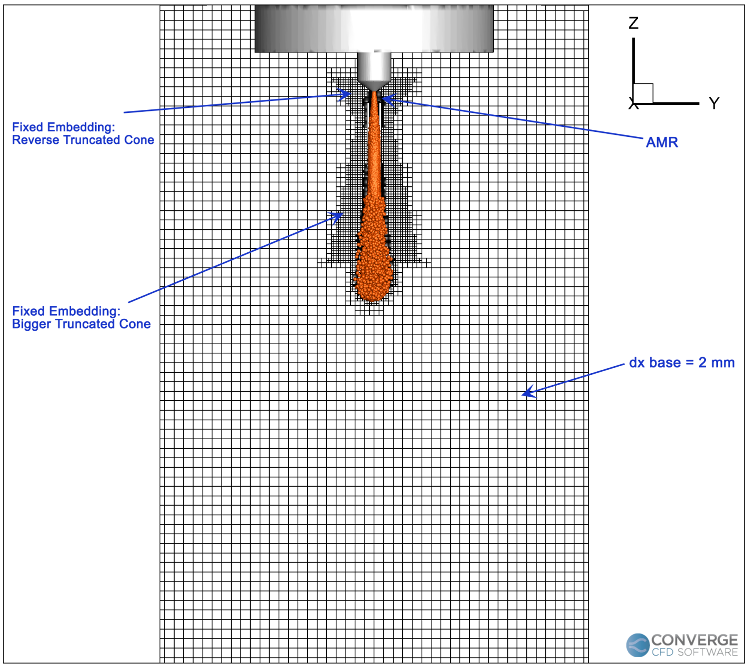

Figure 4.24: Grid structure in the computational domain for ECN Spray D in DFI condition.

Figure 4.26 illustrates the air flow rate in the spray computed within the duct inlet region and the cumulative entrainment[3]. These results are consistent with previous knowledge, as DFI has been recognized to enable higher air entrainment into the liquid spray [5]. In the tested case, DFI achieves nearly two times the air entrainment compared to the free spray. Furthermore, the phenomenon is related to the pressure distribution inside the duct, reported on the bottom in fig. 4.26. Coherently with [5], also in this case it is possible to identify the under-pressure field created by the high-velocity spray. Consequently, the higher air entrained in the spray is consistent with the duct-region pressure field.

Finally, an analysis of the equivalence ratio distribution was conducted. Figure 4.27 presents the results. In this aspect, a misalignment with previous findings is evident; indeed, despite the higher air entrainment, DFI appears unable to reduce the equivalence ratio. Consequently, rich pockets are present for all injection duration. Several phenomena could be

---

[3] For details about the methodology used for the entrainment computation refer to sec. 5.1.1

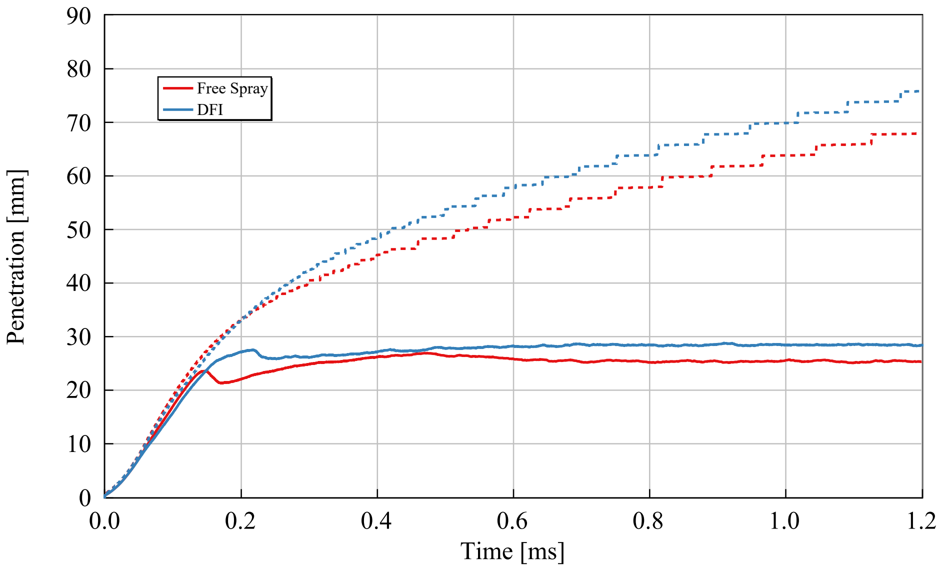

Figure 4.25: Validated Free Spray and fully-predictive DFI liquid (*continuous line*) and vapor (*dashed line*) penetration.

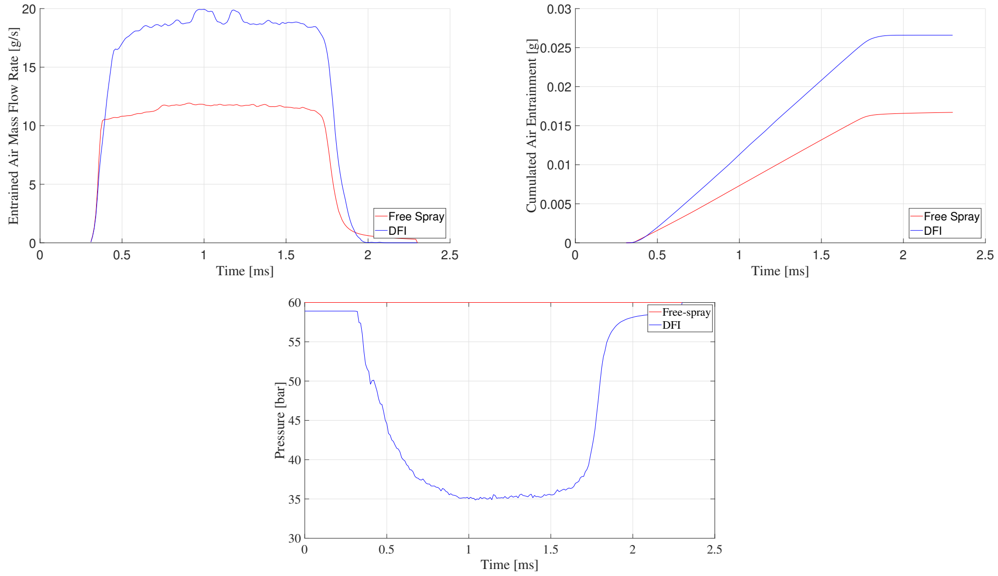

Figure 4.26: *Left*: Air entrainment for both Free Spray and DFI configurations. *Right*: Total entrained air for both Free Spray and DFI configurations. *Bottom*: Pressure time evolution in the duct region.

related to this behavior; first, different operating conditions compared to the PoliTO-UniPG spray could lead to a lower mixing efficiency of DFI in these conditions. Additionally, model-related issues could lead to a divergent behavior of DFI compared to previous knowledge: indeed, once again, this is a fully predictive model and has not been validated against corresponding experimental data.

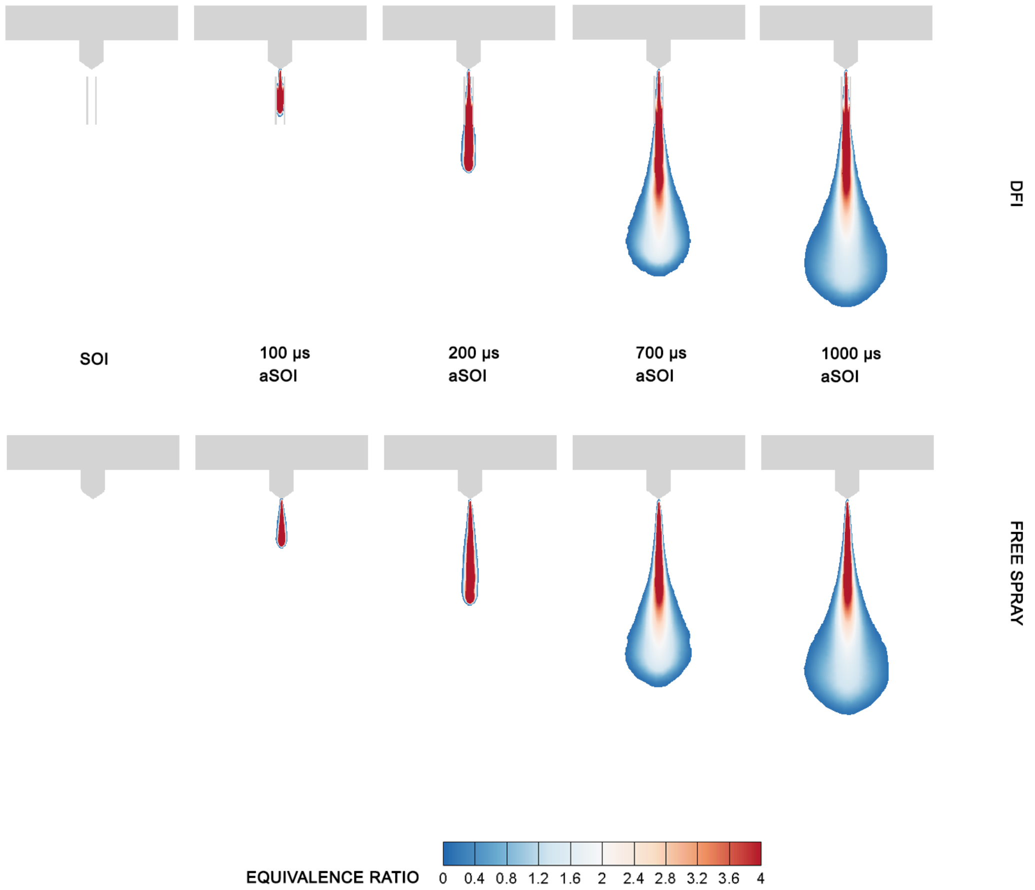

Figure 4.27: Equivalence Ratio evolution for both Free Spray and DFI cases obtained with ECN Spray D model.

Chapter 5

Effects of multi-injection on Ducted Fuel Injection operation in non-reacting conditions

In this chapter, a non-reactive analysis is conducted with a specific focus on evaluating the impact of secondary injection on various parameters. Initially, the PoliTO-UniPG spray model will be employed, followed by an extension of our analysis to incorporate the previously developed Spray D model. This approach facilitates an initial exploration of the influences of secondary injection on diverse parameters.

5.1 PoliTO-UniPG Spray: non-reacting analysis

The investigation will encompass different mass distribution ratios and various hydraulic dwell times. To provide a clearer overview of the conditions we are testing, they are summarized in tab. 5.1. Fig. 5.1 displays the injection rate profiles for each test condition, which have been generated using the developed tool as outlined in section 3.3.

The upcoming analyses will concentrate on evaluating whether the advantages identified from the introduction of DFI, as discussed in chapter 1, persist when utilizing split-injection profiles. Specifically, the first analysis will examine air entrainment, with particular emphasis on the pressure field inside the duct. Subsequently, the distribution of turbulent kinetic energy (TKE) for the second injection event will be analyzed to provide insights into how the flow field has been altered by the first injection. Finally, attention will be directed towards the equivalence ratio.

5.1.1 Air entrainment analysis

The analysis of air entrainment serves as an initial step in comprehending mixture formation. As established in [5], the adoption of DFI resulted in an augmented entrainment of air within the spray in the duct's inlet region. This phenomenon was found to be closely linked to the pressure field within the duct, and particularly to the under-pressure area and the subsequent development of a suction effect for air.

In this context, the computation of air entrainment was conducted from the nozzle outlet to the location where the spray impacts the duct walls. Initially, an overall-equivalence-ratio iso-surface was created to isolate the spray by setting a specific equivalence ratio threshold, in this case equal to 0.1. Subsequently, the axial distance at which the spray impinges on

Dwell Time Sweep		
Test N.	Mass Ratio [%]	Dwell Time [ms]
1		0.3
2	40-60	0.65
3		1
Mass Ratio Sweep		
Test N.	Mass Ratio [%]	Dwell Time [ms]
4	40-60	
5	20-80	1
6	5-95	

Table 5.1: Summary of the test conditions for non-reacting analysis on PoliTO-UniPG spray model.

the duct walls was computed using trigonometric relations based on the known values of the near spray cone angle ϑ and duct radius r_d. It is important to note that this computation assumed the spray to be perfectly symmetric with respect to the duct axis, enabling the calculation of the contact distance z_c as described in (5.1). On the left of fig. 5.2, it is illustrated the geometric approach used to compute the contact point; on the right of the same figure, the isolated iso-surface, in orange, is shown. After isolating the region of interest, the air mass flow rate was calculated. To achieve this, the integration tool of the commercially available software *TECPLOT 360* was utilized. The inputs for this calculation included temperature and pressure as state variables, the velocity components along the three directions for convective variables, and the air gas constant, which was set at $R_{air} = 287\ J/kg \cdot K$. Furthermore, in order to make the analysis consistent, this approach has been used also in the free-spray case, even if the duct is not present; in this way, the spray region in which the air entrainment has been computed is exactly the same for both two cases.

$$z_c = \frac{r_d}{tan\left(\frac{\vartheta}{2}\right)} \tag{5.1}$$

In this configuration, being $\vartheta = 18.5°$ and $r_c = 1\ mm$, the correspondent axial distance results $z_c = 6.14\ mm$.

Fig. 5.4, 5.5, 5.6, 5.7 and 5.8 report both the air mass flow rate within the spray and the cumulated air entrainment, computed as the integral of the first one.

For the tested conditions, air entrainment remains higher for DFI compared to that obtained in free-spray conditions, as indicated by the cumulative air entrainment. Moreover, when comparing the results obtained with split-injection profiles to those obtained with a single-injection profile - single injection results are displayed in fig. 5.3 -, a slight increase in total entrained air can be observed for the split-injection cases. This improvement may be attributed to the tail of the air flow rate curve, which not only reaches a steady-state more prominently for the DFI condition but also exhibits a slower transient phase returning to zero once the injection ceases. This slower transient phase allows more air to continue entering the spray in greater quantities compared to the free spray during this phase. Furthermore, since split-injection profiles feature two injection events, the final integral will take into account this tail twice, whereas in the single-injection profile, it is considered only once thus leading to slight higher air-entrainment in this case.

As previously mentioned in [5] and reiterated in this work, the increased air entrainment into the spray results from a low-pressure area created in the duct inlet zone, inducing a

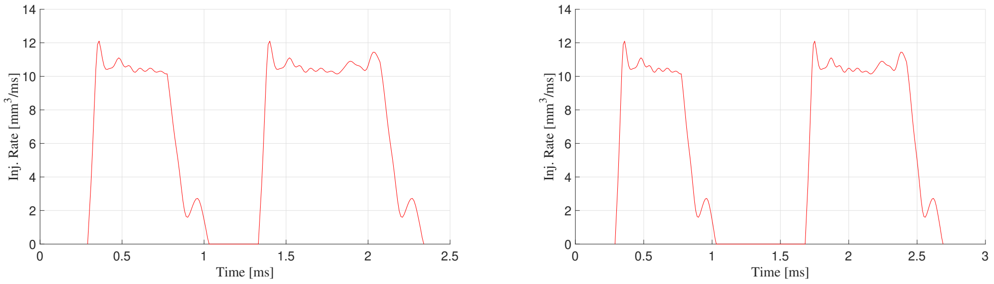

Test 1. Test 2.

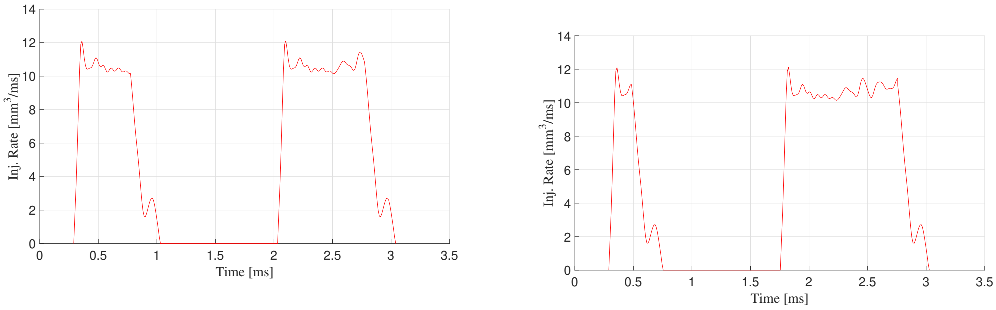

Test 3 and 4. Test 5.

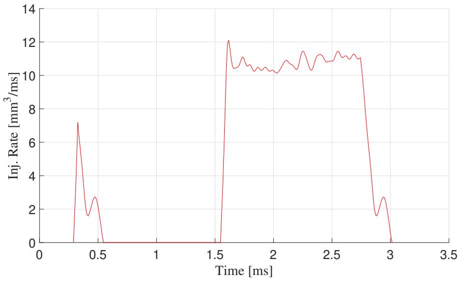

Test 6.

Figure 5.1: Rate Shape Profiles for the test conditions defined in tab. 5.1.

suction effect on the surrounding air. Consequently, the time required for the transient phase of the air flow rate is closely related to the time it takes for the pressure to return to its initial value, which was 20 bar for the tested conditions. In this context, the pressure evolution over time plays a crucial role. This relationship is clearly illustrated on the left in fig. 5.9, which highlights that the time needed for the pressure to return to its initial value is the same as the time needed for the air flow rate to reach zero again.

In fig. 5.10, the time evolution of the minimum pressure in the in-duct region is superimposed on the injection rate curve. This reveals the time delay between the achievement of steady-state for the injection rate and the attainment of steady-state minimum pressure, which in these conditions equals 0.1 ms. The transient duration for the pressure is also noticeable, lasting 0.15 ms. Therefore, it was of interest to investigate what happens if the minimum pressure steady-state value is not reached, simulating a kind of pilot injection that lasts less than 0.15-0.2 ms. The results, pertaining to test 6 and displayed in fig. 5.8,

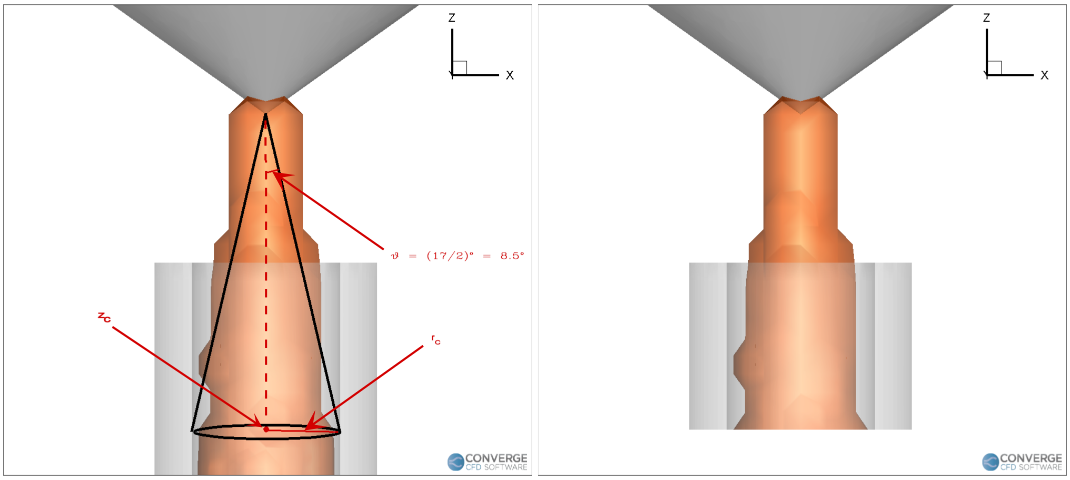

Figure 5.2: *Left*: Geometry scheme illustrating the computation of the axial distance z_c at which the spray impinges on the duct wall. *Rigth*: Isolated iso-surface from nozzle exit to z_c contact point.

show that in this case, the total entrained air is lower compared to that obtained with tests 3-4, but the DFI still allows to obtain higher amount of air in the spray if compared to the correspondent free-spray case. Thus, in light of the previous discussion, the slight lower amount of air can be related to the missed tail during first injection in the air flow rate and to an higher minimum pressure in the first injection, thus preventing the exploitation of the higher air flow rate.

Based on these results, it is crucial to emphasize that these findings align with previously established knowledge. However, they do not yield significant outcomes in terms of soot production. It is true that increased entrainment leads to greater mixing within the spray. Nevertheless, it is essential to consider that during the second injection, a portion of the fuel injected during the first injection has already burned. Consequently, the surrounding gases within the spray zone can also result from combustion, potentially leading to re-entrainment of hot gases in the region, finally shortening the lift-off length, as indicated in [3].

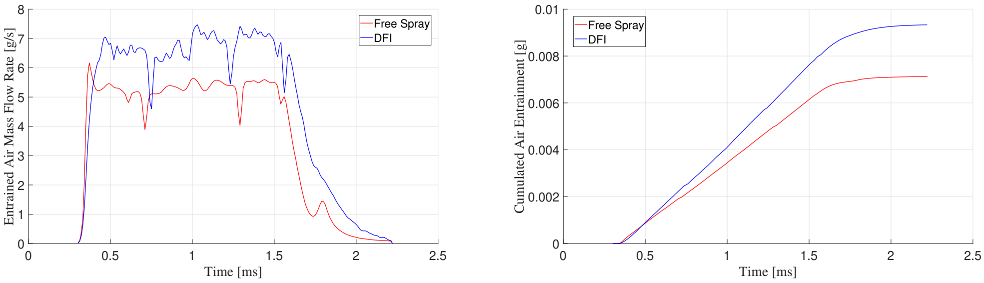

Figure 5.3: *Left*: Air entrainment for both Free Spray and DFI configurations with single-injection profile.
Right: Correspondent total entrained air for both Free Spray and DFI configurations.

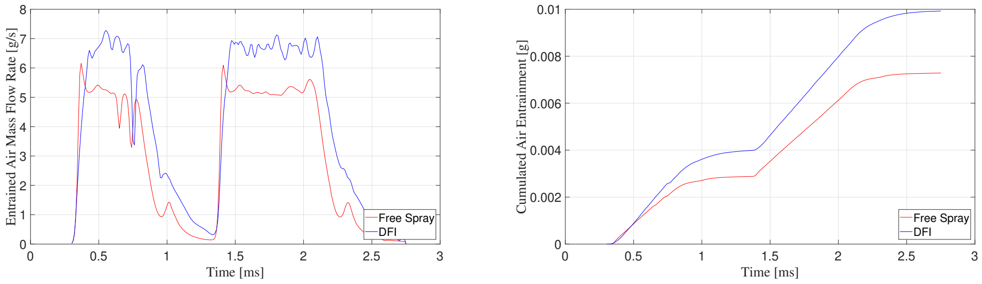

Figure 5.4: Test 1. *Left*: Air entrainment for both Free Spray and DFI configurations. *Right*: Correspondent total entrained air for both Free Spray and DFI configurations.

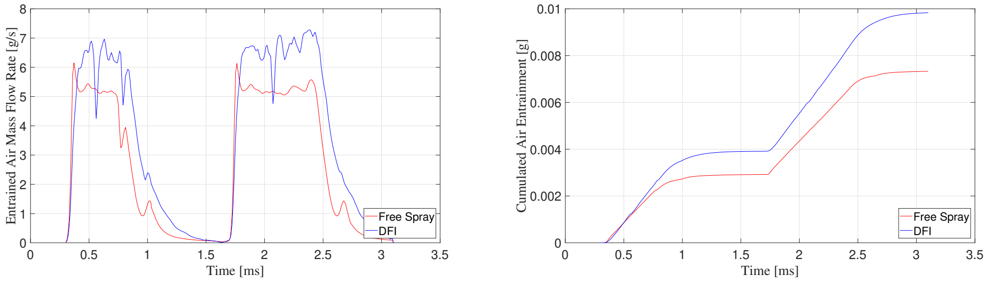

Figure 5.5: Test 2. *Left*: Air entrainment for both Free Spray and DFI configurations. *Right*: Correspondent total entrained air for both Free Spray and DFI configurations.

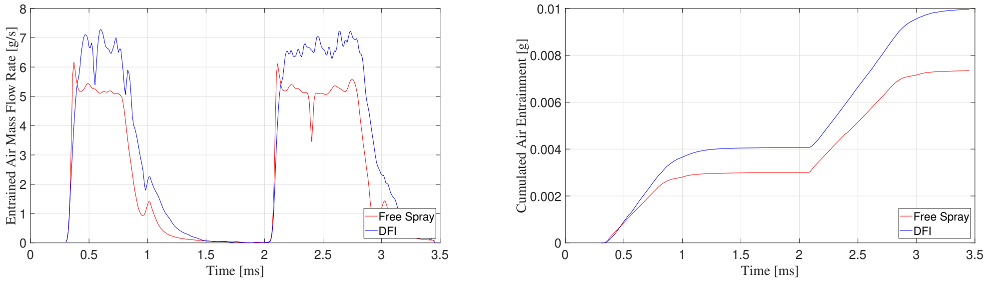

Figure 5.6: Test 3 and 4. *Left*: Air entrainment for both Free Spray and DFI configurations. *Right*: Correspondent total entrained air for both Free Spray and DFI configurations.

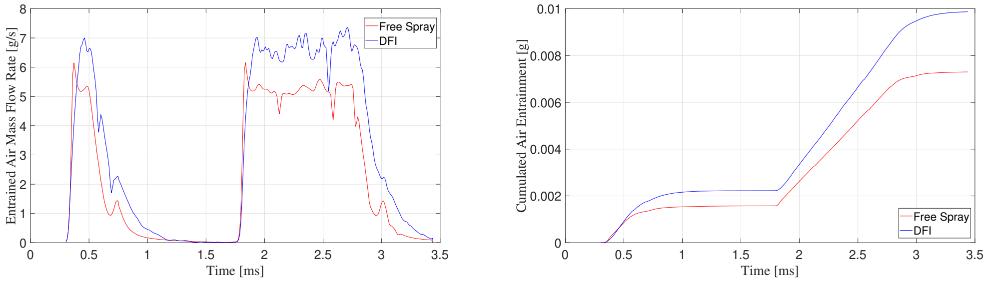

Figure 5.7: Test 5. *Left*: Air entrainment for both Free Spray and DFI configurations. *Right*: Correspondent total entrained air for both Free Spray and DFI configurations.

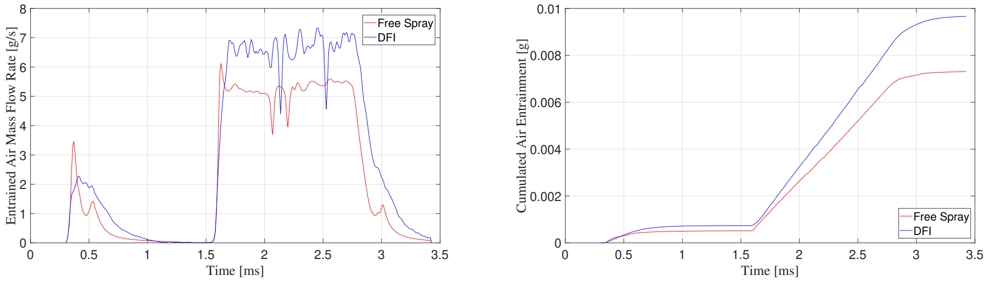

Figure 5.8: Test 6. *Left*: Air entrainment for both Free Spray and DFI configurations. *Right*: Correspondent total entrained air for both Free Spray and DFI configurations.

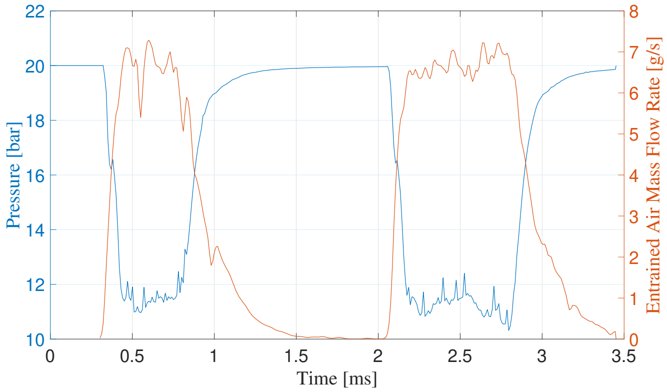

Figure 5.9: Minimum in-duct pressure vs. Duct inlet region Air Mass Flow Rate in to the spray, test conditions 3-4. The time needed for pressure to come back to the original value governs the transient phase for the entrained air mass flow rate.

5.1.2 Turbulent mixing

In this section, the investigation focuses on turbulent conditions within the vessel, with particular attention to flow modifications arising from the first injection event. Additionally, attention is also directed towards the velocity field in the duct during the second injection event.

Previously work [5] has emphasized the different distribution of turbulent kinetic energy

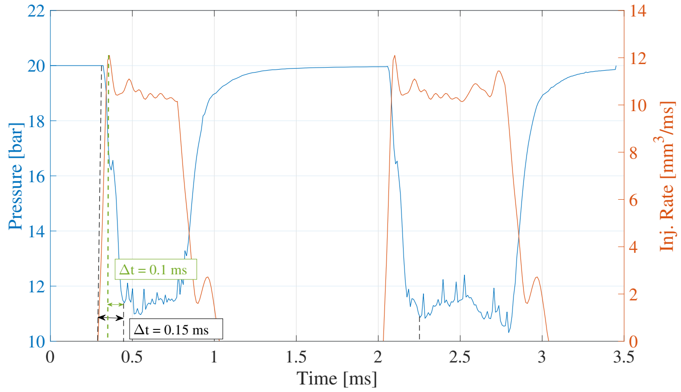

Figure 5.10: Minimum in-duct region pressure vs. Inj. Rate for test conditions 3-4.

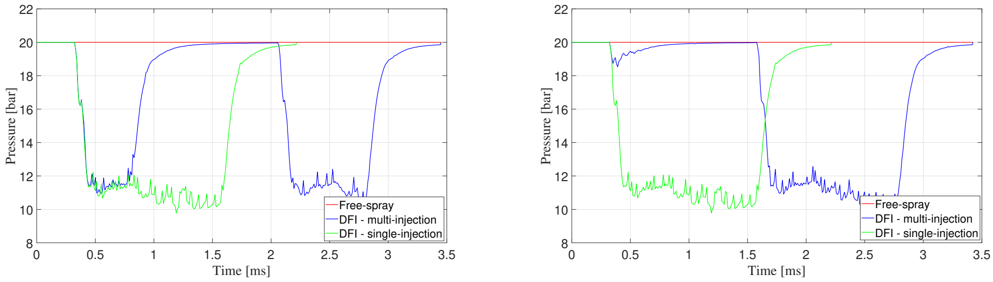

Figure 5.11: Pressure field in duct region. *Left*: Time Evolution of Minimum Duct Region Pressure with Test 3-4 conditions. *Right*: Time Evolution of Minimum Duct Region Pressure with Test 6 conditions.

between free-spray and DFI cases. The presence of the duct enhances the velocity gradient at the duct's outlet region. Consequently, for the DFI case, the distribution of turbulent kinetic energy illustrates the presence of high turbulent vortexes at the duct exit, as represented in [5, figure 15]. This phenomenon has been identified as a significant source of mixing for air and fuel, aligning with the hypotheses presented in [4].

Figure 5.12 displays the time-evolution of turbulent kinetic energy during the second injection event for the DFI cases, referring to the conditions outlined in the dwell time sweep presented in table 5.1. The primary observation from this analysis is a small alteration of turbulent conditions near the chamber bottom at SOI, which becomes more pronounced as the dwell time is reduced. However, in all tested conditions, this does not appear to intensify turbulence in the duct outlet region when the spray exits the duct at 200 µs after SOI as the residual turbulence from the previous injection rapidly dissipates and returns to a quiescent state during this time period. Consistent with previous findings, the peak turbulent kinetic energy is located in the duct exit region, affirming the advantage with DFI in terms of enhancing mixing in this area.

In fig. 5.13 the mass share sweep is observed for what the turbulent kinetic energy distribution concerns. In this case, there are not apparent modifications in the TKE evolution based on the varying amount of mass injected during the second injection event. Furthermore, the peak TKE is still situated in the duct exit region, in line with the typical behavior observed when DFI is employed. Consequently, this analysis does not reveal any significant concerns, suggesting the feasibility of a second injection event. However, as previously mentioned in the context of air entrainment analysis, the enhanced mixing facilitated by the peak turbulence in that region is advantageous when it results in better fuel-air mixing. On the contrary, this effect could be counterproductive if the surrounding gases in that region are composed of hot combustion products.

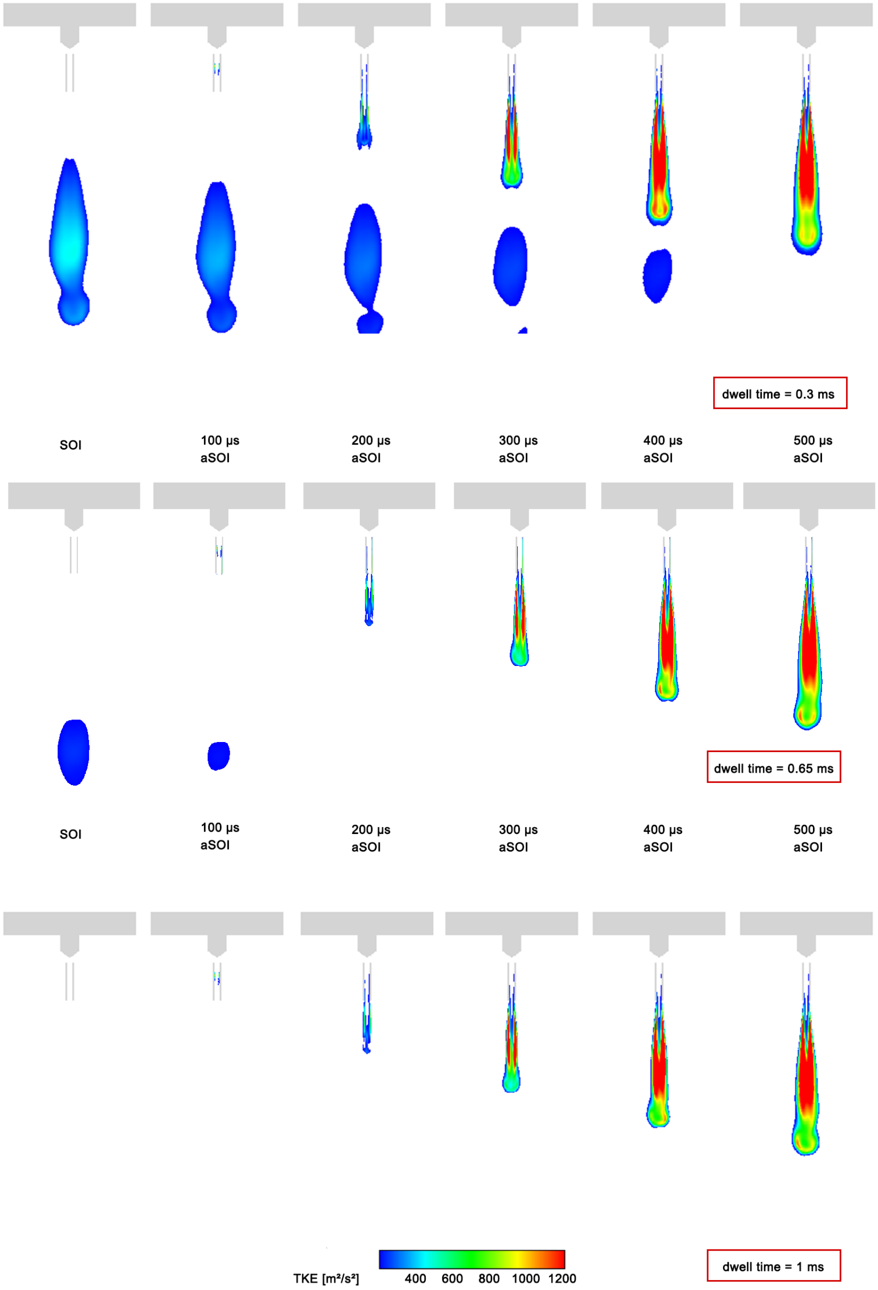

Figure 5.12: Dwell time sweep: Turbulent Kinetic Energy distribution during second injection event.

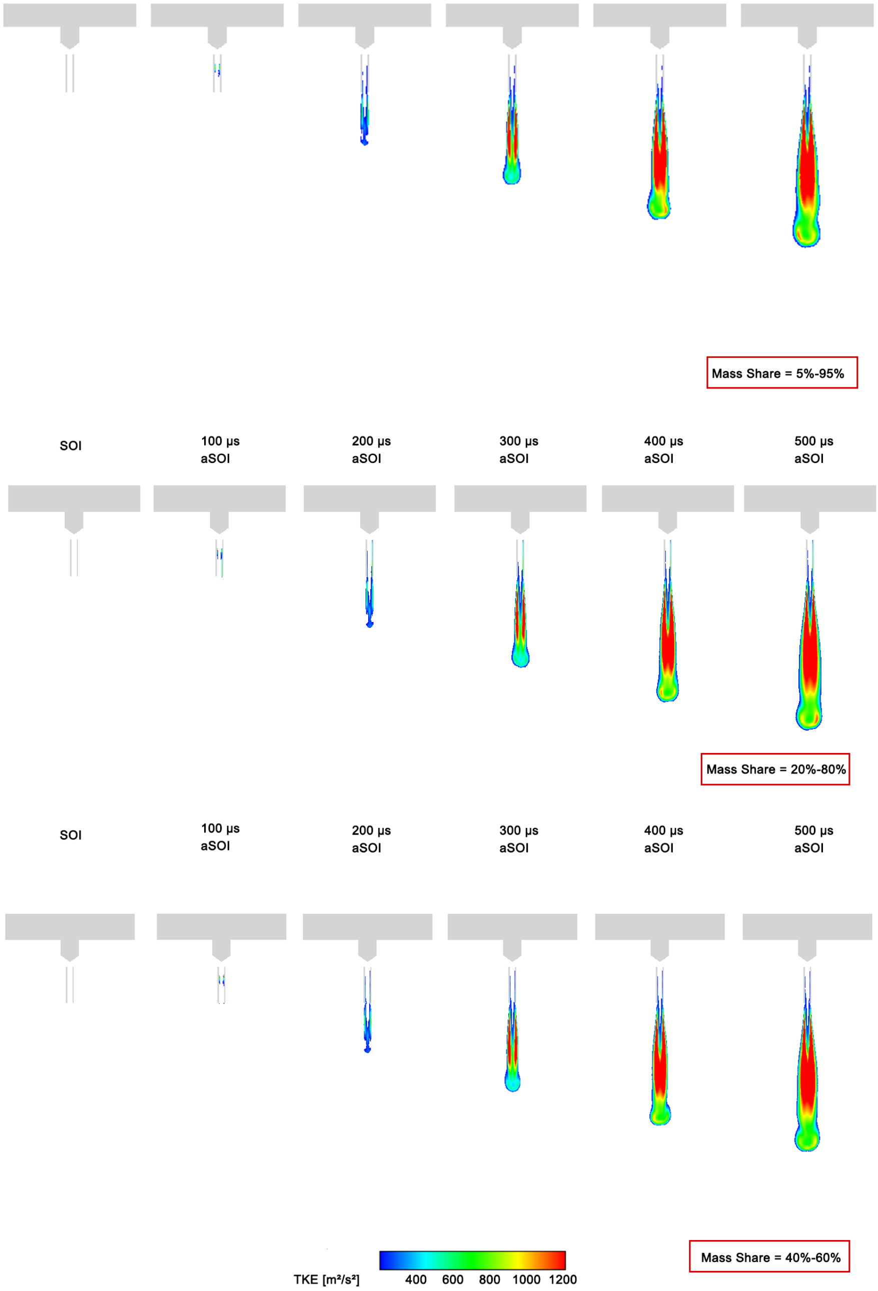

Figure 5.13: Mass Share sweep: Turbulent Kinetic Energy distribution during second injection event.

5.1.3 Equivalence Ratio

DFI adoption has been shown to mitigate the equivalence ratio value. This is of paramount importance in order to promote the sustainability of alternative combustion strategy such as the LLFC [3]. Therefore, in this section it is wanted to investigate how the first injection interact with the second one thus modifying the equivalence ratio distribution.

As previously done for turbulent kinetic energy, also in this case the focus was on the second injection. However, the comparison is also made with the correspondent free-spray cases to better understand whether DFI outperforms the free-spray scenario in terms of maximum equivalence ratio obtained, and consequently, to investigate the presence of rich core which could lead to more soot production in the correspondent reactive condition.

Figure 5.14 presents the results of the dwell time sweep. In all three tested dwell times, a rich core is observed at both 100 µs and 200 µs aSOI in the DFI cases. In contrast, no distinct rich zones are noted for the free-spray case. However, as the injection proceeds, DFI appears to perform better, resulting in a mean equivalence ratio at 500 µs aSOI that is slightly lower compared to the free-spray case. This behavior can be explained by considering the trend of air entrainment. For the free-spray case, steady-state air entrainment is reached immediately. In contrast, DFI exhibits a delay, resulting in a smaller amount of air in the initial injection phase but compensating with a higher amount of air for mixing once steady-state conditions are achieved. This leads to DFI outperforming the free-spray scenario in terms of equivalence ratio after the initial injection phase. The presence of that rich cores, however, must be properly considered in reactive conditions; indeed, if ignition were to occur at 100 µs or 200 µs, the advantages gained at 500 µs could be nullified, potentially leading to increased soot production.

Regarding the interaction of this injection with the previous one, there are no significant issues to report. The spray is injected into a zone with low equivalence ratio values, although different from the rest condition due to the previous injection. This interaction is not problematic, as the equivalence ratio is much lower than 2. However, in the case with the shortest dwell time, i.e. 0.3 ms, higher equivalence ratios are observed in this zone in free-spray conditions. This is closely related to the higher mixing associated with DFI, as well as the reduced time between the two injections compared to the other two tested conditions, i.e dwell time equal to 0.65 ms and 1 ms respectively.

The mass share sweep for the equivalence ratio is depicted in fig. 5.15. In general, the same findings obtained in the dwell time sweep are recapitulated here. Once more, the second injection occurs in a region with a non-negligible equivalence ratio. However, a clear dependence on the size of this region is observed, with a smaller region when less mass has been injected in the first injection event. Indeed, while it may not be appropriate to speak of ”interaction” between the two injections given the low value of the equivalence ratio in this zone, it can be seen that this interaction is practically nonexistent in the case of a mass share of 5%-95%, while it is maximized in the case of 40%-60%. Injecting less mass in the first injection results in less fuel being mixed with air; therefore, even though low values of entrainment are reached during the first injection, this does not lead to a high equivalence ratio at the start of injection (SOI) of the second injection. Moreover, also in this case a rich pocket at 200 µs and 300 µis present, with the mixing increasing later in the injection.

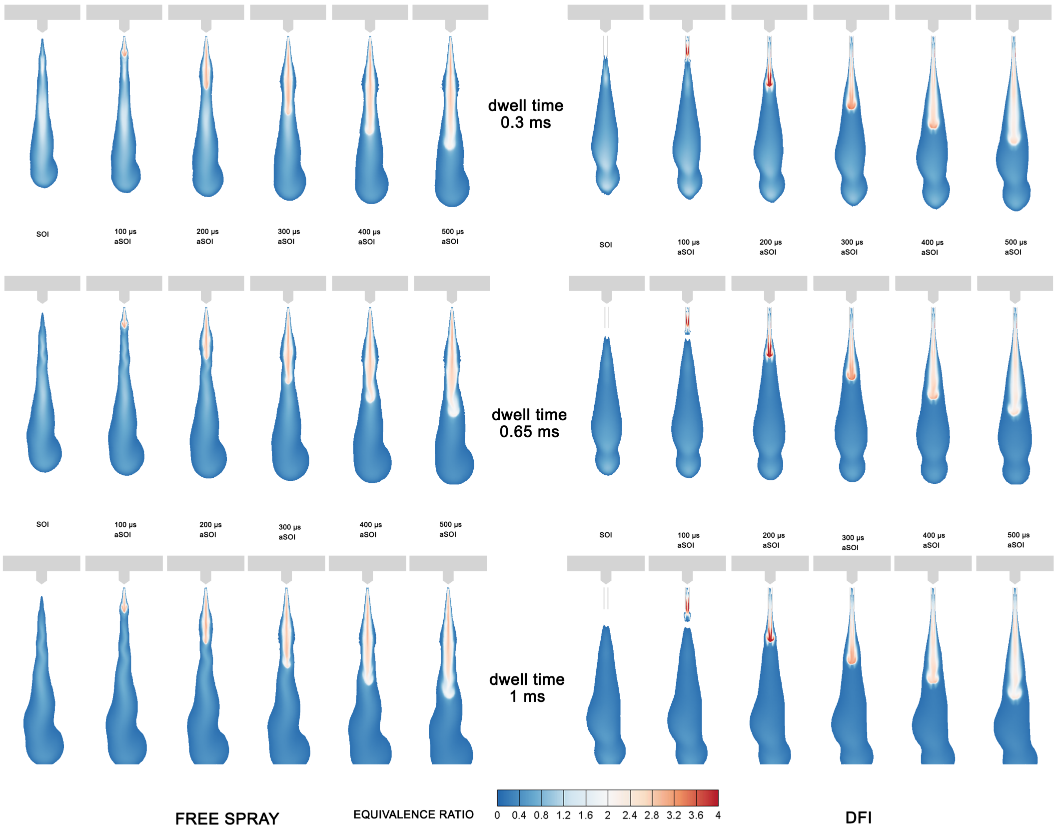

Figure 5.14: Dwell Time sweep: Equivalence Ratio distribution during second injection event.

5.2 ECN Spray D: non-reacting analysis

In this section, a portion of the non-reacting analysis conducted for the PoliTO-UniPG spray model has been replicated using the ECN Spray D model developed as described in sec. 4.2. As mentioned in section 4.2.7, this model is fully-predictive, necessitating further validation activities to ensure its reliability. In this sense, the goal here is to explore the potential of this model for analyzing the coupling interaction between DFI and multi-injection profiles. At this purpose, only a test has been performed with split-injection employment with this model. In this case the total injected mass is 16.78 µg, the mass share is 5% at the first injection and 95% to the second one; the dwell time adopted is 0.9 ms. In fig. 5.16, the rate shape associated to this simulation is depicted.

Figure 5.17 displays the air flow rate in the region upstream of the duct inlet. The same procedure described in section 5.1.1 was used. The air flow rate is higher for DFI, even with split-injection. However, when comparing the total amount of air entering the spray under these conditions with that in the case of a single injection, no significant difference is observed. In this case, the effect of the tail is less pronounced compared to the previous analysis performed on the PoliTO-UniPG spray model. Furthermore, the tested case is the one in which the pressure does not reach the minimum steady-state value, as depicted in fig. 5.18, thus preventing the benefits of DFI in terms of air flow rate during the first injection. However, the amount of air associated with this loss is very small, and therefore, the mixing

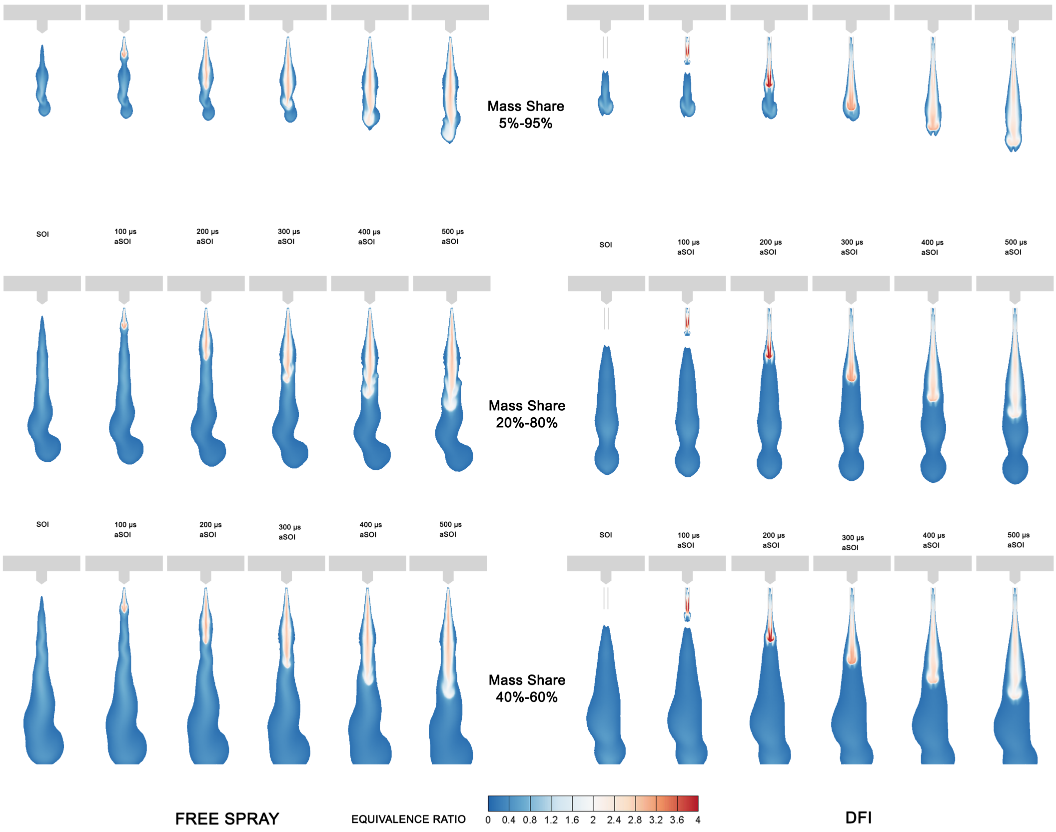

Figure 5.15: Mass Share sweep: Equivalence Ratio distribution during second injection event.

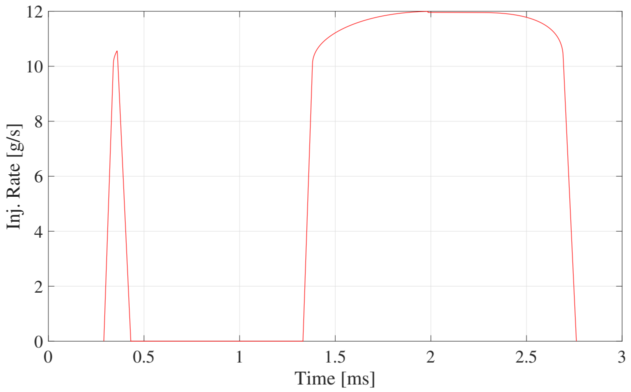

Figure 5.16: Rate shape with split injection profile in ECN Spray D condition. Mass Share: 5%-95%. Dwell time = 0.95 ms.

is not practically affected by this limitation.

Figure 5.19 displays the time-evolution of the equivalence ratio. The fully-predictive results still show the presence of rich pockets for both DFI and free-spray cases, characterized by equivalence ratio values exceeding 4. However, in line with the results obtained with the PoliTO-UniPG model, there is no deterioration when transitioning from a single-injection profile to a split-injection one. Consequently, even though the results for DFI under these thermodynamic conditions are not promising, as they were not for the PoliTO-UniPG test conditions, no criticisms can be attributed to the use of DFI with such a multi-injection strategy. Moreover, it is important to stress that no conclusions can be drawn in non-reactive conditions regarding the lift-off length and the equivalence ratio observed at that position; hence, the high equivalence ratio values obtained under these thermodynamic conditions do not allow to assert whether DFI is ineffective in reducing soot production, as it was not feasible to make the opposite claim for the PoliTO-UniPG case.

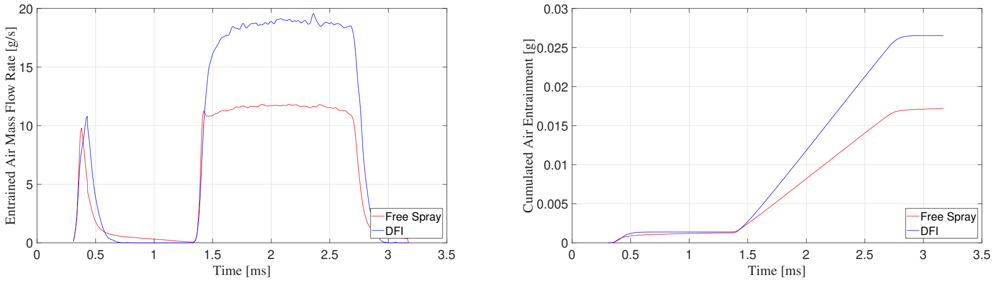

Figure 5.17: *Left*: Air entrainment for both Free Spray and DFI configurations with split-injection profile. *Right*: Correspondent total entrained air for both Free Spray and DFI configurations. Mass share = 5%-95%. Dwell Time = 0.9 ms.

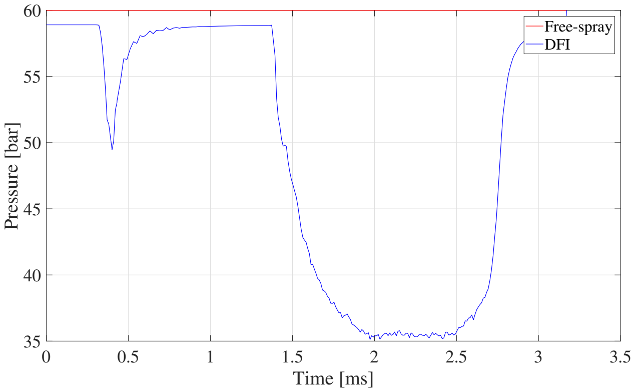

Figure 5.18: ECN Spray D: Pressure time evolution in the in-duct region. Mass share = 5%-95%. Dwell Time = 0.9 ms.

In summary, the conditions experienced in the ECN Spray D model seem to result in a worsening of the equivalence ratio, even when only one injection event is employed. However, no worsening is observed when transitioning from one injection to two injection events compared to the results obtained with only one injection. Moreover, the air flow rate into the spray is still enhanced by the adoption of the duct, even when two injections are employed.

In this context, further analyses are required for this model to gain a better understanding of the phenomena related to the lower air-fuel mixing observed. Furthermore, as previously mentioned, additional analyses are needed to provide better validation of the model, thereby

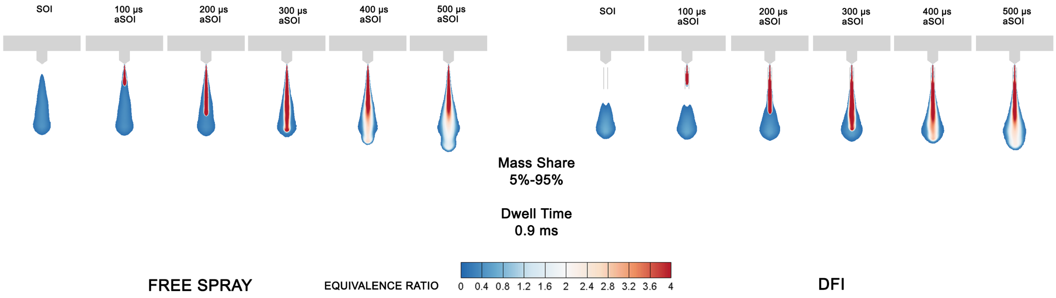

Figure 5.19: ECN Spray D: Equivalence Ratio distribution during second injection event.

ruling out model-related issues as the cause of the reduced mixing.

Chapter 6

Conclusions

In conclusion of this work, a step forward has been made in understanding the potential coupling between Ducted Fuel injection (DFI) technology and multi-injection (MI) profiles. This represents a crucial aspect for the practical implementation of DFI in current Diesel engine series production.

To summarize the activities conducted in this thesis, first a tool for creating multi-injection profiles was developed. Indeed, it was essential to rely on injection profiles that closely matched the characteristics of the injectors used for calibrating the models employed in the analysis. Following this, a virtual test-rig was calibrated and validated within a 3D Computational Fluid Dynamics (CFD) environment for free-spray conditions. Experimental data from the Engine Combustion Network (ECN) Spray D setup were used for this purpose. Particular emphasis was placed on the sub-models utilized, and efforts were dedicated to calibrating their key parameters to achieve alignment with the experimental data. Subsequently, a validation based on prior knowledge was conducted for the DFI case. The developed virtual test-rig, in this context, demonstrated a high level of consistency with previous findings, particularly regarding the distribution of turbulent kinetic energy and air flow rate in the spray at the duct inlet region. Nevertheless, the analysis of the equivalence ratio distribution revealed the presence of rich cores. Finally, both the previously developed and validated PoliTO-UniPG spray model and the new ECN Spray D model were employed to conduct non-reacting simulations. These simulations aimed to investigate the mixing potential and flow field characteristics associated with the coupling of DFI and split-injection profiles. The results were generally encouraging,

Despite the encouraging outcomes, there are still several phenomena that remain not fully understood. In this regard, future work should be directed towards a more extensive validation of the developed test-rig, for both free-spray and DFI conditions, to ensure the reliability of the results, especially for DFI conditions. It is important to better investigate the phenomena related to the transient phase of liquid penetration and how they are related to the turbulent initial conditions. Furthermore, in the context of turbulence investigations into the reliability of the results can be performed by adopting more complex and precise turbulence models such as Large Eddy Simulation (LES).

The non-reacting analysis conducted on the coupling possibilities between DFI and MI profiles has highlighted the strong potential of the numerical tools developed. However, this analysis cannot be considered complete. It is essential to investigate flow field variables under different test conditions to gain a better understanding of how the flow field is modified.

Furthermore, non-reacting analysis alone does not provide sufficient information regarding the actual soot mitigation properties. Therefore, it will be of paramount importance to invest efforts in implementing appropriate combustion models in the virtual test rig developed, enabling combustion simulations. This will allow for the analysis of actual lift-off length and the consequent sustainability of alternative combustion strategies.

Bibliography

[1] Dec. J. “A Conceptual Model of DI Diesel Combustion Based on Laser-Sheet Imaging”. In: *SAE Technical Paper* (1997). DOI: `10.4271/970873`.

[2] N. Ladommatos, S. Abdelhalim, and H. Zhao. “The effects of exhaust gas recirculation on diesel combustion and emissions”. In: *International Journal of Engine Research* 1.1 (2000), pp. 107–126. DOI: `10.1243/1468087001545290`.

[3] Christopher J. Polonowski et al. “An Experimental Investigation of Low-Soot and Soot-Free Combustion Strategies in a Heavy-Duty, Single-Cylinder, Direct-Injection, Optical Diesel Engine,” in: *SAE Int. J. Fuels Lubr.* (2012). ISSN: 1946-3952. DOI: `10.4271/2011-01-1812`.

[4] Charles J. Mueller et al. “Ducted fuel injection: A new approach for lowering soot emissions from direct-injection engines”. In: *Applied Energy* 204 (2017), pp. 206–220. ISSN: 0306-2619. DOI: `10.1016/j.apenergy.2017.07.001`.

[5] F. Millo et al. “Ducted Fuel Injection: Experimental and numerical investigation on fuel spray characteristics, air/fuel mixing and soot mitigation potential”. In: *Fuel* 289 (2021), p. 119835. ISSN: 0016-2361. DOI: `10.1016/j.fuel.2020.119835`.

[6] R.K. Gehmlich et al. “Using ducted fuel injection to attenuate or prevent soot formation in mixing-controlled combustion strategies for engine applications”. In: *Applied Energy* 226 (2018), pp. 1169–1186. DOI: `10.1016/j.apenergy.2018.05.078`.

[7] K. Svensson and G. Martin. “Ducted Fuel Injection: Effects of Stand-Off Distance and Duct Length on Soot Reduction”. In: *SAE Int. J. Adv. & Curr. Prac. in Mobility* (2019). DOI: `10.4271/2019-01-0545`.

[8] Christopher W. Nilsen, Drummond E. Biles, and Charles J. Mueller. “Using Ducted Fuel Injection to Attenuate Soot Formation in a Mixing-Controlled Compression Ignition Engine”. In: *SAE International Journal of Engines* 12.3 (2019), pp. 309–322. ISSN: 19463936, 19463944.

[9] Christopher Nilsen et al. “Ducted Fuel Injection vs. Conventional Diesel Combustion: Extending the Load Range in an Optical Engine with a Four-Orifice Fuel Injector”. In: *SAE International Journal of Engines* 14 (Oct. 2020). DOI: `10.4271/03-14-01-0004`.

[10] Kenth Svensson et al. “Performance and Emission Results from a Heavy-Duty Diesel Engine with Ducted Fuel Injection”. In: *SAE Technical Paper* 14 (2021), p. 14. DOI: `10.4271/2021-01-0503`.

[11] Andrea Piano et al. “Investigation of Ducted Fuel Injection Implementation in a Retrofitted Light-Duty Diesel Engine through Numerical Simulation”. In: *SAE Int. J. Engines* (Nov. 2022). DOI: `10.4271/03-16-05-0038`.

[12] Gustav Nyrenstedt et al. “Ducted fuel injection with Low-Net-Carbon fuels as a solution for meeting future emissions regulations”. In: *Fuel* 338 (2023), p. 127167. DOI: `10.1016/j.fuel.2022.127167`.

[13] Andrea Piano et al. “Numerical and Experimental Assessment of a Solenoid Common-Rail Injector Operation with Advanced Injection Strategies”. In: *SAE International Journal of Engines* 9.1 (2016), pp. 565–575. ISSN: 19463936, 19463944.

[14] Lucio Postrioti et al. “Zeuch method-based injection rate analysis of a common-rail system operated with advanced injection strategies”. In: *Fuel* 128 (2014), pp. 188–198. ISSN: 0016-2361. DOI: `10.1016/j.fuel.2014.03.006`.

[15] Engine Combustion Network, ECN. `https://ecn.sandia.gov/`. 2023.

[16] R. Payri et al. “Hydraulic characterization of diesel engine single-hole injectors”. In: *Fuel* 180 (2016), pp. 357–366. ISSN: 0016-2361. DOI: `10.1016/j.fuel.2016.03.083`.

[17] Raul Payri et al. “A study of the relation between nozzle geometry, internal flow and sprays characteristics in Diesel fuel injection systems”. In: *KSME International Journal* 18 (July 2004), pp. 1222–1235. DOI: `10.1007/BF02983297`.

[18] Jeffrey D. Naber and Dennis L. Siebers. “Effects of Gas Density and Vaporization on Penetration and Dispersion of Diesel Sprays”. In: *SAE Technical Paper* (1996).

[19] R.D. Reitz and C.J. Rutland. “Development and testing of diesel engine CFD models”. In: *Progress in Energy and Combustion Science* 21.2 (1995), pp. 173–196. ISSN: 0360-1285. DOI: `10.1016/0360-1285(95)00003-Z`.

[20] Z. Han and R. D. Reitz. “Turbulence Modeling of Internal Combustion Engines Using RNG k-ε Models”. In: *Combustion Science and Technology* (2007). DOI: `10.1080/00102209508907782`.

[21] Peter J O’Rourke. “Statistical properties and numerical implementation of a model for droplet dispersion in a turbulent gas”. In: *Journal of Computational Physics* 83.2 (1989), pp. 345–360. ISSN: 0021-9991. DOI: `10.1016/0021-9991(89)90123-X`.

[22] J.D. Naber and Rolf D. Reitz. “Modeling Engine Spray/Wall Impingement”. In: *SAE Technical Paper* (1998). DOI: `10.4271/880107`.

[23] D. Gonzalez et al. “A Study of Diesel Cold Starting using both Cycle Analysis and Multidimensional Calculations”. In: *SAE Technical Paper* (). DOI: `10.4271/910180`.

[24] L. H. J. Wachters and N. A. J. Westerling. “The heat transfer from a hot wall to impinging water drops in the spheroidal state”. In: *Chemical Engineering Science* 21.11 (Jan. 1966), pp. 1047–1056. DOI: `10.1016/0009-2509(66)85100-X`.

[25] K.J. Richards, P.K. Senecal, and E. Pomraning. *CONVERGE 3.0*. 2023.

[26] A. A. Amsden, P. J. O’Rourke, and T. D. Butler. “KIVA-II: A computer program for chemically reactive flows with sprays”. In: *[]* (May 1989). DOI: `10.2172/6228444`.

[27] Rolfd Reitz et al. “Modeling atomization processes in high-pressure vaporizing sprays”. In: *Atomisation and Spray technology* 3.4 (1987), pp. 309–337.

[28] P. K. Senecal et al. “Grid-Convergent Spray Models for Internal Combustion Engine Computational Fluid Dynamics Simulations”. In: *Journal of Energy Resources Technology* 136.1 (Sept. 2013), p. 012204. ISSN: 0195-0738. DOI: `10.1115/1.4024861`.

[29] P. O’Rourke and A. Amsden. “Statistical properties and numerical implementation of a model for droplet dispersion in a turbulent gas”. In: *SAE Technical Paper* (1987). DOI: `10.4271/872089`.

[30] A. Liu, D. Mather, and R. Reitz. “Modeling the Effects of Drop Drag and Breakup on Fuel Sprays”. In: *SAE Technical Paper* (1993). DOI: `10.4271/930072`.

[31] Rolf Reitz and F. Bracco. “Mechanisms of breakup of round liquid jets”. In: *Encyclopedia of Fluid Mechanics* 3 (Jan. 1986).

[32] John B. Heywood. *Internal Combustion Engine Fundamentals*. McGraw-Hill Education, 1998.

[33] Cristiano Segatori. "Ducted Fuel Injection: a Computational Fluid Dynamics analysis of soot formation mitigation mechanisms." Master Thesis. Politecnico di Torino, 2020.

[34] Wai Tong Chung, Peter C Ma, and Matthias Ihme. "Examination of diesel spray combustion in supercritical ambient fluid using large-eddy simulations". In: *International Journal of Engine Research* 21.1 (2020), pp. 122–133. DOI: `10.1177/1468087419868388`.

Acknowledgements

My first thanks go to my advisor, *Prof. Federico Millo*, for giving me the opportunity to undertake this work, for the support, guidance, and kindness shown to me. Thank you for believing in me throughout these months.

My thanks also go to the thesis co-advisors *Dr. Andrea Piano* and *Cristiano Segatori* for the availability, kindness, and passion you have shown me throughout this journey. Your experience and expertise have undoubtedly played a foundational role in this work.

Additionally, I would like to thank the entire e3 - *Energy Environment Research Group* for how you welcomed me during these months spent together.

Finally, I would like to express my gratitude to *Politecnico di Torino* for the university education as well as all the opportunities that has been afforded to me during these two years.